FIRST-PRINCIPLES INVESTIGATION OF GRAPHITIC NANOSTRUCTURES

A DISSERTATION SUBMITTED TO
THE DEPARTMENT OF PHYSICS
AND THE GRADUATE SCHOOL OF ENGINEERING AND SCIENCE
OF BILKENT UNIVERSITY
IN PARTIAL FULFILLMENT OF THE REQUIREMENTS
FOR THE DEGREE OF
DOCTOR OF PHILOSOPHY

By
Hüseyin Şener Şen
August, 2013

I certify that I have read this thesis and that in my opinion it is fully adequate, in scope and in quality, as a dissertation for the degree of Doctor of Philosophy.

Prof. Dr. Oğuz Gülseren (Advisor)

I certify that I have read this thesis and that in my opinion it is fully adequate, in scope and in quality, as a dissertation for the degree of Doctor of Philosophy.

Assoc. Prof. Dr. M. Özgür Oktel

I certify that I have read this thesis and that in my opinion it is fully adequate, in scope and in quality, as a dissertation for the degree of Doctor of Philosophy.

Assist. Prof. Dr. Emrah Özensoy

I certify that I have read this thesis and that in my opinion it is fully adequate, in scope and in quality, as a dissertation for the degree of Doctor of Philosophy.

Assist. Prof. Dr. Coşkun Kocabaş

I certify that I have read this thesis and that in my opinion it is fully adequate, in scope and in quality, as a dissertation for the degree of Doctor of Philosophy.

Assoc. Prof. Dr. Hande Toffoli

Approved for the Graduate School of Engineering and Science:

Prof. Dr. Levent Onural
Director of the Graduate School

ABSTRACT

FIRST-PRINCIPLES INVESTIGATION OF GRAPHITIC NANOSTRUCTURES

Hüseyin Şener Şen
Ph.D. in Physics
Supervisor: Prof. Dr. Oğuz Gülseren
August, 2013

In this thesis, first-principles investigations of several graphene related nano-systems based on density functional theory are presented. First, the electronic structure of several graphene nano-ribbons both in 1D and 0D (up to systems with more than 1000 atoms) including all types (armchair, zigzag and chiral) are discussed using tight binding calculations. We observed that the band gap of the ribbons depend both on the length of the ribbon and the angle of chirality. Second, the effect of phosphorus and sulfur during the growth of carbon nanotubes is investigated from *ab-initio* density functional theory based calculations. To this end, we present the binding chemistry of phosphorus and sulfur atoms on graphene with and without vacancies and kink like defect structures. Consequently, the difference between the bindings of these two atoms is discussed in order to understand the reason behind their effects on the growth mechanism. The details of the phosphorus or sulfur binding are important in order to understand the occurrence of Y-junctions and kinks in carbon nanotubes as well. Third, we focus on the interaction of bilayer graphite and multi-walled carbon nanotubes with the Li atom since these materials are prime candidates for the electrodes for battery applications. The need for rechargeable batteries with high capacity increased enormously by the invention of electronic devices like cell phones or MP3 players. Hence, there is a huge effort to develop and improve Li-ion batteries. Therefore, we have investigated interaction of Li with graphene and Li intercalation to bilayer graphene and multi-walled carbon nanotubes from planewave pseudo potential calculations. Finally, super-periodic graphitic structures observed through scanning tunnelling microscope are described and investigated from density functional calculations. The difference between the observed and actual periodicity and the occurrence of the so-called Moire patterns are explained in terms of geometrical calculations and the charge density of these systems.

Keywords: Graphene, nano-ribbon, tight binding, electronic structure, band gap, AGNR, ZGNR, CGNR, quantum confinement, phosphorus and sulfur chemistry, Density Functional Theory, VASP, lithium intercalation, battery, Moire pattern, actual periodicity, charge density, density of states.

ÖZET

GRAFEN TABANLI NANOYAPILARIN İLK-PRENSİP HESAPLAR İLE İNCELENMESİ

Hüseyin Şener Şen
Fizik, Doktora
Tez Yöneticisi: Prof. Dr. Oğuz Gülseren
Ağustos, 2013

Bu tez çalışmasında çeşitli grafen tabanlı nanoyapıların özellikleri yoğunluk fonksiyoneli teorisine dayanan ilk-prensip hesaplar ile incelendi. İlk olarak, birçok grafen nano-şeridin (bin ve üzeri atom sayılarına ulaşan), elektronik yapısı sıkı bağlanma yöntemi ile hesaplanarak sunulmuştur. Bu grafen nano-şeritler hem sıfır hem de bir boyutlu yapılar olmak üzere koltuk, zigzag ve kiral göz önüne alınarak olası tüm çeşitleri içermektedir. Bu hesaplara göre şeritlerin bant aralığının hem şeritlerin uzunluğuna hem de kiral açıya bağlı olduğu gözlemlenmiştir. İkinci olarak, fosfor ve sülfür atomlarının karbon nanotüpün büyümesi sırasındaki etkilerini anlamak üzere yoğunluk fonksiyoneli teorisine dayalı hesaplar yapılmıştır. Bu amaçla fosfor ve sülfür atomlarının hem boşluk içeren ve içermeyen grafene hem de kıvrım oluşturan kusurlu bölgelere bağlanma kimyası incelenmiştir. Sonuçta büyümeye olan etkilerinin arkasındaki sebebi anlamak için bu iki atomun bağlanmaları arasındaki fark irdelenmiştir. Bunun ötesinde bu bağlanma kimyalarının incelenmesi karbon nanotüplerde oluşan Y-eklentilerini ve kıvrım bölgelerini anlamak açısından da oldukça önemlidir. Üçüncü olarak, çift katmanlı grafen ve çok duvarlı karbon nanotüplerin Li atomu ile nasıl etkileşime girdikleri araştırılmıştır. Son yıllarda cep telefonu, mp3 çalar vb. elektronik aletlerin keşfi ile yüksek kapasiteye sahip tekrar doldurulabilen pil ihtiyacı müthiş oranda arttı. Böylece Li-iyon pillerinin üretimi ve geliştirilmesi için büyük çaba gösterilmeye başlandı. Bu yüzden pillerde elektrot olmak için ciddi aday olarak kabul edilen çift katmanlı grafen ve çok duvarlı karbon nanotüplerle lityumun etkileşimi ve interkalasyonu düzlemsel dalga sahte potansiyel hesaplarıyla araştırılmıştır. Son olarak, yoğunluk fonksiyoneli teorisi kullanarak taramalı tünelleme mikroskobu altında gözlemlenebilen süper peryodik grafen tabanlı yapılar incelenmiştir. Gözlemlenen ve gerçek peryodun farkı ve Moire şekillerinin oluşumu, geometrik hesaplar ve yük yoğunluğu cinsinden açıklanmıştır.

Anahtar sözcükler: Grafen, nano-şerit, sıkı baglanma, elektronik yapı, bant aralığı, KGNŞ, ZGNŞ, CGNŞ, kuvantum hapsolması, fosfor ve sülfür kimyası, yoğunluk fonksiyoneli teoremi, lityum interkalasyon, pil, Moire şekli, yük yoğunluğu, durum yük yoğunluğu.

Acknowledgement

I would like to thank to Prof. Dr. Oğuz Gülseren with all my heart, for his ultra-supervision and kindness.

I would like to express my deepest gratitude to Assoc. Prof. Dr. M. Özgür Oktel and Assist. Prof. Erman Bengü for their guidance throughout my PhD. studies.

I am indebted to Assist. Prof. Dr. Emrah Özensoy, Assist. Prof. Dr. Coşkun Kocabaş and Assoc. Prof. Dr. Hande Toffoli for accepting to read, criticize and improve my thesis.

I would like to thank to Assist. Prof. Dr. Rasim Volga Ovalı, Assoc. Prof. Dr. Oğuzhan Gürlü, Dr. Gökçe Küçükayan Doğu and Dilek Yıldız for their contribution in my studies.

I would like to thank my parents Ahmet-Necla Şen, brothers Şenol-İbrahim Şen, mother and sister-in-law Hüsne and Derya Soyer for their never ending support.

I am also grateful to my friends İsmail Can Oğuz, Mustafa Erol, Emine Selamoğlu, Ali Menteşoğlu and the AgA's Marabas group for their kind friendship and supports.

I would like to express my gratitude to TUBITAK for the financial support supplied during my PhD. studies.

Most importantly, I would like to thank my beloved wife Hicran Şen. I will always be indebted to her for everything she has done for me.

Contents

List of Figures

List of Tables

Chapter 1

Introduction

All living organisms depend on carbon. This element is so important that there is a branch of chemistry, organic chemistry, which deals with hydrocarbon (CH) containing compounds. Even just the role of organic chemistry in science is enough to consider this element as the most important one. The nature of interaction of the carbon atom with other atoms can vary a lot. This is because of the capability of carbon atoms to hybridize in various combinations, sp, sp^2 or sp^3. Carbon atoms can make stable C-C single bonds among themselves with sp^3 hybridization, C=C double bonds with sp^2 hybridization, C≡C triple bonds with sp hybridization in an organic compound. Therefore, the compounds can occur in different forms like chain, branched or ring form. The structures containing only carbon atoms are also very important. Bucky ball (figure 1.1a) is zero dimensional (0D), carbon nanotubes (CNTs) (figure 1.1b) are one dimensional (1D) [1], graphene (figure 1.1c) is two dimensional (2D) [2, 3], diamond and graphite (figure 1.1d) are three dimensional (3D) structures. For a physicist dealing with nano-sized structures, geometry of the structure is very important, since it determines the dimensionality. In CNTs and graphene, carbon atoms make sp^2 bonding leaving one of their electrons, namely p_z electron unbounded. In graphene, carbons create a honeycomb structure with hexagons on a plane. In this structure, every carbon atom has three nearest neighbours. Therefore, single sp^2 bonds are created with each of them, three bonds in total. Carbon

atom has four valance electrons. Three of them are paired with the electrons of the neighbouring atom leaving one of them, the electron in p_z orbital, unpaired. This unpaired electron is responsible for the electronic properties of graphene as will be discussed later. In carbon nanotubes, these hexagons are not planar but they are rolled to create a cylinder. The C_{60} structure is just a sphere, which makes them zero dimensional molecules with discrete energy states. Graphite, a three dimensional allotrope of carbon, has been known for centuries. Graphene is a single layer of graphite. In graphite, the nearest carbon atoms in a layer have 1.42 Å of distance having strong interaction, whereas, graphene layers with a distance around 3.4 Å are weakly bounded by van der Waals forces. Therefore, graphite can be expected to have closer physical properties to graphene. Theoretical works enlighten these expectations, however, it was believed that graphene, since it is a two dimensional material, could not be stable and cannot exist until 2004. In 2004 Novoselov et. al made a breakthrough for graphene and managed to synthesize it [4]. Since then, experimental work has gained speed. Experiments were able to fulfill many theoretical expectations. For example, it is shown that graphene has a band structure where charge carriers are indeed massless Dirac fermions and go ballistic as was expected [5,6]. The ballistic transport property, as well as many other properties made graphene a popular material to work on. Researches on transport properties under the exposure of gaseous molecules [7,8] show that graphene can be used as a sensor with high sensitivity and response time [9]. Also, it is shown that electronic and magnetic properties can be modulated by doping with boron, nitrogen, phosphorus, sulfur etc [10–13]. Many researches were successful in opening a tunable band gap on graphene. Many different methods were used for this goal such as doping [9,14–17], chemical functionalization [18–20], and using electric fields [21]. A recent work showed that it is possible to open a band gap in the band structure of graphene by doping with sulfur atoms [14]. In the third chapter of this thesis, we investigate a different approach for the same purpose, i.e. graphene nano-ribbons.

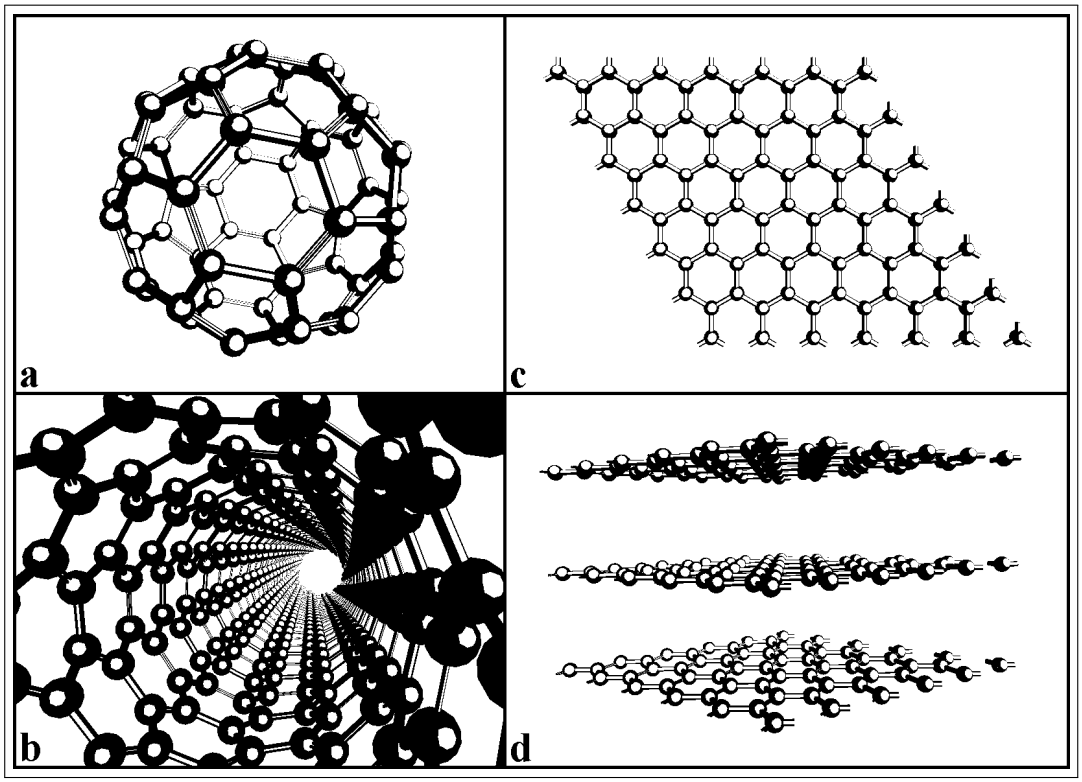

Figure 1.1: Structures of carbon with different dimensions; a) Bucky ball - C_{60} is a molecule consisting of wrapped graphene by introduction of pentagons on honeycomb lattice in 0D, b) Carbon nanotubes are rolled-up cylinders of graphene in 1D, c) Graphene consists of honeycomb lattice of carbon atoms in 2D and d) Graphite is a stack of graphene layers creating a 3D structure.

1.1 General Properties of Graphene

Graphite is composed of graphene layers with 3.35 Å of distance in between them. These layers are held together by Van der Waals forces. Although, graphite is known by human kind for centuries, graphene could only be isolated in 2004 by Novoselov et al. [4]. Therefore, the theoretical expectations on graphene was realized experimentally only recently. Carbon atoms of graphene creates a hexagonal lattice. This kind of lattice occurs due to sp^2 hybridization of the atoms. Every C atom creates σ bonds with three other C atoms as shown in figure 1.2a. C-C distance for these neighbouring atoms is $a = 1.42$ Å. sp^2 hybridization is created by one 2s and two 2p electrons of the carbon. However, carbon has four valance electrons and the last 2p electron remains unpaired. The electronic properties of graphene is due to this unpaired electron. Graphene has zero band gap as the valance and conduction bands coincide at point K of the Brillouin zone. K point in reciprocal space of graphene is called Dirac point and the band structure has a conical shape around this point. If a few graphene layers are put together to construct graphite, valance and conduction bands start to overlap notably creating a metallic film.

Tight binding approach is a simple but very accurate method to describe the electronic structure of periodic systems. With the tight binding approach, electronic structure of graphene can be described very easily. We first examine the geometrical structure. In figure 1.2a, carbon atoms of graphene are shown. The region between $\vec{a}_1$, $\vec{a}_2$ and gray lines is the unit cell. The length of these unit vectors are 2.46 Å each. Then the lattice vectors can be defined in terms of the C-C bond distance a as;

$$\vec{a}_1 = \frac{a}{2}(3, \sqrt{3}) \tag{1.1}$$

$$\vec{a}_2 = \frac{a}{2}(3, -\sqrt{3}). \tag{1.2}$$

Two carbon atoms remain inside the unit cell. Although, in graphene there is no difference between these two atoms, in graphite there is. Therefore, we call the atoms A and B to make a distinction which will be useful in the proceeding

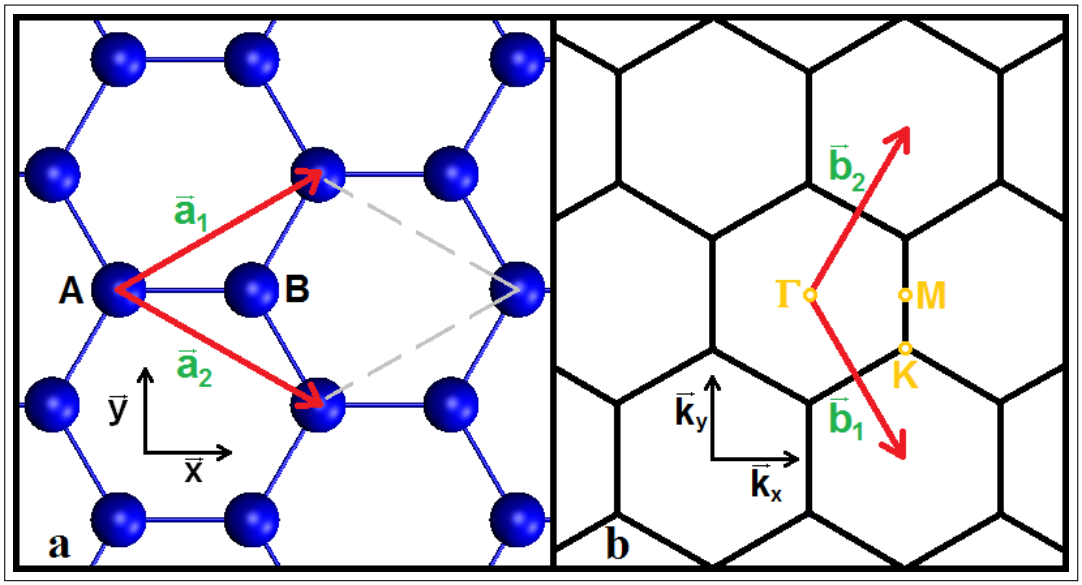

Figure 1.2: Lattice of graphene; a) in real space, b) in reciprocal space. $\vec{a}_1$, $\vec{a}_2$, $\vec{b}_1$, $\vec{b}_2$ are the lattice vectors, A and B are the carbon atom in the unit cell in real space, Γ, K and M are high symmetric points in recpirocal space.

chapters. The positions of these atoms are;

$$\vec{r}_A = (0,0) \tag{1.3}$$

$$\vec{r}_B = a(1,0). \tag{1.4}$$

In a similar way, we can define the vectors for the nearest neighbour list of atom A as follows;

$$\vec{\delta_1} = a(1,0) \tag{1.5}$$

$$\vec{\delta_2} = \frac{a}{2}(-1,\sqrt{3}) \tag{1.6}$$

$$\vec{\delta_3} = \frac{a}{2}(-1,-\sqrt{3}). \tag{1.7}$$

All these vectors define the positions of nearest neighbours of atom A which are all B type atoms. The second nearest neighbours of atom A, however, are A type

atoms and the position vectors for them can be defined as;

$$\vec{\delta_1'} = \frac{a}{2}(3, \sqrt{3}) \tag{1.8}$$
$$\vec{\delta_2'} = \frac{a}{2}(3, -\sqrt{3}) \tag{1.9}$$
$$\vec{\delta_3'} = a(0, -\sqrt{3}) \tag{1.10}$$
$$\vec{\delta_4'} = \frac{a}{2}(-3, -\sqrt{3}) \tag{1.11}$$
$$\vec{\delta_5'} = \frac{a}{2}(-3, \sqrt{3}) \tag{1.12}$$
$$\vec{\delta_6'} = a(0, \sqrt{3}). \tag{1.13}$$

In figure 1.2b, the Brillouin zone of graphene is shown. In the figure, $\vec{b}_1$ and $\vec{b}_2$ are the lattice vectors and Γ, K and M are high symmetric points of the lattice. The energy band diagrams drawn between these points reveal the electronic properties of graphene. The reciprocal lattice vectors are defined in terms of a as;

$$\vec{b}_1 = \frac{2\pi}{3a}(1, \sqrt{3}) \tag{1.14}$$
$$\vec{b}_2 = \frac{2\pi}{3a}(1, -\sqrt{3}). \tag{1.15}$$

With the given lattice vectors, positions of the high symmetry points Γ, K and M can be defined as;

$$\mathbf{\Gamma} = (0, 0) \tag{1.16}$$
$$\mathbf{K} = (\frac{2\pi}{3a}, \pm\frac{2\pi}{3\sqrt{3}a}) \tag{1.17}$$
$$\mathbf{M} = (\frac{2\pi}{3a}, 0). \tag{1.18}$$

We will use all the informative equations above while calculating the energy band diagram of graphene from tight binding approach. In order to calculate the energy band diagram, first we have to construct the Hamiltonian matrix H. The Hamiltonian matrix is composed of four main parts which can be shown as follows;

$$H = \begin{pmatrix} H_{AA} & H_{AB} \\ H_{BA} & H_{BB} \end{pmatrix}. \tag{1.19}$$

In equation 1.19, H_{AA} and H_{BB} represents the interaction of A type atoms, whereas, H_{AB} represents the interaction of A type and B type atoms. Since Hamiltonian matrix has to be Hermitian, H_{BA} is the just the complex conjugate of H_{AB}, i.e. ${H_{BA}}^* = H_{AB}$. The tight binding method, makes use of the linear combination of atomic orbitals located on various atoms weighted by a coefficient of plane waves $e^{i\vec{k}\vec{R}}$, where $\vec{R}$ denotes the atomic position. For simplicity, we can use first nearest neighbour approximation. According to this approximation, only the interaction of the nearest atoms contribute to the integral. Since, the nearest neighbours of A type atom are all B type, only self interaction term in H_{AA} survives and the rest becomes zero. The same situation is true for H_{BB} as well. Then, H_{AA} (or H_{BB}) can be written as;

$$H_{AA} = H_{BB} \begin{pmatrix} \epsilon_{2s} & 0 & 0 & 0 \\ 0 & \epsilon_{2p} & 0 & 0 \\ 0 & 0 & \epsilon_{2p} & 0 \\ 0 & 0 & 0 & \epsilon_{2p} \end{pmatrix}. \tag{1.20}$$

In equation 1.20, ϵ_{2s} is the self energy of the 2s orbital, ϵ_{2p} is the self energy of the 2p orbital. H_{AB} shows the interaction of A type and B type atoms, therefore, all elements have a contribution to Hamiltonian matrix. H_{AB} can be written as;

$$H_{AB} = \begin{pmatrix} \langle 2s_A|H_{15}|2s_B\rangle & \langle 2s_A|H_{16}|2p_{xB}\rangle & \langle 2s_A|H_{17}|2p_{yB}\rangle & \langle 2s_A|H_{18}|2p_{zB}\rangle \\ \langle 2p_{xA}|H_{25}|2s_B\rangle & \langle 2p_{xA}|H_{26}|2p_{xB}\rangle & \langle 2p_{xA}|H_{27}|2p_{yB}\rangle & \langle 2p_{xA}|H_{28}|2p_{zB}\rangle \\ \langle 2p_{yA}|H_{35}|2s_B\rangle & \langle 2p_{yA}|H_{36}|2p_{xB}\rangle & \langle 2p_{yA}|H_{37}|2p_{yB}\rangle & \langle 2p_{yA}|H_{38}|2p_{zB}\rangle \\ \langle 2p_{zA}|H_{45}|2s_B\rangle & \langle 2p_{zA}|H_{46}|2p_{xB}\rangle & \langle 2p_{zA}|H_{47}|2p_{yB}\rangle & \langle 2p_{zA}|H_{48}|2p_{zB}\rangle \end{pmatrix}. \tag{1.21}$$

In equation 1.21, $\langle 2s_A|$ defines the atomic 2s orbital of A atom, $\langle 2p_{xA}|$ defines the atomic $2p_x$ orbital of A atom and H_{nm} contains the plane wave and coupling contributions. $|2p_x\rangle$ can be decomposed into σ and π components. Considering the positions of B atoms $\vec{\delta_1}$, $\vec{\delta_2}$ and $\vec{\delta_3}$, we can say that atom A makes a bond with B atom at position $\vec{\delta_1}$ along x direction, but, A atom makes bond with B atoms at positions $\vec{\delta_2}$ and $\vec{\delta_3}$ with an angle of $\pi/3$ with respect to x axis. Therefore, we can decompose $|2p_{xB}\rangle$ as follows;

$$|2p_{xB}\rangle = |2p_\sigma\rangle + 2(\cos(\frac{\pi}{3})|2p_\sigma\rangle + \sin(\frac{\pi}{3})|2p_\pi\rangle). \tag{1.22}$$

In equation 1.22, the first term represents the contribution of the B atom at position $\vec{\delta_1}$ and the second term represents the contributions of other two B atoms. Here is an example of one of the elements of the matrix H_{AB};

$$\langle 2s_A|H_{16}|2p_{xB}\rangle = \langle 2s|\{H_{sp\sigma}(-e^{ik_x a} + e^{-ik_x a/2}e^{ik_y a\sqrt{3}/2}$$

$$\cos(\pi/3) + e^{-ik_x a/2}e^{-ik_y a\sqrt{3}/2}\cos(\pi/3))|2p_\sigma\rangle + H_{sp\pi}(-e^{ik_x a} + e^{-ik_x a/2}e^{ik_y a\sqrt{3}/2}$$

$$\sin(\pi/3) + e^{-ik_x a/2}e^{-ik_y a\sqrt{3}/2}\sin(\pi/3))|2p_\pi\rangle\}. \quad (1.23)$$

Here, $H_{sp\sigma}$ stands for the coupling between 2s and $2p_\sigma$ of atom A and B as a parameter. Similarly, $H_{sp\pi}$ represents the coupling parameter for the coupling between 2s and $2p_\pi$ which is equal to zero. Therefore, the last term in equation 1.23 drops and we are only left with $H_{sp\sigma}$ parameter which we call H_{sp} here after.

Table 1.1: Values of the coupling and overlap parameters in the Hamiltonian matrix for the carbon atom for nearest neighbour approximation. (Adapted from G. Dresselhaus, M.S. Dresselhaus and R. Saito,*Physical Properties of Carbon Nanotubes*, Imperial College Press, London, 1998.)

Coupling Parameter	Value(eV)	Overlap Parameter	Value(eV)
ϵ_{2s}	-8.868	-	-
ϵ_{2p}	0	-	-
H_{ss}	-6.769	S_{ss}	0.212
H_{sp}	-5.580	S_{sp}	0.102
H_σ	-5.037	S_σ	0.146
H_π	-3.033	S_π	0.129

Table 1.2: Another set of tight binding coupling parameters for carbonwith second nearest neighbour approximation. (Adapted from D. Tomanek, S. G. Louie, Phys. Rev B, 37, 8327, 1988)

First nearest neighbour parameter	Value(eV)	Second nearest neighbour parameter	Value(eV)
ϵ_s	-7.3	H_{ss2}	-0.18
ϵ_p	0	H_{sp2}	0
H_{ss}	-4.30	$H_{pp\sigma 2}$	0.35
H_{sp}	4.98	$H_{pp\pi 2}$	-0.10
$H_{pp\sigma}$	6.38		
$H_{pp\pi}$	-2.66		

After determining all the elements of Hamiltonian matrix we have to solve the secular equation $det(H - ES) = 0$. S is the overlap matrix which is defined similar to Hamiltonian matrix but the diagonal elements are 1. In table 1.1, the coupling and overlap parameters for the Hamiltonian matrix is shown for the first nearest neighbour approximation [22]. The band structure created using these parameters is shown in figure 1.3a. In table 1.2 another set of parameters are shown. These parameters include second nearest neighbour atoms, but the overlap matrix is assumed to be identity matrix. The band structure of graphene generated using these parameters is shown in figure 1.3b. The bands around Fermi level are described quite well in both of the graphs and as the valance and conduction bands cross at K point. If a three dimensional graph for the band structure was drawn, these bands would have a conical shape as shown in figure 1.4. As it can be seen from the figure the Wigner-Seitz cell is a hexagon with K points in each corner. Therefore, there are Dirac cones at each corner of this hexagon. For these valance and conduction bands the energy dispersion relation is linear around Dirac point which can be given by;

$$E_{\pm}(\mathbf{q}) \cong \pm v_F|\mathbf{q}| + \Theta(q^2) \tag{1.24}$$

where $\mathbf{q}$ is the momentum measured relatively to the Dirac points and v_F is the Fermi velocity [8]. According to Wallace et al., the value of this velocity is around

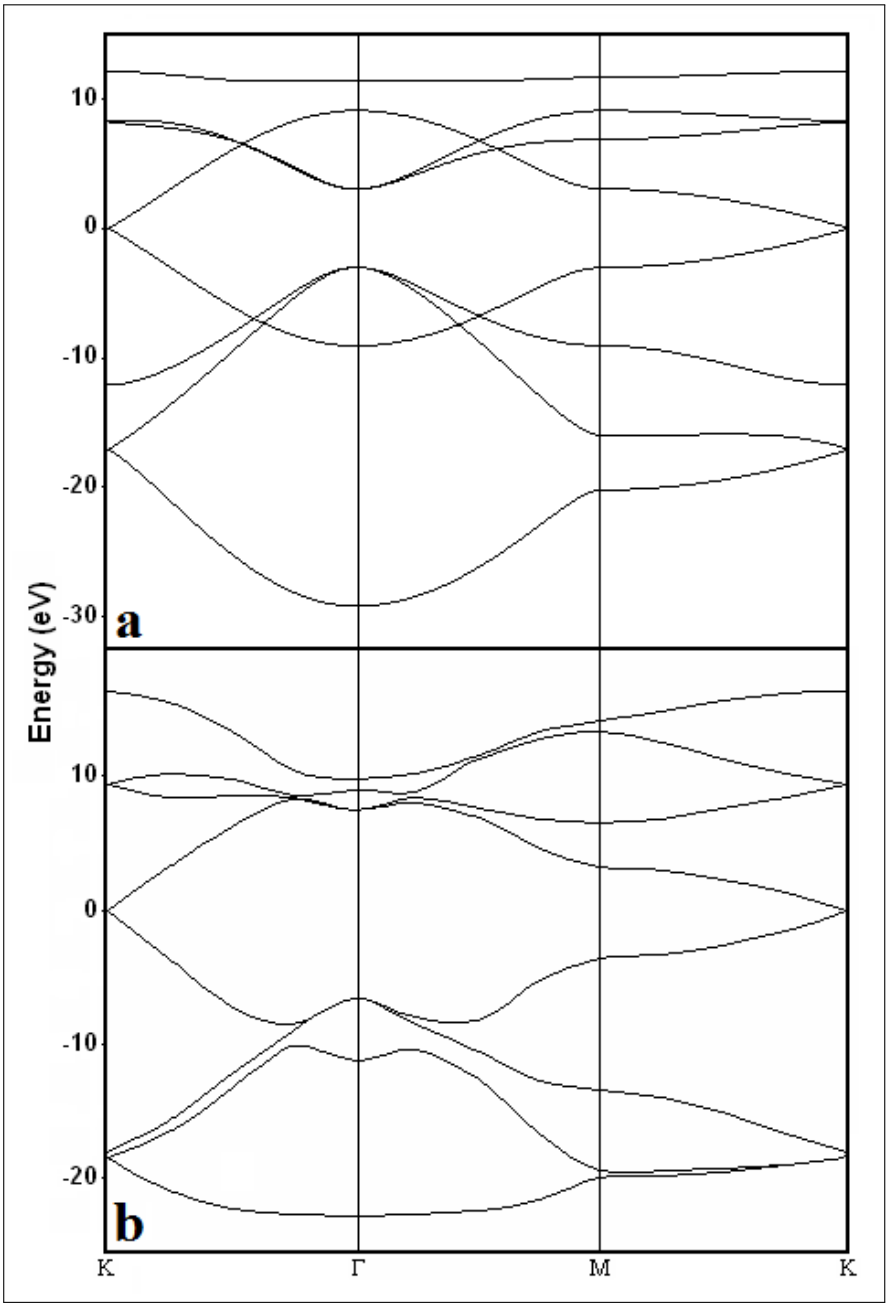

Figure 1.3: The calculated graphene electronic band structure along the high symmetry points Γ, K and M, using tight binding parameters a) including only first nearest neighbour hoppings shown in table 1.1, b) including first and second nearest neighbour hoppings shown in table 1.2.

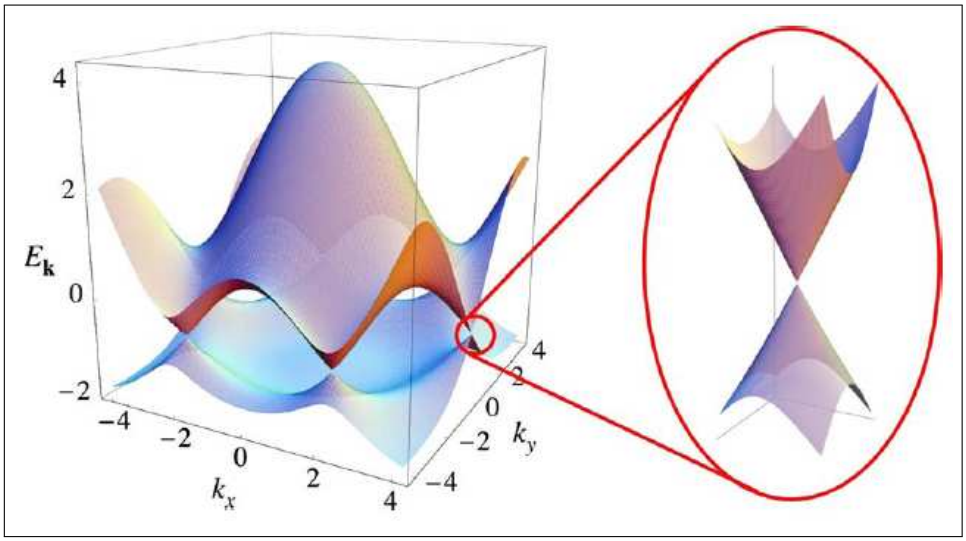

Figure 1.4: Three dimensional drawing of the electronic band structure of graphene over the Wigner-Seitz cell with a zoomed vision on K point to show the conical behaviour. (Reproduced from A.H. Castro Neto, F. Guinea, N.M.R. Peres, K.S. Novoselov and A.K. Geim, *Reviews of Modern Physics*, 81, 2009).

10^6 m/s, which is around $c/300$, c being the speed of light [23]. Notice that the Fermi velocity is independent of the energy or the momentum differing from usual case.

Massless Dirac equation describes the energy of ultra-relativistic particles. The energy spectrum of graphene resembles these particles near K points. A direct consequence of Dirac like spectrum is to have cyclotron mass which depends on the square root of the electronic charge density. The cyclotron mass, within the semiclassical approximation, can be defined as

$$m^* = \frac{1}{2\pi}\frac{\partial A(E)}{\partial E}, \tag{1.25}$$

where $A(E)$ is the area enclosed by orbit in momentum space. $A(E)$ is given by;

$$A(E) = \pi q^2 = \pi \frac{E^2}{v_F^2}. \tag{1.26}$$

Using equation 1.26 in equation 1.25, the cyclotron mass can be obtained as,

$$m^* = \frac{E}{v_F^2} = \frac{q}{v_F}. \tag{1.27}$$

The relation between the electronic charge density and the Fermi momentum is;

$$n = \frac{k_F^2}{\pi}. \tag{1.28}$$

Using equation 1.28 in equation 1.27 the cyclotron mass can be derived in terms of the square root of electronic charge density as follows;

$$m^* = \frac{\sqrt{\pi}}{v_F}\sqrt{n}. \tag{1.29}$$

The cyclotron mass can be calculated experimentally and the experimental data fits the calculated results providing an estimation for Fermi velocity around $c/300$ [8]. The observation of cyclotron mass being proportional to the square root of the charge density is an evidence for the existance of massless Dirac particles in graphene.

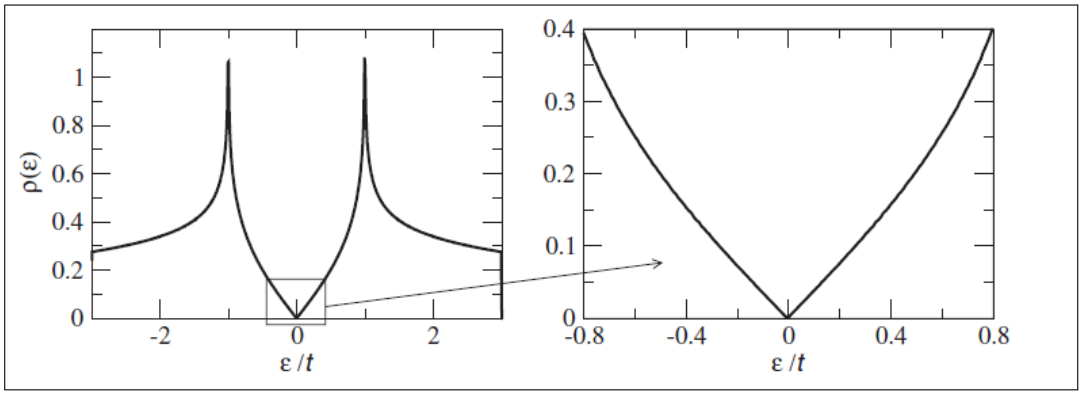

Figure 1.5: Total density of states of graphene computed from tight binding method with first nearest neighbour approximation on the left, and the neighbourhood of Fermi level is magnified on the right. (Reproduced from A.H. Castro Neto, F. Guinea, N.M.R. Peres, K.S. Novoselov and A.K. Geim, *Reviews of Modern Physics*, 81, 2009)

According to Neto et al. the calculated density of states is shown in figure 1.5 for the first nearest neighbour approximation [8]. Although the total density of states of graphene is asymmetric around Fermi level, it is approximately symmetric in the zoomed part of the figure showing linear dependency on energy, $\rho(\epsilon) \propto |\epsilon|$.

In short, graphene has a band structure such that at near K points valance and conduction bands touch each other at the Fermi level in a conical shape. As a result, electrons in graphene behave like Dirac Fermions reaching relativistic speeds for conduction.

1.2 Organization of the Thesis

Graphene is the basic structure in the thesis. Therefore, we must first understand the electronic properties of graphene. The first chapter of the thesis is the introduction chapter where the organization of the thesis and the electronic structure of graphene is explained.

We use ab-initio methods to calculate the properties of the graphitic structures we are interested in. These ab-initio methods are tight binding approach and density functional theory. The second chapter consists of the theoretical background of the ab-initio methods used.

If we can somehow cut the graphene layer, we can have a one or zero dimensional nano-sized ribbon-like structure out of it. These structures are called graphene nano-ribbons (GNRs). They can have band gaps depending on their shapes and sizes. GNRs are a huge research area by itself; energy band gap engineering [24–26], transport properties [27–30], impurities [31], effect of electric field [32–34], edge effects [35, 36] are some examples. There are even some works to use them as a molecular switch [37]. Although, graphene has zero band gap, Graphene nano-ribbons are finite sized graphenes and they can have finite band gaps so they are one of the new candidates for band gap engineering applications. Depending on their shapes and sizes, band gap values vary a lot. In the third chapter of this thesis, we present theoretical calculation of the band structures of Graphene nano-ribbons in both one (infinite in one dimension) and zero dimensions (finite in both dimensions) with the help of tight binding method for several graphene nano-ribbons including armchair (AGNR), zigzag (ZGNR) and chiral (CGNR) types. These graphene nano-ribbons are observed to have zero or finite

band gaps which increase with the decrease in the size of the ribbon making them much more suitable and strong candidate to replace silicon as a semiconductor. Also, the chirality angle has a major role in the change of the value of band gap and energy values.

Carbon nanotubes are rolled up versions of graphene. They are one dimensional materials showing different band gaps depending on their chiralitiy and radii [22]. Also, mechanical properties of CNTs are very unique. Although they are very soft in radial direction and can change their shape elastically, they are very stiff in axial direction [22]. After the discovery of CNTs by Iijima in 1991, the number of researches on it grew enormously [38]. There are many applications foreseen for CNTs such as nanosized electronics [39–41], Li ion batteries [42], hydrogen storage divices [43,44], molecular sensors [45,46], field emission sources [47], scanning probe microscope tips [48]. Up to date, junctions consisting of two crossed nanotubes have been produced [41]. It is shown that nanotubes make Y-junctions and T-junctions and kinks [49–51]. If we can control the growth of this junctions and kinks, we can produce the interested junction and make use of it as a device in nano-electronics. Therefore, it is very important to understand the growth mechanism of CNTs. It is reported that sulfur has a major role in this growth mechanism [49, 50, 52–54] of these junctions. Although sulfur plays a unique role in the growth of Y-junctions and kinks, if we replace sulfur with phosphorus under the same conditions it is shown that CNTs grow in a very low quantity [52]. In the forth chapter of this thesis, the difference between the effects of sulfur and phosphorus in the growth mechanism is investigated from DFT based first-principle calcultions.

The technological improvements in the size and variation of electronic devices made them cheap and available for the public. Today almost everyone living in a modern city has at least one cell phone. However, these kind of electronic devices need small but efficient power supplies with high capacity. Li ion batteries are commonly used as an energy storage device since they are rechargeable and very efficient. Graphitic carbon and related carbonaceous materials are prime candidates for electrode applications in such batteries having reversible capacity of a couple of hundreds Ah/kg [55, 56]. Also structural stability of carbon based

materials makes them even better with respect to other candidates such as metal oxide compounds [57]. In the fifth chapter of this thesis, we investigate lithium chemistry on graphitic structures and used the information to simulate carbon nanotube - lithium atom interaction [58].

The graphene layers consist of carbon atoms creating hexagons and in the unit cell there are two of them, namely A and B type atoms. These atoms have no difference in graphene, however, in highly oriented pyrolytic graphite (HOPG), which is a three dimensional structure, they do. In HOPG each consecutive graphene layers are shifted such that A atoms lie on top of each other, whereas, B atoms lie on top of the center of the hexagon. In scanning tunnelling microscope (STM) image of HOPG this situation has a stunning effect. In those images only one type of atoms is visible [59, 60] which are widely accepted to be B type. The proposed explanation is the charge density difference, which is reasonable since STM plots the charge density profiles. Apart from that, large super-periodicities of HOPG structures are reported [61–67]. There may be many possible physical origins for them but we are interested in Moire pattern assumption [61–63, 68], which briefly states that the top most layer of the graphite is rotated with respect to the layers underneath. In the sixth chapter of this thesis we first try to explore the geometry of Moire patterns and then investigate the charge profile to explain the related STM images. Finally, in the seventh chapter we conclude the thesis.

Chapter 2

Computational Methods

The electronic band structures of graphene nano-ribbons discussed in chapter three are calculated from tight binding model with second nearest neighbour approximation. Density functional theory is employed in the calculations subject to chapter four, five and six. Therefore, in this chapter, we introduce background information on the computational methods used in this thesis.

2.1 Tight-Binding Method

There are many methods within energy band theory to determine the band structures of solids. Green's functions method, density functional theory and tight-binding method are some examples. Among these methods the tight-binding (TB) model is simple but very instructive and accurate enough approach for the description of electronic structure of many systems. The tight-binding model assumes that the approximate set of wave functions based upon superposition of the wave functions for isolated atoms located at each atomic site is enough to describe the system. Therefore, the method is very closely related to the linear combination of atomic orbitals method (LCAO) used in chemistry. The tight-binding model can be applied to a wide variety of solids. In many cases, this model is accurate enough for qualitative results. Furthermore, even when

this approach fails to describe the system, it is still useful to use by combining with other methods whose results are more accurate. Although, the tight-binding model is a simple approach, the model also provides a basis for more advanced calculations.

The tight-binding model is more accurate in the systems where the electrons are tightly bound to their atoms as the name suggests. Therefore, these electrons should have limited interaction with the potentials and the states originating from the surrounding atoms in the solid. As a natural result of this low interaction, the wave functions of the electron will be very close to the atomic orbitals of the atom that it belongs to. Then, it can be assumed that the restricted Hilbert space is spanned by atomic orbitals and they are sufficient enough to describe the wave functions. The wave functions of the electron can be written in terms of the linear combination of the atomic orbitals with a weight function.

In a periodic medium, the potential inside the unit cell is repeated just like the atoms. Bloch's theorem suggests that the wave-function of the lattice should have a translational symmetry and satisfy the following equation;

$$T_{\vec{a}_i}\Psi = e^{i\vec{k}\cdot\vec{a}_i}\Psi \tag{2.1}$$

where $T_{\vec{a}_i}$ is a translational operation along the lattice vector $\vec{a_i}$ $(i = 1, 2, 3)$, Ψ is the wave function and $\vec{k}$ is the wave vector. In tight-binding method we use atomic orbitals to describe this function. Therefore, a tight-binding Bloch function is given by;

$$\Phi_{lj}(\vec{k}, \vec{r}) = \frac{1}{\sqrt{N}} \sum_{\vec{R}}^{N} e^{i\vec{k}\cdot\vec{R}} \psi_l(\vec{r} - \vec{t_j} - \vec{R}),\ (j = 1, ..., n), \tag{2.2}$$

with the summation running over all the N unit cells in the crystal. In equation 2.2, $\vec{t_j}$ is the basis vector related to the position of the j^{th} atom with n atoms in the unit cell, ψ_l is the atomic wave function of state l and $\vec{R}$ is the lattice vector. Therefore, we assume that the atomic wavefunctions in the unit cell weighted by a phase factor summed over the lattice vectors describe Bloch functions in the solid. In order to verify that these states have Bloch character we look for

$\Phi_{lj}(\vec{k}, \vec{r}+\vec{R}')$ as follows;

$$\begin{aligned}
\Phi_{lj}(\vec{k}, \vec{r}+\vec{R}') &= \frac{1}{\sqrt{N}} \sum_{\vec{R}}^{N} e^{i\vec{k}\cdot\vec{R}} \psi_l((\vec{r}+\vec{R}') - \vec{t_j} - \vec{R}) \\
&= e^{i\vec{k}\cdot\vec{R}'} \frac{1}{\sqrt{N}} \sum_{\vec{R}}^{N} e^{i\vec{k}\cdot(\vec{R}-\vec{R}')} \psi_l(\vec{r} - \vec{t_j} - (\vec{R}-\vec{R}')) \\
&= e^{i\vec{k}\cdot\vec{R}'} \frac{1}{\sqrt{N}} \sum_{\vec{R}''}^{N} e^{i\vec{k}\cdot\vec{R}''} \psi_l(\vec{r} - \vec{t_j} - \vec{R}'') = e^{i\vec{k}\cdot\vec{R}'} \Phi_{lj}(\vec{k}, \vec{r}) \quad (2.3)
\end{aligned}$$

where $\vec{R}'' = \vec{R} - \vec{R}'$ is another lattice vector. The n^{th} eigenfunction in the solid can be expanded by the linear combination of Bloch functions as follows;

$$\Psi^n(\vec{k}, \vec{r}) = \sum_{lj} C^n_{lj}(\vec{k}) \Phi_{lj}(\vec{k}, \vec{r}) \quad (2.4)$$

and all that remains to do is determine the coefficients $C^n_{lj}(\vec{k})$. The n^{th} eigenvalue, i.e., the n^{th} energy value as a function of wave vector $\vec{k}$ is given by;

$$E^n(\vec{k}) = \frac{\langle \Psi^n_{\vec{k}} | H | \Psi^n_{\vec{k}} \rangle}{\langle \Psi^n_{\vec{k}} | \Psi^n_{\vec{k}} \rangle} \quad (2.5)$$

where H is the Hamiltonian of the solid.

Substituting equation 2.4 into equation 2.5, we obtain;

$$E^n(\vec{k}) = \frac{\sum_{ljl'j'} H_{ljl'j'}(\vec{k}) C^{n*}_{lj} C^n_{l'j'}}{\sum_{ljl'j'} S_{ljl'j'}(\vec{k}) C^{n*}_{lj} C^n_{l'j'}} \quad (2.6)$$

where l and l' denote the atomic orbitals and j and j' represents the atoms in the unit cell. The integrals over the Bloch orbitals, $H_{ljl'j'}(\vec{k}) = \langle \Phi_{lj} | H | \Phi_{lj'} \rangle$ and $S_{ljl'j'}(\vec{k}) = \langle \Phi_{lj} | \Phi_{lj'} \rangle$ are called transfer integral matrices and overlap integral matrices respectively. Minimizing the eigenvalue by taking derivative with respect to C^{n*}_{lj}, multiplying both sides of the equation by $\sum_{ljl'j'} S_{ljl'j'}(\vec{k}) C^{n*}_{lj} C^n_{l'j'}$ and inserting $E^n(\vec{k})$ from equation 2.6 into this equation, we obtain equation 2.8 as follows;

$$\frac{\partial E^n(\vec{k})}{\partial C^{n*}_{lj}} = \frac{\sum_{l'j'} H_{ljl'j'}(\vec{k}) C^n_{l'j'}}{\sum_{ljl'j'} S_{ljl'j'}(\vec{k}) C^{n*}_{lj} C^n_{l'j'}} - \frac{\sum_{ljl'j'} H_{ljl'j'}(\vec{k}) C^{n*}_{lj} C^n_{l'j'}}{(\sum_{ljl'j'} S_{ljl'j'}(\vec{k}) C^{n*}_{lj} C^n_{l'j'})^2} \sum_{l'j'} S_{ljl'j'}(\vec{k}) C^n_{l'j'} = 0 \quad (2.7)$$

$$\sum_{l'j'} H_{ljl'j'}(\vec{k})C^n_{l'j'} = E^n(\vec{k}) \sum_{l'j'} S_{ljl'j'}(\vec{k})C^n_{l'j'}. \tag{2.8}$$

If we define the coefficients as a column vector with elements $C^n_{l'j'} = (C^n_{1j'}, ..., C_{l'j'}, ...)$ by transporting the right hand side to the left, we have $(H - E^n(\vec{k})S)C^n_{l'j'} = 0$. If the inverse of $(H - E^n(\vec{k})S)$ exists, this means that $C^n_{l'j} = 0$, which represents the null vector, and the no wavefunction is obtained. Hence, the eigenfunction is only given when the inverse matrix does not exist, which means the following equation should hold;

$$det|H - ES| = 0, \tag{2.9}$$

which is called the secular equation. By solving the secular equation, we can obtain the energy eigenvalues $E^n(\vec{k})$, for a given $\vec{k}$.

In short, in order to make use of tight-binding method in the band structure calculation, we first specify the unit cell, unit vectors, the basis set and the atomic orbitals to be used. Then, we calculate the reciprocal lattice vectors and select the high symmetry directions in the Brillouin zone. After that, we calculate the transfer and the overlap matrix elements and solve the secular equation for the selected $\vec{k}$ points to obtain the energy eigenvalues and the coefficients.

2.2 Density Functional Theory

Density functional theory is a quantum mechanical theory used in physics and chemistry. This theory tries to investigate the electronic structure of many-body systems based on the functionals that depends on the charge density function. In general, many-body systems consist of a collection of atoms and electrons interacting among themselves. Therefore, a many-body Schrödinger equation contains $3N + 3N_e$ degrees of freedom where N is the number of atoms and N_e is the number of electrons without taking spin degrees of freedom. The Hamiltonian for many-body Schrödinger equation can be written in atomic units as;

$$H = -\sum_{I=1}^{N} \frac{\nabla_I^2}{2M_I} - \sum_{i=1}^{N_e} \frac{\nabla_i^2}{2} + \sum_{J=1}^{N-1} \sum_{I=J+1}^{N} \frac{Z_I Z_J}{|\vec{R_I} - \vec{R_J}|} + \sum_{j=1}^{N_e-1} \sum_{i=j+1}^{N_e} \frac{1}{|\vec{r_i} - \vec{r_j}|} - \sum_{I=1}^{N} \sum_{i=1}^{N_e} \frac{Z_I}{|\vec{R_I} - \vec{r_i}|} \tag{2.10}$$

where M_I is the mass of the nuclei, Z_I is the number of protons in I^{th} nucleus, $\vec{R_I}$ and $\vec{r_i}$ denote the positions of nuclei and electrons. The first two terms represent the kinetic energy of the nuclei and the electrons respectively. The remaining terms are the electrostatic Coulomb interaction of nucleus-nucleus, electron-electron and nucleus-electron respectively. With this Hamiltonian, the Schrödinger equation can be written as follows;

$$H\Psi(\mathbf{r}, \mathbf{R}) = E\Psi(\mathbf{r}, \mathbf{R}). \tag{2.11}$$

Here Ψ is the wave-function of the many-body system and E is the energy eigenstate for the state. In practice, it is impossible to solve this problem analytically. Even with the help of numerical methods it is possible to solve only a very limited number of cases in which there are a few electrons and nuclei. This problem arises because of two main reasons. First, this many body Schrödinger equation (equation 2.11) is not separable, i.e. it cannot be decoupled into a set of independent equations because of Coulombic correlations. Therefore, in general one has to deal with $3N + 3N_e$ coupled degrees of freedom disregarding the spin. The second reason is that the particles that form the system can obey different statistics, i.e. electrons are fermions which should obey the Fermi-Dirac statistics and nuclei can be fermions or bosons which can be distinguishable or indistinguishable. These difficulties can be overcome by the help of approximations.

2.2.1 Adiabatic Approximation

Adiabatic approximation, which is also know as Bohr-Oppenheimer Approximation origins from the large difference between the mass of the nuclei and electrons. Mass of a nucleus is at least three orders of magnitude greater than the mass of an electron. Therefore, nuclei are much heavier particles than the electrons and the response of a nucleus to the change in the environment is much slower than that of an electron. Then, while electrons can instantaneously follow the changes, nuclei stay in the same stationary state. This stationary state will vary in time due to the Coulombic coupling and as the nuclei follow their dynamics the electrons will instantaneously arrange their wave-functions accordingly. Hence, the full

wave-function can be separated into electronic and nuclear wave-functions [69];

$$\Psi(\mathbf{r},\mathbf{R}) = \chi(\mathbf{r},\mathbf{R})\Phi(\mathbf{R}) \tag{2.12}$$

where χ is the electronic and Φ is the nuclear wave-functions. This is called the adiabatic approximation. The decoupled adiabatic Schrödinger equations become;

$$\begin{aligned} H\Psi(\mathbf{r},\mathbf{R}) = H\chi(\mathbf{r},\mathbf{R})\Phi(\mathbf{R}) &= E\chi(\mathbf{r},\mathbf{R})\Phi(\mathbf{R}), \\ \{T_e + V_{ee}(\mathbf{r}) + V_{Ne}(\mathbf{r},\mathbf{R})\}\chi_n(\mathbf{r},\mathbf{R}) &= \epsilon_n(\mathbf{R})\chi_n(\mathbf{r},\mathbf{R}), \qquad (2.13) \\ \{T_N + V_{NN}(\mathbf{R}) + \epsilon_n\}\Phi_n(\mathbf{R}) &= E_n(\mathbf{R})\Phi_n(\mathbf{R}). \qquad (2.14) \end{aligned}$$

In equations 2.13 and 2.14, T represents the kinetic energy and V represents the Coulomb potential. The Coulombic interactions between the nuclei and the electrons enter the electronic Hamiltonian in equation 2.13. However, since nuclei are in stationary state, nuclear positions enter this equation as parameters and by varying these positions adiabatically the potential energy surface of the electronic ground state can be formed and the motion of the nuclei can be solved. Then, the following equations are obtained;

$$\begin{aligned} \{T_e + V_{ee}(\mathbf{r}) + V_{Ne}(\mathbf{r},\mathbf{R})\}\chi_0(\mathbf{r},\mathbf{R}) &= \epsilon_0(\mathbf{R})\chi_0(\mathbf{r},\mathbf{R}), \qquad (2.15) \\ \{T_N + V_{NN}(\mathbf{R}) + \epsilon_0(\mathbf{R})\}\Phi_n(\mathbf{R},t) &= i\hbar\frac{\partial}{\partial t}\Phi_n(\mathbf{R},t). \qquad (2.16) \end{aligned}$$

If the nuclei are treated as classical particles assuming that they are sufficiently localized, the connection between classical and quantum mechanics can be achieved. Then, the quantum mechanical analog of Newton's equation can be obtained by Ehrenfest's theorem of the mean value of the position operator as follows;

$$M_I\frac{\langle\partial^2\mathbf{R}_I\rangle}{\partial t^2} = -\langle\nabla_I E_0(\mathbf{R})\rangle, \tag{2.17}$$

where

$$E_0(\mathbf{R}) = \epsilon_0(\mathbf{R}) + V_{NN}(\mathbf{R}). \tag{2.18}$$

Contributions from both the ion-ion interaction and the gradient of the electronic total energy of the ground state are contained in the force $-\langle\nabla_I E_0(\mathbf{R})\rangle$ in equation 2.17. The gradient of the electronic total energy of the ground state can be

calculated from Hellman-Feynman theorem;

$$\begin{aligned}\langle\nabla_I\epsilon_0(\mathbf{R})\rangle &= \nabla_I\langle\chi_0|H_e(\mathbf{R})|\chi_0\rangle \\ &= \langle\nabla_I\chi_0|H_e(\mathbf{R})|\chi_0\rangle + \langle\chi_0|H_e(\mathbf{R})|\nabla_I\chi_0\rangle + \langle\chi_0|\nabla_I H_e(\mathbf{R})|\chi_0\rangle \\ &= \langle\chi_0|\nabla_I H_e(\mathbf{R})|\chi_0\rangle. \end{aligned} \tag{2.19}$$

The first and second terms are zero due to the variational property of the ground state.

2.2.2 Hartree and Hartree-Fock Approximation

With the Born-Oppenheimer approximation and the classical nuclei approximation, nuclear part of the many-body Schrödinger equation is solved, however, due to the complex electron-electron interaction the electronic part still remains as a difficult task. The first approximation to this problem is proposed by Hartree in 1928 [70]. According to Hartree approximation, the electronic wavefunction can be written as the product of single electron wavefunctions;

$$\chi(\mathbf{r}) = \prod_i \phi_i(\mathbf{r}_i). \tag{2.20}$$

Each electron is then subjected to an effective potential which is created by the nuclei and other electrons. Hence, the Schrödinger equation for the single electron can be written as;

$$\left(-\frac{\hbar^2}{2m}\nabla^2 + V_{eff}^{(i)}(\mathbf{r})\right)\phi_i(\mathbf{r}) = \epsilon_i\phi_i(\mathbf{r}) \tag{2.21}$$

where the effective potential is the sum of the potentials of nuclei and other electrons as follows;

$$V_{eff}^{(i)}(\mathbf{r}) = V_{Ne}(\mathbf{r}) + \int \frac{\sum_{j\neq i}|\phi_j(\mathbf{r}')|^2}{|\mathbf{r}-\mathbf{r}'|}d\mathbf{r}'. \tag{2.22}$$

In equation 2.22, $V_{Ne}(\mathbf{r})$ stands for the Coulombic interaction between the electron and the nuclei, and $|\phi_j(\mathbf{r}')|^2$ is the charge density n_j of the j^{th} electron. Notice that i^{th} electron is excluded in the summation as $i \neq j$ so that the equation is self interaction free. Since the electron-electron interaction is counted twice in the

effective potential, the total energy of the system by the Hartree approximation can be written as;

$$E_H = \sum_i^{N_e} \epsilon_i - \frac{1}{2} \int \int \frac{n(\mathbf{r}) n(\mathbf{r}')}{|\mathbf{r} - \mathbf{r}'|} d\mathbf{r} d\mathbf{r}'. \tag{2.23}$$

The charge density is expressed in terms of the electronic eigenstates and the effective potential, so the Schrödinger equation is expressed in terms of the charge density. By solving the Schrödinger equation, we can re-calculate the electronic eigenstates. Therefore, the electronic Schrödinger equation reduces to a self-consistent problem. The procedure can be summarized as follows; first, an appropriate trial wavefunction is choosen. Then, from this wavefunction the charge density so and effective potential can be obtained. From the charge density, total energy of the system can be calculated, and the Schrödinger equation can be solved to obtain a new wavefunction. Repeating the same procedure, self consistency can be achieved within the desired accuracy by checking the energy and the wavefunction difference of the consecutive steps.

One of the problems of Hartree approximation is that it does not include the Fermionic nature of electrons. The Hartree-Fock method overcomes this problem and makes the electronic wavefunction antisymmetric by the introduction of Slater determinant [71]. According to Hartree-Fock approximation, the total wavefunction can be written as the determinant of the matrix containing single electron wavefunctions as follows;

$$\chi(\mathbf{r}) = \frac{1}{\sqrt{N!}} \begin{vmatrix} \phi_1(\mathbf{r}_1, \sigma_1) & \phi_1(\mathbf{r}_2, \sigma_2) & ... & \phi_1(\mathbf{r}_N, \sigma_N) \\ \phi_2(\mathbf{r}_1, \sigma_1) & \phi_2(\mathbf{r}_2, \sigma_2) & ... & \phi_2(\mathbf{r}_N, \sigma_N) \\ ... & ... & ... & ... \\ \phi_N(\mathbf{r}_1, \sigma_1) & \phi_N(\mathbf{r}_2, \sigma_2) & ... & \phi_N(\mathbf{r}_N, \sigma_N) \end{vmatrix}. \tag{2.24}$$

In equation 2.24, σ_j represents the spin of j^{th} electron. The exchange interaction of electrons included in this formalism gives rise to an additional coupling term in the Schrödinger equation and the energy of the system is reduced. The electronic

Schrödinger equation for the i^{th} electron can be rewritten as;

$$\Big(-\nabla^2 + V_{Ne}(\mathbf{r}) + \int \frac{\sum_{\sigma,j\neq i} |\phi_j(\mathbf{r}',\sigma)|^2}{|\mathbf{r}-\mathbf{r}'|} d\mathbf{r}' \Big)\phi_i(\mathbf{r},\sigma)$$
$$- \int \frac{\sum_{\sigma,j\neq i} \phi_j^*(\mathbf{r}',\sigma)\phi_i(\mathbf{r}',\sigma)}{|\mathbf{r}-\mathbf{r}'|} d\mathbf{r}' \phi_i(\mathbf{r},\sigma) = \epsilon_i \phi_i(\mathbf{r},\sigma). \tag{2.25}$$

In equation 2.25, the first two terms on the left hand side are the Hartree terms and the last term on the left hand side is the exchange term. Notice that, there is no self interaction of electrons in the equation due to cancellations. Calculating the electronic properties of a system with Hartree-Fock equation is similar to the procedure applied for Hartree equation where the wavefunctions are generated through self-consistent iteration method. The greatest problem with both of these methods is that the computation time and cost increases rapidly as the number of interacting particles increase. Also, these methods over-estimate the band and HOMO-LUMO gap values.

2.2.3 Thomas-Fermi Theory

One of the first attempts to write the total energy of a system in terms of charge density function was done by Thomas and Fermi in 1927 [72, 73]. The theory is based on writing the total kinetic energy term of the electrons as a functional of electron density. Thomas and Fermi assume that the electrons of the system can be treated as homogeneous electron gas and the density is related to fermi energy as follows;

$$n = 2^{3/2}\frac{\epsilon_F^{3/2}}{3\pi^2} \Rightarrow \epsilon_F = n^{2/3}\frac{(3\pi^2)^{2/3}}{2}. \tag{2.26}$$

The kinetic energy density is $t(\vec{r}) = 3n(\vec{r})\epsilon_F/5$. Therefore, total kinetic energy of the electrons can be expressed in terms of charge density as;

$$T_{TF} = C_F \int n^{5/3}(\mathbf{r}) d\mathbf{r} \tag{2.27}$$

where $C_F = 3(3\pi)^2/10$. Neglecting the contribution of the exchange and correlation of electrons in total energy, we can obtain the following Thomas-Fermi total energy as a functional of charge density,

$$E_{TF}[n] = C_F \int n^{5/3}(\mathbf{r}) d\mathbf{r} + \int V(\mathbf{r}) n(\mathbf{r}) d\mathbf{r} + \frac{1}{2}\int\int \frac{n(\mathbf{r})n(\mathbf{r}')}{|\mathbf{r}-\mathbf{r}'|} d\mathbf{r} d\mathbf{r}'. \tag{2.28}$$

Using the variation principle and the constraint that the number of electrons is constant one can introduce Lagrange multipliers and minimize the total Thomas-Fermi energy with respect to charge density to obtain;

$$\frac{\delta}{\delta n(\mathbf{r})}\left(E_{TF} - \mu \int n(\mathbf{r}) d\mathbf{r}\right) = 0,$$
$$\mu = \frac{5}{3} C_F n^{2/3}(\mathbf{r}) + V(\mathbf{r}) + \int \frac{n(\mathbf{r}')}{|\mathbf{r} - \mathbf{r}'|} d\mathbf{r}' \tag{2.29}$$

where μ is the chemical potential.

Without taking the exchange and correlation potentials into account and expressing the kinetic energy term in a crude way, the Thomas-Fermi theory is a poor model. However, it is a very important theory since it constructs the basis for the modern density functional theory.

2.2.4 Hohenberg-Kohn Theory

The basis of density functional theory is that the electronic properties of a many-body system can be defined as a functional of ground state charge density. As a result of the Born-Oppenheimer approximation, we treat the potential due to nuclei as an external potential and express as the summation of Coulomb interactions of all electrons and nuclei. If we define the remainder of the electronic Hamiltonian as F which contains kinetic energy and the Coulombic interaction of the electrons, we have;

$$H = V_{Ne}(\mathbf{r}) + T_e + V_{ee}(\mathbf{r}) = V_{ext} + F. \tag{2.30}$$

F is the same for all N-electron systems, hence, the Hamiltonian and the ground state wavefunction are completely determined by N and V_{ext}. The first statement of Hohenberg and Kohn is that, V_{ext} is uniquely determined, except for a constant shift in energy, by the ground state electronic density n_0 [74]. The proof is as follows; assume that there exists a second external potential V'_{ext} with the ground state $|\Psi'_0\rangle$ which gives rise to the same ground state density $n_0(\mathbf{r})$. Then, the ground state energies are $E_0 = \langle\Psi_0|H|\Psi_0\rangle$ and $E'_0 = \langle\Psi'_0|H'|\Psi'_0\rangle$, where

$H = V_{ext} + F$ and $H' = V'_{ext} + F$. Taking $|\Psi'_0\rangle$ as a trial wavefunction for H, we obtain the strict inequality by variational principle;

$$\begin{aligned} E_0 < \langle \Psi'_0|H|\Psi'_0\rangle &= \langle \Psi'_0|H'|\Psi'_0\rangle + \langle \Psi'_0|H - H'|\Psi'_0\rangle \\ &= E'_0 + \int n_0(\mathbf{r})(V_{ext}(\mathbf{r}) - V'_{ext}(\mathbf{r}))d\mathbf{r}. \end{aligned} \tag{2.31}$$

On the other hand, taking $|\Psi_0\rangle$ as a trial wavefunction for H' we obtain;

$$\begin{aligned} E'_0 < \langle \Psi_0|H'|\Psi_0\rangle &= \langle \Psi_0|H'|\Psi_0\rangle - \langle \Psi_0|H - H'|\Psi_0\rangle \\ &= E_0 - \int n_0(\mathbf{r})(V_{ext}(\mathbf{r}) - V'_{ext}(\mathbf{r}))d\mathbf{r}. \end{aligned} \tag{2.32}$$

Adding equation 2.31 to equation 2.32 we obtain $E_0 + E'_0 < E_0 + E'_0$. Then, the first assumption that there can exist a second external potential V'_{ext} with the ground state $|\Psi'_0\rangle$ which gives rise to the same ground state density $n_0(\mathbf{r})$ is wrong and the statement is true. Therefore, there cannot be two different external potentials up to a constant shift, which give rise to the same non-degenerate ground state electronic density. In other words, the ground state determines the external potential within a constant, thus, energy and external potentials are functionals of $n_0(\mathbf{r})$. The second statement of Hohenberg and Kohn is that the density that minimizes the total energy is the exact ground state [74]. In order to prove this we write the energy functional in terms of external potential as follows;

$$E[n(\mathbf{r})] = \int n(\mathbf{r})V_{ext}(\mathbf{r})d\mathbf{r} + F[n(\mathbf{r})] \tag{2.33}$$

where $F[n(\mathbf{r})]$ is an unknown, but otherwise universal functional of $n(\mathbf{r})$. Number of electrons N and the external potential $V_{ext}(\mathbf{r})$ determines H and thus Ψ which ultimately means Ψ is a functional of $n(\mathbf{r})$. Hence, the expectation value of F is also a functional of $n(\mathbf{r})$, i.e., $F[n(\mathbf{r})] = \langle \Psi|F|\Psi\rangle$. Now, if we define energy functional for another electronic density $n'(\mathbf{r})$ and apply the variational principle we obtain;

$$E[n'(\mathbf{r})] = \int n'(\mathbf{r})V_{ext}(\mathbf{r})d\mathbf{r} + F[n'(\mathbf{r})] \tag{2.34}$$

and consequently,

$$\langle \Psi'|F|\Psi'\rangle + \langle \Psi'|V_{ext}|\Psi'\rangle > \langle \Psi|F|\Psi\rangle + \langle \Psi|V_{ext}|\Psi\rangle. \tag{2.35}$$

Using the expectation value of F in equation 2.35 the following inequality can be formed;

$$\begin{aligned} F[n'(\mathbf{r})] + \langle \Psi' | V_{ext} | \Psi' \rangle &= F[n'(\mathbf{r})] + \int n'(\mathbf{r}) V_{ext}(\mathbf{r}) d\mathbf{r} > \\ F[n(\mathbf{r})] + \langle \Psi | V_{ext} | \Psi \rangle &= F[n(\mathbf{r})] + \int n(\mathbf{r}) V_{ext}(\mathbf{r}) d\mathbf{r}. \end{aligned} \tag{2.36}$$

Combining equation 2.36 with equation 2.34, we can identify the following inequality;

$$E[n'(\mathbf{r})] > E[n(\mathbf{r})] = E[n_0(\mathbf{r})]. \tag{2.37}$$

Therefore, the energy for the ground state density $n_0(\mathbf{r})$ is indeed lower than the energy for any other state $n'(\mathbf{r})$.

2.2.5 Kohn-Sham Equations

Kohn and Sham make use of the theories explained above to suggest a solution to find the wavefunctions of a many-body system. They stated that the total energy of an interacting system can be calculated using the equations describing non-interacting particles [75]. In order to do this, the total energy functional is written in terms of electronic density as in equation 2.33. In equation 2.33, $F[n(\mathbf{r})]$ describes the kinetic energy and the electron-electron interaction of non interacting particles as well as including the exchange and correlation term as follows;

$$F[n(\mathbf{r})] = T_e + V_{ee} = T_s + V_s + V_{XC} \tag{2.38}$$

where T_s and V_s are the kinetic and potential energy of non-interacting particles and V_{XC} includes the energy from all the exchange and correlation of the electrons. Then, the total energy as a functional of electronic density can be written as

$$\begin{aligned} E_{tot}[n(\mathbf{r})] \quad &= -\frac{1}{2} \sum_{i,\sigma} \int \phi_i^*(\vec{r}) \nabla^2 \phi_i(\vec{r}) d\mathbf{r} + \int V_{ext} n(\mathbf{r}) d\mathbf{r} \\ &+ \int \frac{n(\mathbf{r}) n(\mathbf{r}')}{|\mathbf{r} - \mathbf{r}'|} d\mathbf{r} d\mathbf{r}' + E_{XC}[n(\mathbf{r})], \end{aligned} \tag{2.39}$$

where E_{XC} represents the exchange-correlation energy. The exchange and correlation energy can be minimized with respect to electronic density to get exchange-correlation potential;

$$V_{XC}(\mathbf{r}) = \frac{\delta E_{XC}[n(\mathbf{r})]}{\delta n(\mathbf{r})}. \tag{2.40}$$

Then, the single particle Shrödinger equation can be written as;

$$\left(-\frac{1}{2}\nabla^2 + V_{ext}(\mathbf{r}) + V_H + V_{XC}(\mathbf{r}) \right) \phi_i(\mathbf{r}) = \epsilon_i \phi_i(\mathbf{r}) \tag{2.41}$$

where

$$V_H = \int \frac{n(\mathbf{r}')}{|\mathbf{r} - \mathbf{r}'|} d\mathbf{r}' \tag{2.42}$$

is called the Hartree potential. This equation is very important because it reduces the many-body electron system into non-interacting electrons system, where the electrons feel the effective potential of other electrons and nuclei, hiding the exchange and correlation of electrons inside the exchange and correlation potential. If the exchange and correlation energy was known exactly, the total energy of the system could be calculated without approximations. Since the exchange and correlation energy functional is not known explicitly, some approximations are made for the exchange-correlation potential.

2.2.6 Approximations For Exchange-Correlation Potential

The major problem of density functional theory is that the exact functionals for exchange and correlation energy are not known except for the free electron gas whose exchange functional is known. However, making approximations is possible and these approximations work quite well in the calculation of certain physical quantities. The simplest and most widely used approximation is the local density approximation (LDA) or more generally local spin density approximation (LSDA). In this approximation, the exchange-correlation energy of an inhomogeneous system is described with an assumption that the exchange-correlation energy per electron is similar to that of the exchange-correlation energy per electron of a homogeneous electron gas. Therefore, the energy as a functional of

density can be written as;

$$E_{XC}^{LSDA}[n^{\uparrow}n^{\downarrow}] = \int n(\mathbf{r})\varepsilon_{XC}^{hom}(n^{\uparrow}(\mathbf{r}), n^{\downarrow}(\mathbf{r}))d\mathbf{r}, \tag{2.43}$$

where ε_{XC}^{hom} is the exchange and correlation function of a homogeneous electron gas.

General features of LDA are as follows; it favoures more homogeneous systems, it gives over-binding molecules and solids, chemical trends are estimated usually correctly and for covalent, ionic and metallic systems, although dielectric properties are overestimated, geometry of the system and phonon frequencies are well predicted.

LDA is very successful to predict the properties of many systems, especially those where the electronic density is uniform, however, there are some features that LDA fails to reproduce such as; weak molecular bonds where the bonding region has inhomogeneous electronic density, Van der Waals interaction and underestimation of the energy band gap in semiconductors.

In order to improve LSDA, which makes use of the charge density at a coordinate, further for some cases, generalized gradient approximation (GGA), which takes into account the gradient of the density at the same coordinate as well, is proposed. The exchange energy functional for GGA can be rewritten as;

$$E_{XC}^{GGA}[n^{\uparrow}n^{\downarrow}] = \int n(\mathbf{r})\varepsilon_{XC}^{hom}(n^{\uparrow}(\mathbf{r}), n^{\downarrow}(\mathbf{r}), \vec{\nabla}n^{\uparrow}(\mathbf{r}), \vec{\nabla}n^{\downarrow}(\mathbf{r}))d\mathbf{r}. \tag{2.44}$$

There are many forms of $\varepsilon_{XC}^{hom}(n^{\uparrow}(\mathbf{r}), n^{\downarrow}(\mathbf{r}), \vec{\nabla}n^{\uparrow}(\mathbf{r}), \vec{\nabla}n^{\downarrow}(\mathbf{r}))$ proposed such as Becke (B88) [76], Perdew and Wang (PW91) [77] and Perdew, Burke and Enzerhof (PBE) [78]. Although, GGA sometimes worsen the results with respect to LDA, it estimates binding and atomic energies, bond lengths and angles and the properties of hydrogen bonded systems except for F-H bond better.

Both of the approximations has advantages and disadvantages over each other. Hence, it is better to check both of them to compare with the real system for the particular case interested.

2.2.7 Plane Wave Basis Set

In order to be able to solve equation 2.41, we have to expand the wave function in terms of some basis set at each $\vec{k}$. In density functional theory, we choose plane wave basis set which is very convenient in crystals due to periodic potential and also they can expand the wavefunction regardless of the atom type. Another important property of the plane wave basis set is that they are easy to work in reciprocal space so that computational errors decrease significantly.

According to Bloch's Theorem, under a periodic potential, the electronic wave function can be written as

$$\phi_i(\mathbf{r}) = e^{i\mathbf{k}\cdot\mathbf{r}} f_i(\mathbf{r}), \tag{2.45}$$

where $f_i(\mathbf{r})$ is a periodic function with the periodicity of the lattice. This function can be extended in terms of the plane wave basis set with reciprocal lattice vectors $\mathbf{G}$ as

$$f_i(\mathbf{r}) = \sum_{\mathbf{G}} c_{i,\mathbf{G}} e^{i\mathbf{G}\cdot\mathbf{r}}. \tag{2.46}$$

In equation 2.46, $c_{i,\mathbf{G}}$ are the plane wave coefficients. By combining equations 2.45 and 2.46 one can obtain the electronic wave function to be

$$\phi_i(\mathbf{r}) = \sum_{\mathbf{G}} c_{i,\mathbf{k}+\mathbf{G}} e^{i(\mathbf{k}+\mathbf{G})\cdot\mathbf{r}}, \tag{2.47}$$

In principle, the expansion of the wavefunctions at each $\vec{k}$ requires infinite number of plane waves. However, the contribution of the plane waves with low kinetic energy are greater than those with high kinetic energy to this expansion. Hence, the expansion can be truncated after some predefined cut-off energy. With the defined cut-off energy the coefficient $c_{i,\mathbf{G}}$ of plane waves $e^{i\mathbf{G}\cdot\mathbf{r}}$ are set to zero when,

$$|\mathbf{k}+\mathbf{G}|^2/2 > E_{cut}. \tag{2.48}$$

When the plane waves are used in the expansion of wavefunctions, the Kohn-Sham equation turns into a matrix equation and the solution can be found by the diagonalization of the Hamiltonian matrix. The size of the matrix depends on the cut-off energy, therefore, before performing the calculations cut-off energy should be tested and an appropriate cut-off energy should be chosen.

Although, Bloch theorem cannot be applied to non-periodic systems, a non-periodic system can be thought as a periodic non-interacting system. In order to do this, a periodic super-cell is defined such that the closest atoms of neighbouring unit cells are so far that they cannot have a significant interaction. The interaction distance depends on the kind of atoms and molecules, inside the super-cell and should be tested before performing the calculations. For instance, a typical distance for carbon atoms is 10 Å which is the main subject of this thesis.

2.2.8 Pseudopotentials

Valance electrons of the atoms are responsible for many of the physical properties. The wavefunctions of the valance electrons must be orthogonal to the wavefunctions of the core electrons. Strong ionic potential in the core region, Pauli exclusion principle and the orthogonality of the wavefunctions enforce the wavefunctions of the valance electrons to oscillate rapidly in the core region. Hence, expanding the wavefunctions of core electrons in terms of a plane wave basis set requires a very large number of plane waves [79]. The plane wave basis set formalism is the simplest approach for periodic systems. Therefore, instead of leaving the plane wave formalism, the potential in the core region is approximated by a pseudopotential. The pseudopotential approximation removes the core electrons and replaces the strong ionic potential of the core region by a very soft and weak pseudopotential. This leads to smooth pseudo wavefunctions of valance electrons in the core region which can be expanded in terms of a plane wave basis set with a small number of plane waves. A norm-conserving pseudopotential has some properties. First, the pseudopotential should lead to a smooth pseudo wavefunction such that it should have no nodes. Second, the normalized pseudo wavefunction with angular momentum l should coincide with the all-electron wave function with the same angular momentum beyond a cut-off radius. Third, the number of charges should be conserved, i.e., the number of charges determined by the pseudo wavefunction should be equal to that of the all-electron wavefunction. Finally, the eigenvalues of pseudo wavefunction and the real wavefunction should be equal.

2.2.9 k-point Sampling

The periodicity determines the unit cell, and in turn the periodicity of the Brillouin zone. The volume of the unit cell is inversely proportional to the volume of the Brillouin zone, therefore, Brillouin zone for a greater unit cell is smaller. In principle, the integrations carried out in the Brillouin zone should include infinite number of k-points. However, the calculated wavefunctions are almost identical for some neighborhood of a k-point. Therefore, infinitely many k-points do not have to be taken into account, but, a k-point mesh with finite number of k-points is enough. The size of the mesh is closely related to the size of the Brillouin zone, and in turn the unit cell.

There are different kinds of methods to create special sets of k points in the Brillouin zone. One of these methods is the Monkhorst-Pack grid in which k points are distributed uniformly throughout the first Brillouin zone [127]. It requires much denser k point mesh for metallic systems with respect to insulators and semiconductors. Therefore, the density of the k-points required for the calculation is another variable to test before starting actual calculations.

2.2.10 How to Employ DFT

In the sections above, we tried to explain density functional theory by discussing many theories that leads to it. With the help of these theories and the Kohn-Sham equation, density functional theory can predict the physical properties of many-body systems by calculating the many-body wavefunction with an iterative method as in the schematic below.

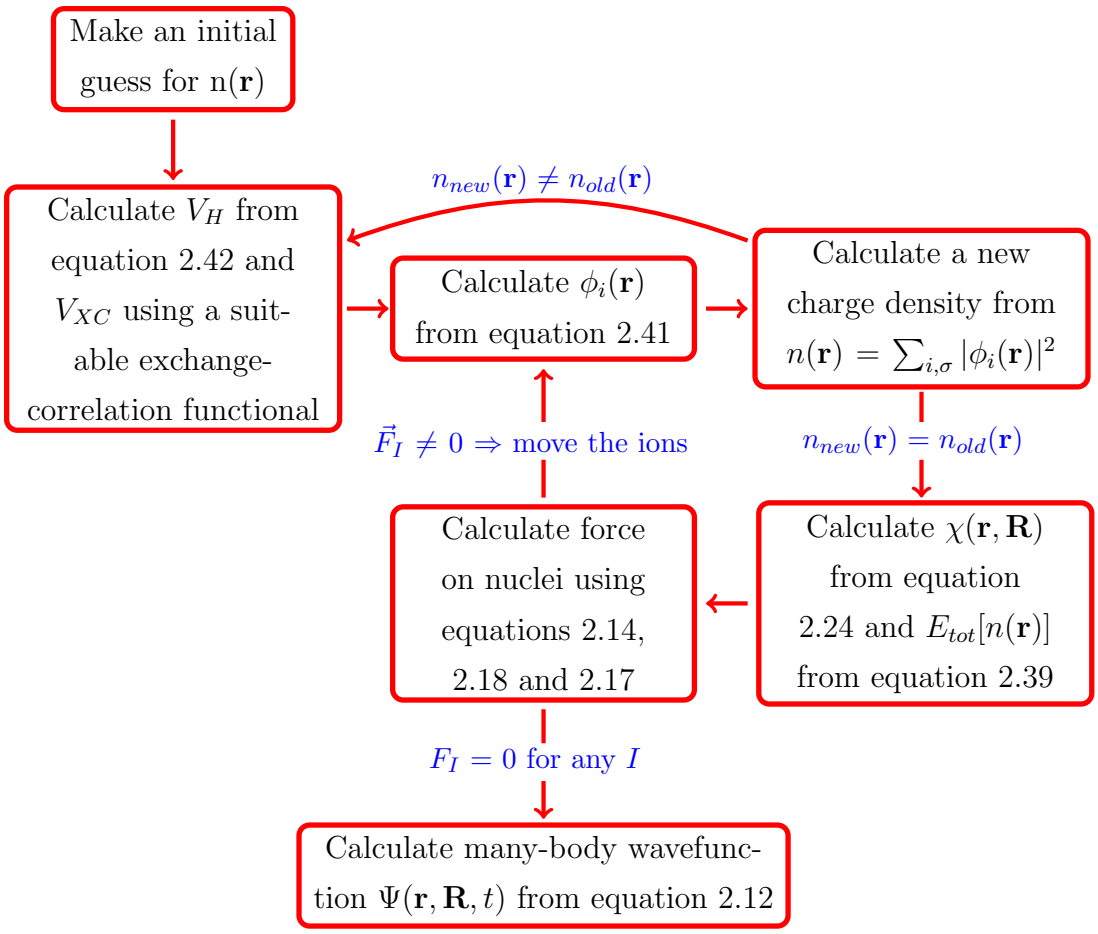
Make an initial guess for n(r)
Calculate V_H from equation 2.42 and V_{XC} using a suitable exchange-correlation functional
Calculate $\phi_i(\mathbf{r})$ from equation 2.41
Calculate a new charge density from $n(\mathbf{r}) = \sum_{i,\sigma} |\phi_i(\mathbf{r})|^2$
$n_{new}(\mathbf{r}) \neq n_{old}(\mathbf{r})$
$n_{new}(\mathbf{r}) = n_{old}(\mathbf{r})$
$\vec{F}_I \neq 0 \Rightarrow$ move the ions
Calculate $\chi(\mathbf{r}, \mathbf{R})$ from equation 2.24 and $E_{tot}[n(\mathbf{r})]$ from equation 2.39
Calculate force on nuclei using equations 2.14, 2.18 and 2.17
$F_I = 0$ for any I
Calculate many-body wavefunction $\Psi(\mathbf{r}, \mathbf{R}, t)$ from equation 2.12

Chapter 3

Graphene Nano-Ribbons

Graphene nano-ribbons (GNRs) are graphene sheets with finite size (at least in one of the dimensions). GNRs are a very active research area including energy band gap engineering [24–26], transport properties [27–30], impurities [31], effect of electric field [32–34], and edge effects [35, 36]. There are even some studies on their potential as molecular switches [37]. GNRs are very important, because, although graphene has zero band gap, GNRs can have different band gaps which depends on their shapes and sizes, so they are one of the new candidates for band gap engineering applications. Therefore, in this chapter of the thesis, we present theoretical calculations of the band structures of graphene nano-ribbons in both one (infinite in one dimension) and zero dimensions (finite in both dimensions) by using the tight binding method for several graphene nano-ribbons including armchair (AGNR), zigzag (ZGNR) and chiral (CGNR) types. These graphene nano-ribbons are observed to have zero or finite band gaps which increases with decreasing size of the ribbon, which makes them a much more suitable and strong candidate to replace silicon as a semiconductor. Also, the chirality angle has a major role in the change of the value of band gap and energy values.

3.1 Geometry of Graphene Nano-ribbons

In this section, we will describe 1D ribbons which are infinitely long in one of the dimensions, while the width is finite along the other direction and ribbons in 0D which is finite in both dimensions. In order to generate a one dimensional ribbon of width w, a 2D graphene sheet is cut in a rectangular shape such that the longer side is, in principal, infinitely long (uncut), which will be defined as L and the finite side has a length of w. If the length L of the ribbon is comparable with the width w, we have a rectangle which we can call a zero dimensional ribbon if L and w are in nano-scale.

In the cutting process of the two dimensional graphene sheet another important parameter is the direction of cutting. The shorter edge of the ribbon can be cut in armchair direction, zigzag direction or in a direction in between which is called the chiral direction. Therefore, in order to describe both the cutting direction and the length we define the chiral vector $\vec{C}$. This vector is defined in terms of the lattice vectors of graphene shown in figure 1.2a as follows,

$$\vec{C} = p_1\vec{a}_1 + q_1\vec{a}_2 \tag{3.1}$$

where p_1 and q_1 are positive integers with $p_1 \geq q_1$. This procedure of defining a graphene nano-ribbon is similar to the definition of a nanotube. The chiral vector is also a translational vector, so it defines another lattice point in two dimensional graphene as well. Now, another translational vector $\vec{T}$ can be defined which is perpendicular to the chiral vector. The chiral vector represents the width of the ribbon, whereas, $\vec{T}$ represents the length of the ribbon. Then, $\vec{C}$ and $\vec{T}$ forms a rectangular shape. Therefore, a one dimensional graphene nano-ribbon can be obtained by cutting the two dimensional graphene sheet with width $|\vec{C}|$ in the direction of chiral vector and with length L (L$\gg$w) in the direction of $\vec{T}$. In order to have a zero dimensional graphene nano-ribbon, however, L should be comparable to w.

We can define $\vec{T}$ in a similar way as we defined the chiral vector as follows;

$$\vec{T} = p_2\vec{a}_1 + q_2\vec{a}_2. \tag{3.2}$$

In equation 3.2,

$$p_2 = \frac{2q_1 + p_1}{d}, \tag{3.3}$$

$$q_2 = -\frac{2p_1 + q_1}{d} \tag{3.4}$$

where d is the greatest common devisor of $2q_1 + p_1$ and $2p_1 + q_1$. d is necessary to find the shortest possible $\vec{T}$ perpendicular to $\vec{C}$. The chirality angle can be calculated using a simple equation as follows;

$$\theta_c = \arctan \frac{p_1 - q_1}{\sqrt{3}(p_1 + q_1)}. \tag{3.5}$$

In figure 3.1, $\vec{C}$ and $\vec{T}$ are shown as well as the $p_1 = q_1$ and $q_1 = 0$ directions. If q_1 is chosen to be zero, the chiral vector will point in the direction of $q_1 = 0$ line which will lead to an edge with a zigzag shape. If p_1 is chosen to be equal to q_1, the ribbon will have an armchair shaped edge. From the figure 3.1, it is easy to figure out that if $\vec{C}$ defines a zigzag type edge, $\vec{T}$ will define an armchair one and vice versa. The naming of the ribbons include both a verbal giving the information of the long edge, and a numerical part giving the information of the short edge of the ribbon. The verbal part is related to the shape of the longer edge of the ribbon, so the shape defined by $\vec{T}$. Then, if the longer edge has a zigzag shape, these type of graphene nano-ribbons are called zigzag graphene nano-ribbons (ZGNR), whereas, if the longer edge has an armchair shape, these type of graphene nano-ribbons are called armchair graphene nano-ribbons (AGNR). If the longer edge is neither zigzag nor armchair shaped, the graphene nano-ribbon is called a chiral graphene nano-ribbon (CGNR). The numerical part of the naming of the ribbons originates from the number of atoms at the width. A zigzag graphene nano-ribbon with 10 atoms at the width will be called 10ZGNR and an armchair graphene nano-ribbon with 10 atoms at the width will be called 10AGNR. Since for a CGNR both edges are neither zigzag nor armchair shaped, we name them after p_1 and q_1 values. As an example a 2-1CGNR is displayed in figure 3.1.

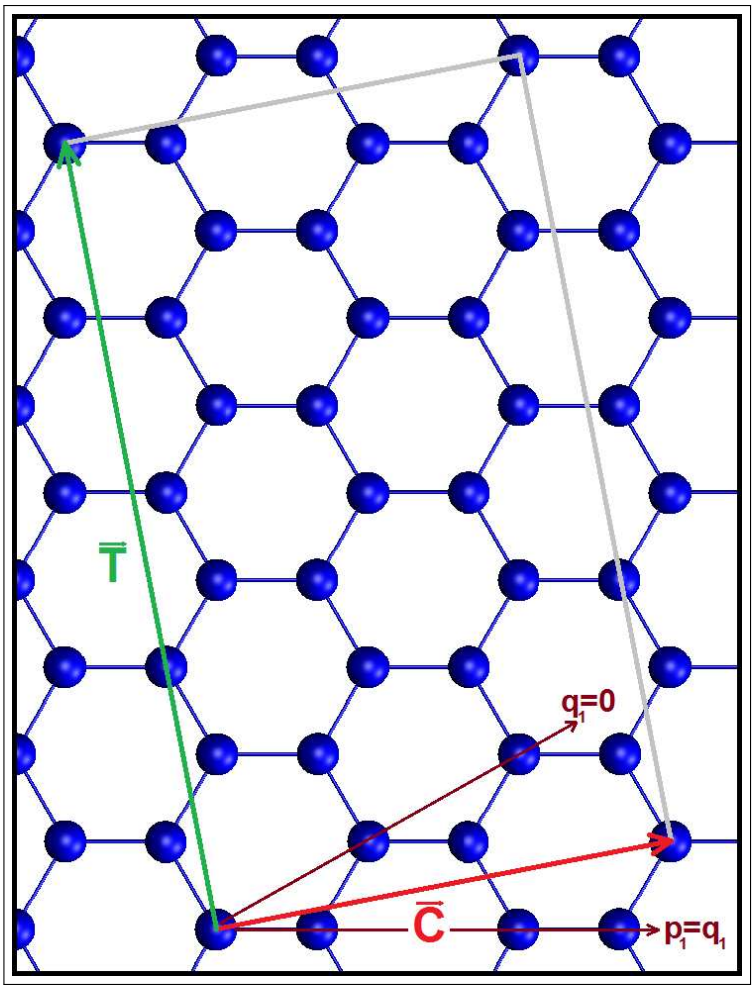

Figure 3.1: The unit cell of 2-1CGNR defined by the vectors $\vec{C} = 2\vec{a}_1 + \vec{a}_2$ and $\vec{T} = 4\vec{a}_1 - 5\vec{a}_2$. Armchair $p_1 = q_1$ and zigzag $q_1 = 0$ directions are shown as well. ($\vec{a}_1$ and $\vec{a}_2$ are defined in figure 1.2a).

3.2 Computational Method

Band structures of all graphene nano-ribbons in this chapter are calculated using the tight binding method. In order to calculate the band structure of a one dimensional graphene nano-ribbon from the tight binding method, we have to define periodic boundary conditions by defining a unit cell. Indeed, $\vec{C}$ and $\vec{T}$ are not only related to the naming of the ribbons, but also they define the unit cell. In figure 3.1, the unit cell of 2-1CGNR is the rectangle defined by $\vec{C}$ and $\vec{T}$. By repeating the system in $\hat{T}$ direction, one can have a periodic system in one dimension with width $|\vec{C}|$. Since the ribbon has a finite width, there are some carbon atoms at the edges with two neighbouring carbon atoms. Therefore, one of the sp^2 bond is not established leaving a dangling bond. Because of these unpaired electrons, the ribbon would not be stable and most probably it would twist. Since tight-binding calculation does not include a geometrical relaxation our systems would not be realistic. In order to get rid of these misleading dangling bonds, they are saturated by hydrogen atoms. We set C-H bond length to 1.09 Å [25]. We have a periodicity in only one direction leading a one dimensional reciprocal space. Therefore, in our calculations for one dimensional graphene nano-ribbons Brillouin zone is spanned by $\vec{k}$ vectors in corresponding direction.

Zero dimensional graphene nano-ribbons have finite length and width in nano-scale. Hence, they are molecules rather than periodic systems. The tight-binding calculations require a periodic system due to the Bloch theorem. Then, the super-cell approach can be used as described in the section 2.2.7. We form a large unit cell such that it contains the whole molecule and a wide vacuum region that prevents the interaction of the nearest atoms in neighbouring cells. In our calculations the vacuum region is always greater than 10 Å, which is much greater than the second nearest neighbour distance. Since we have a large unit cell, the corresponding reciprocal lattice is very small. Therefore, it is enough to use a single point, which is Γ point, in the Brillouin zone. This is also meaningful since we are dealing with molecules rather than crystals. In the calculations of zero dimensional graphene nano-ribbons, since they are finite in both dimensions, the dangling bonds of both edges are saturated by the introduction of hydrogen

atoms into the system.

In tight-binding calculations, coupling of the atomic orbitals are expressed as parameters. The parameters for carbon atoms used in our calculations are shown in table 1.2. However, since we introduced extra hydrogen atoms into the system we have to include their contributions as well. Since hydrogen atoms have a single 1s electron, we need parameters for self interaction of hydrogen atom, the interaction of s orbitals of carbon and hydrogen atoms and the interaction of p orbital of carbon with s orbital of hydrogen atom. H-H interaction, other than the self interaction is not important since we use second nearest neighbour approximation and no hydrogen has another hydrogen atom as one of these neighbours. In order to calculate these three parameters we used a fitting program for three molecules CH, CH_4 and C_2H_4, all of which include only hydrogens and carbons [80–84]. The parameters shown in table 1.2 are given as input to this fitting program so that it generated the necessary three parameters consistent with them. These new parameters are; $\epsilon_H = 6.85eV$, $H_{Hs-Cs} = 7.66eV$, $H_{Hs-Cp} = -9.92eV$ for a distance of 1.09 Å between hydrogen and carbon atoms. The calculated parameters are tested by producing the band structures of one dimensional zigzag and armchair graphene nano-ribbons and comparing them with the ones in the literature. The resulting band structures were in good agreement with the literature so that we were convinced that the parameters can safely be used in the rest of the calculations [25, 85]. As an example, the comparison for the band structure of 10ZGNR and the band gap values of AGNRs are shown in figure 3.2.

3.3 Results

In addition to the naming convention already discussed, there is one more criteria in the naming which is the dimension. If the ribbon of interest is one dimensional, we put 1D before the name such as "1D 10-ZGNR". However, if we have an armchair (zigzag) nano-ribbon in zero dimension with N atoms at the zigzag (armchair) edge, which is the shorter edge, and M atoms in the armchair (zigzag)

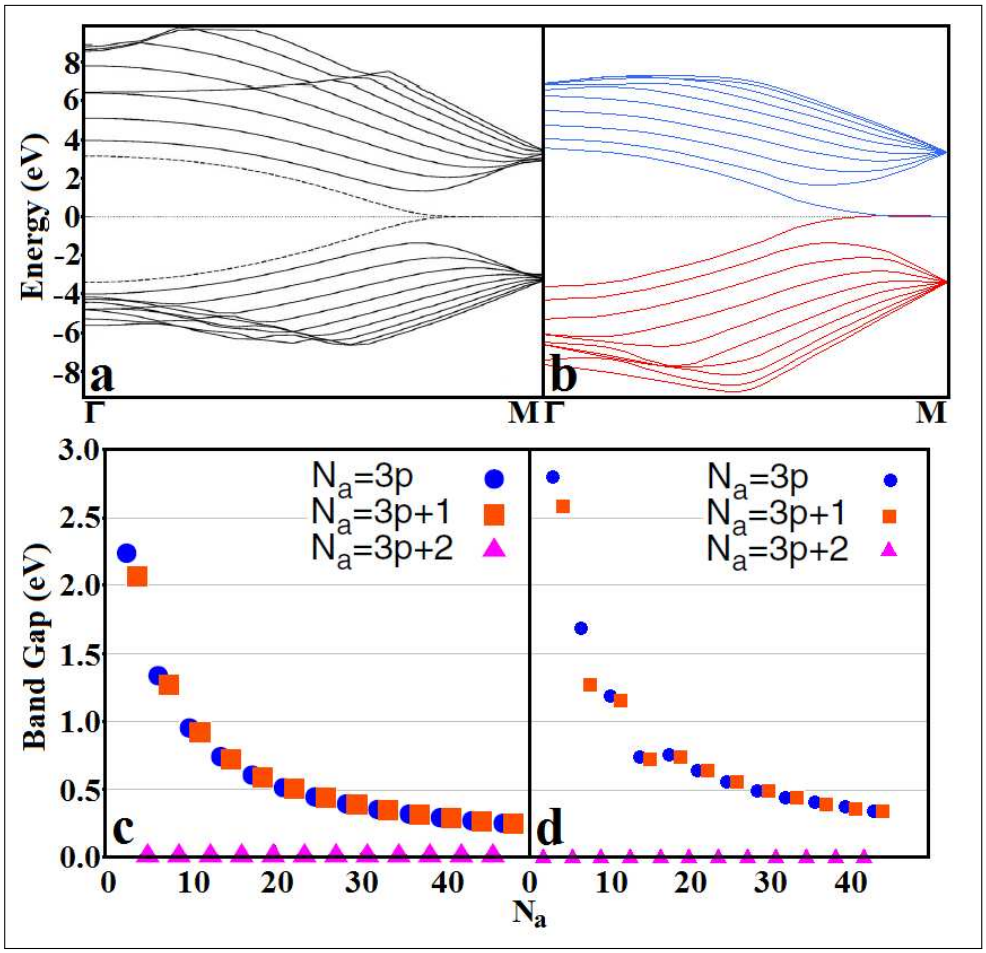

Figure 3.2: a) Band structure of 10ZGNR calculated with ab-initio method (Reproduced from L. Pisani, J.A. Chan, B. Montanari and N.M. Harrison, Phys. Rev. B 75, 64418, 2007), b) Band structure of 10ZGNR calculated with our parameters from tight binding method, c) Graph showing three distinct family behaviour of the band gap of AGNRs from tight binding calculations (Reproduced from Young-Woo Son, Marvin L. Cohen and Steven G. Louie, Phys. Rev. Lett., 97, 216803, 2006), d) Same graph generated with our parameters.

Table 3.1: Calculated band gap values for 1D zigzag graphene nano-ribbons.

Ribbon	Gap (eV)	Ribbon	Gap (eV)	Ribbon	Gap (eV)
50ZGNR	0.0	90ZGNR	0.0	130ZGNR	0.0
60ZGNR	0.0	100ZGNR	0.0	140ZGNR	0.0
70ZGNR	0.0	110ZGNR	0.0	150ZGNR	0.0
80ZGNR	0.0	120ZGNR	0.0		

edge we call it "0D MA-NZGNR" (0D MZ-NAGNR) and if we have a chiral nano-ribbon in zero dimension with integers p_1 and q_1 defining chiral vector we call the ribbon 0D p_1-q_1CGNR.

3.3.1 1D Zigzag Graphene Nano-Ribbons

The calculations are made from 3ZGNR up to 150ZGNR and the greatest ribbon has 302 atoms, 300 of which are carbon atoms, in the unit cell. Energy band calculations show that in all of the 1D zigzag graphene nano-ribbons valance and conduction bands cross each other and we have a metallic behaviour (see table 3.1). All band structures look like the one in figure 3.2b but the bands get denser as N increased.

3.3.2 1D Armchair Graphene Nano-Ribbons

The calculations are made from 2AGNR up to 151AGNR and the greatest ribbon has 306 atoms, 302 of which are carbon atoms, in the unit cell. The three distinct family behaviour is observed. As shown in figure 3.2d, if we are interested in 1D N-AGNR with N= $3p$, p being integer, we have the blue dots, with N= $p+1$, we have the red squares and with N= $p+2$ we have the pink triangles as the band gap value. We calculated the band gap values of much greater ribbons and still see the same behaviour shown in figure 3.3a. Band gap value depends on the width of the ribbon as follows;

$$E = A \times e^{-a.l} \tag{3.6}$$

Table 3.2: Calculated band gap values for 1D armchair graphene nano-ribbons.

3p	Gap (eV)	3p-1	Gap (eV)	3p+1	Gap (eV)
51AGNR	0.23	50AGNR	0.0	52AGNR	0.23
60AGNR	0.20	59AGNR	0.0	61AGNR	0.20
69AGNR	0.18	68AGNR	0.0	70AGNR	0.17
81AGNR	0.14	80AGNR	0.0	82AGNR	0.14
90AGNR	0.14	89AGNR	0.0	91AGNR	0.14
99AGNR	0.12	98AGNR	0.0	100AGNR	0.12
111AGNR	0.11	110AGNR	0.0	112AGNR	0.11
120AGNR	0.10	119AGNR	0.0	121AGNR	0.10
129AGNR	0.09	128AGNR	0.0	130AGNR	0.09
141AGNR	0.09	140AGNR	0.0	142AGNR	0.09
150AGNR	0.08	149AGNR	0.0	151AGNR	0.08

where E is the energy gap value in eV, A and a are constants with units eV and Å^{-1} and l is the length or width of the ribbon in consideration, with the unit of Å. For N= $3p$ family, $A = 1.7347$ and $a = 0.145$. For N= $3p + 1$ family, $A = 1.6004$ and $a = 0.1405$. This exponential behaviour is shown in figure 3.3b. It is worth to note that the values are very close to each other as expected. All energy gap values for N= $3p + 2$ family is zero just like graphene or 1D ZGNRs. All band gap values are shown in table 3.2.

3.3.3 0D Zigzag Graphene Nano-Ribbons

The calculations are made from 21Z4A-GNR to 41Z10A-GNR. The greatest ribbon includes 470 atoms, 410 of which are carbon atoms, to deal with. The calculated energy levels tell us that for all of the ZGNRs in 0D HOMO and LUMO levels always coincide and therefore, there is no HOMO-LUMO gap. Also, as we increase the length or the width of the ribbon the energy levels tend to get denser.

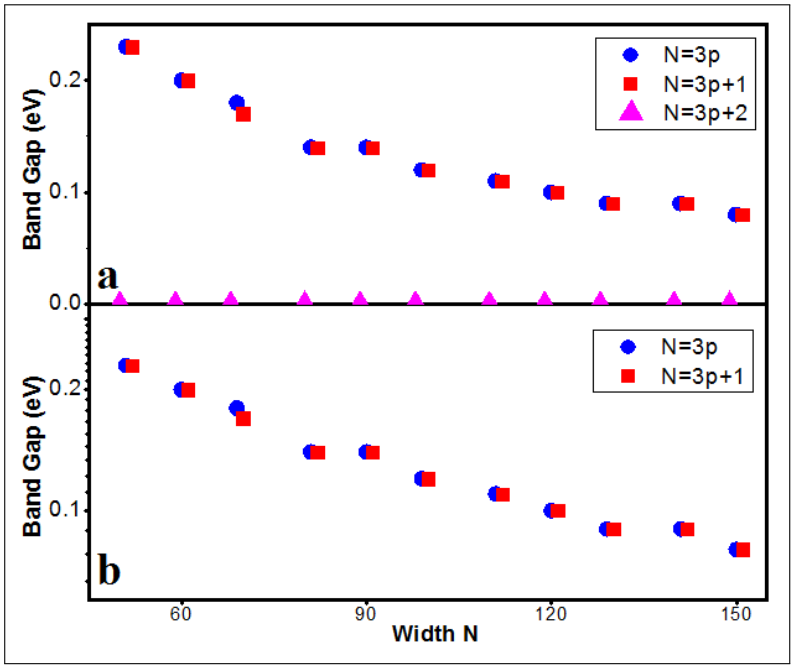

Figure 3.3: The band gap values of 1D AGNRs versus width N a) in normal scale, b) in logarithmic scale.

3.3.4 0D Armchair Graphene Nano-Ribbons

The calculations are made from 10A3Z-GNR to 30A15Z-GNR. The greatest ribbon includes 524 atoms, 450 of which are carbon atoms. For 0D AGNRs with the smallest the length, the greatest the HOMO-LUMO gap. The same thing happens for the width. The smallest width has the greatest HOMO-LUMO gap value. However, the increase in the width has a greater effect on this gap compared to the increase in the length. This can be thought as the zigzag characteristic of the width becomes quite important as we increase the width slightly and pulls the HOMO-LUMO gap down to zero. The smallest 0D AGNR (10A3Z) has a HOMO-LUMO gap of 3.4eV, and the greatest ribbon with the same width (30A3Z) has 2.9eV, whereas, the greatest ribbon with the same length (10A15Z-Notice that armchair shaped edge has a greater length then zigzag shaped edge) goes down to zero.

The HOMO-LUMO gap change of these ribbons depend on the length of the sides exponentially as in equation 3.6. For increasing length, from 10A3Z to 30A3Z we have $A = 3.3162$ and $a = 0.0144$ (figure 3.4a), from 10A5Z to 30A5Z we have $A = 1.0143$ and $a = 0.1037$ (figure 3.4a), from 10A7Z to 30A7Z we have $A = 0.3007$ and $a = 0.4941$. For increasing width, from 10A3Z to 10A15Z we have $A = 16.839$ and $a = 1.4881$ (figure 3.4b), from 12A3Z to 12A15Z we have $A = 29.695$ and $a = 1.9288$ (figure 3.4b), from 14A3Z to 14A15Z we have $A = 27.128$ and $a = 1.9804$. All HOMO-LUMO gap values are shown in table 3.3

3.3.5 1D and 0D Chiral Graphene Nano-Ribbons

In CGNRs, there is no specific shape for the edges as in ZGNRs and AGNRs. Therefore, in order to understand the band structure of 1D CGNRs, we have to consider both the width of the ribbon and how close it is to ZGNRs and AGNRs, which means we have to consider the angle of chirality. We made calculations for the band structures of 52 different 1D CGNRs. The smallest CGNR is 1D 4-1CGNR which has 34 atoms, 28 of which are carbon. The greatest one 1D

Table 3.3: Calculated HOMO-LUMO gap values for 0D armchair graphene nanoribbons.

Ribbon	Gap(eV)	Ribbon	Gap(eV)	Ribbon	Gap(eV)
10A3ZGNR	3.39	10A5ZGNR	1.01	10A7ZGNR	0.20
12A3ZGNR	3.24	12A5ZGNR	0.84	12A7ZGNR	0.12
14A3ZGNR	3.15	14A5ZGNR	0.73	14A7ZGNR	0.06
16A3ZGNR	3.08	16A5ZGNR	0.65	16A7ZGNR	0.04
18A3ZGNR	3.03	18A5ZGNR	0.57	18A7ZGNR	0.02
20A3ZGNR	2.99	20A5ZGNR	0.52	20A7ZGNR	0.02
22A3ZGNR	2.97	22A5ZGNR	0.47	22A7ZGNR	0.00
24A3ZGNR	2.93	24A5ZGNR	0.43	24A7ZGNR	0.00
26A3ZGNR	2.92	26A5ZGNR	0.40	26A7ZGNR	0.00
28A3ZGNR	2.90	28A5ZGNR	0.37	28A7ZGNR	0.00
30A3ZGNR	2.89	30A5ZGNR	0.35	30A7ZGNR	0.00
10A9ZGNR	0.04	10A11ZGNR	0.01	10A13ZGNR	0.00
12A9ZGNR	0.01	12A11ZGNR	0.00	12A13ZGNR	0.00
14A9ZGNR	0.00	14A11ZGNR	0.00	14A13ZGNR	0.00
16A9ZGNR	0.00	16A11ZGNR	0.00	16A13ZGNR	0.00
18A9ZGNR	0.00	18A11ZGNR	0.00	18A13ZGNR	0.00
20A9ZGNR	0.00	20A11ZGNR	0.00	20A13ZGNR	0.00
22A9ZGNR	0.00	22A11ZGNR	0.00	22A13ZGNR	0.00
24A9ZGNR	0.00	24A11ZGNR	0.00	24A13ZGNR	0.00
26A9ZGNR	0.00	26A11ZGNR	0.00	26A13ZGNR	0.00
28A9ZGNR	0.00	28A11ZGNR	0.00	28A13ZGNR	0.00
30A9ZGNR	0.00	30A11ZGNR	0.00	30A13ZGNR	0.00
10A15ZGNR	0.00				
12A15ZGNR	0.00				
14A15ZGNR	0.00				
16A15ZGNR	0.00				
18A15ZGNR	0.00				
20A15ZGNR	0.00				
22A15ZGNR	0.00				
24A15ZGNR	0.00				
26A15ZGNR	0.00				
28A15ZGNR	0.00				
30A15ZGNR	0.00				

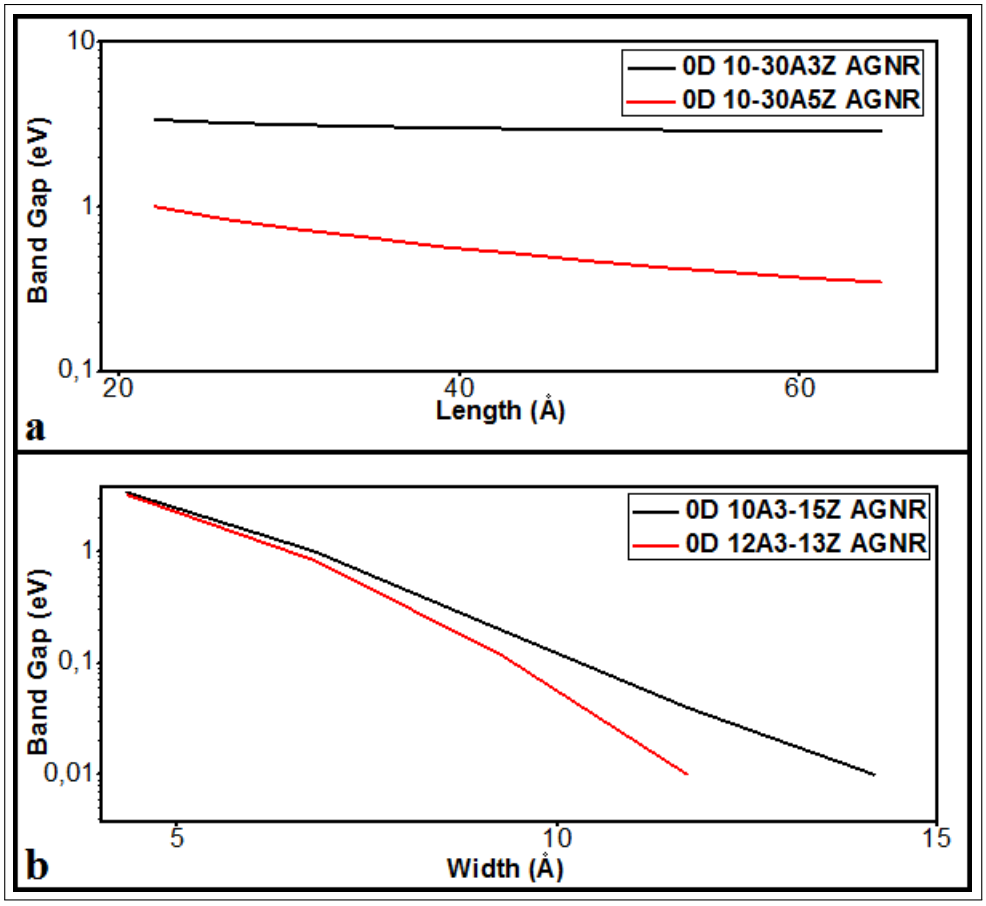

Figure 3.4: HOMO-LUMO gap of 0D AGNRs a) with widths N=3 and N=5 as a function of length, b) with length N=10 and N=12 as a function of width.

13-5CGNR however, contains 1108 atoms, 1036 of which are carbon.

When we calculated the energy band dispersions of 1D CGNRs, we observed that there are 2 families behaving differently. We can say that if $p_1 - q_1 = 3n$, p_1 and q_1 are the integers that appear in the name of the ribbon and n is an integer, the ribbon has an energy dispersion like ZGNRs, which means that the valance and conduction bands gets closer around point **M** and if $p_1 - q_1 \neq 3n$, then the energy dispersion of the ribbon is AGNR-like, which means that the valance and conduction bands get closer around the $\mathbf{\Gamma}$ point.

In order to avoid the dependence of the band gap on the chirality angle and obtain the behaviour of length dependence only, we look for 1D 4-1CGNR, 1D 8-2CGNR and 1D 12-3CGNR. We see that the band gap has an exponential dependence on the length just like in equation 3.6 with $A = 2.8235$ and $a = 1.4311$ although we cannot observe in other 1D CGNRs.

We performed calculations for the band structures of 56 0D CGNRs. The smallest CGNR is 0D 4-1CGNR which has 46 atoms, 28 of which are carbon. The greatest CGNR is 0D 13-5CGNR which has 1150 atoms, 1036 of which are carbon.

The calculations show that when we get rid of the angle dependence, equation 3.6 is valid, with $A = 1.7028$, $a = 0.3391$ for 0D 4-1CGNR, 0D 8-2CGNR, 0D 12-3CGNR and $A = 1.5278$, $a = 0.2975$ for 0D 2-1CGNR, 0D 4-2CGNR, 0D 8-4CGNR, 0D 10-5CGNR and $A = 1.761$, $a = 0.371$ for 0D 3-1CGNR, 0D 6-2CGNR, 0D 12-4CGNR. It is worth to note that the values for A and a are very close to each other in each case. In order to understand angle dependence of CGNRs we tried many functions but couldn't find a simple equation both in 1D and 0D. All HOMO-LUMO and band gap values of chiral graphene nano-ribbons are shown in table 3.4.

Table 3.4: Calculated HOMO-LUMO gap values for chiral graphene nano-ribbons for both 1D and 0D.

Ribbon	0D Gap(eV)	1D Gap(eV)	Ribbon	0D Gap(eV)	1D Gap(eV)
2-1CGNR	1.32	0.40	10-1CGNR	0.16	0.34
3-1CGNR	1.26	0.89	10-2CGNR	0.31	0.39
3-2CGNR	0.46	0.18	10-3CGNR	0.25	0.05
4-1CGNR	1.32	0.70	10-4CGNR	1.07	0.15
4-2CGNR	0.71	0.70	10-5CGNR	0.53	0.34
4-3CGNR	0.16	0.38	10-6CGNR	0.32	
5-1CGNR	0.55	0.08	10-7CGNR	0.23	0.13
5-2CGNR	0.72	0.56	11-1CGNR	0.04	0.02
5-3CGNR	0.44	0.28	11-2CGNR	0.44	0.26
6-1CGNR	0.49	0.57	11-3CGNR	0.13	0.04
6-2CGNR	0.78	0.11	11-4CGNR	0.24	0.04
6-3CGNR	0.59		11-5CGNR	0.42	0.24
6-4CGNR	0.26	0.22	11-6CGNR	0.19	0.14
7-1CGNR	0.46	0.46	12-1CGNR	0.12	0.32
7-2CGNR	0.42	0.26	12-2CGNR	0.29	0.03
7-3CGNR	0.36	0.07	12-3CGNR	0.67	0.04
7-4CGNR	0.55	0.28	12-4CGNR	0.60	0.32
8-1CGNR	0.23	0.03	12-5CGNR	0.11	0.02
8-2CGNR	0.73	0.15	13-1CGNR	0.07	0.26
8-3CGNR	0.44	0.28	13-2CGNR	0.21	0.16
8-4CGNR	0.56	0.07	13-3CGNR	0.07	0.00
8-5CGNR	0.49	0.18	13-4CGNR	0.36	0.22
9-1CGNR	0.24	0.41	13-5CGNR	0.13	0.08
9-2CGNR	0.18	0.04	14-1CGNR	0.01	0.01
9-3CGNR	0.65		14-2CGNR	0.31	0.11
9-4CGNR	0.36	0.29	14-3CGNR	0.20	0.15
9-6CGNR	0.21		14-4CGNR	0.28	0.03
15-1CGNR	0.06	0.25	15-2CGNR	0.07	0.01

Table 3.5: Calculated A and a values for specific structures.

Ribbon Type	System	A (eV)	a (Å^{-1})
1D AGNR	$N = 3p$	1.7347	0.145
1D AGNR	$N = 3p + 1$	1.6004	0.1405
1D CGNR	4-1/12-3	2.8235	1.4311
0D AGNR (w dependence)	10A3Z/10A15Z	16.839	1.4881
0D AGNR (w dependence)	12A3Z/12A15Z	29.695	1.9288
0D AGNR (w dependence)	14A3Z/14A15Z	27.128	1.9804
0D AGNR (L dependence)	10A3Z/30A3Z	3.3162	0.0144
0D AGNR (L dependence)	10A5Z/30A5Z	1.0143	0.1037
0D AGNR (L dependence)	10A7Z/30A7Z	0.3007	0.4941
0D CGNR	4-1/8-2/12-3	1.7028	0.3391
0D CGNR	2-1/4-2/6-3/8-4/10-5	1.5278	0.2975
0D CGNR	3-1/6-2/12-4	1.761	0.371

3.4 Discussions

In this chapter we performed calculations of the band structure of many one and zero dimensional GNRs using the tight binding method. All one and zero dimensional zigzag type GNRs have zero band gap values, whereas, armchair type GNRs have band gap values which can be calculated using equation 3.6 with the necessary A and a values taken from table 3.5. In one dimensional armchair GNRs the three distinct family behaviour is observed. Moreover, it is observed that one dimensional armchair and zigzag GNRs have different band structures. This difference in band structures are also observed in certain types of one dimensional chiral GNRs. Zero dimensional chiral GNRs have band gap values which obeys the equation 3.6. The A and a values to be used for certain systems are summarized in table 3.5. Although, we revealed that the band gap values has an exponentional dependence on the width and length, we could not find a simple function to fit for the angle dependence.

Chapter 4

Growth of Carbon Nanotubes: Effect of Phosphorus and Sulfur-Carbon Chemistry

With the development of microelectronics, stable, ordered nano-structures with strong bonding between the building blocks are required. CNTs in two and three dimensional networks are proposed and studied theoretically for this purpose [86]. However, this kind of a device requires CNTs grown specifically for the purpose and yet details of the growth mechanism is still a mystery. Although today we can produce many single or multi walled CNTs, we do not have control over how to produce only the kind we are interested in with the quality and quantity we want. Luckily, we do not only produce straight CNTs, but also Y and T shaped ones which are called Y and T junctions are inside the possible products. These junctions are more suitable candidates for the fabrication of electronic devices than the straight ones. There are several studies that discuss the catalytic role of sulfur in the growth mechanism of Y-junctions [49, 51, 87]. Herrera et al. claims that there is sulfur presence in the vicinity of the branches in CNTs [49]. In the same study, possible geometries for the occurrence of Y-junctions in the CNTs are discussed theoretically with the help of ab-initio density functional calculations. In-situ doping during the synthesis is also reported for phosphorus

atoms [58, 88, 89]. Although doping is achieved with the inclusion of phosphorus atoms in the growth, there is no sign of Y-junction appearance. Also, CNTs grown in a phosphorus-rich environment has a variety of differences with the CNTs grown in a sulfur-rich environment under the same conditions as reported in [58]. Sulfur and phosphorus atoms are neighbours in the periodic table and yet they have completely different effect on the growth mechanism of CNTs and Y and T junctions and kinks. CNTs growing in sulfur rich environments tend to be longer and thicker, whereas, in phosphorus rich environment, CNTs tend to grow shorter and thinner. Also, we see phosphorus-carbon clusters bound on the walls of CNTs.

The wall of a CNT with large curvature and diameter is like a hexagonal lattice in a plane. Therefore, it can be simulated using graphene instead of describing the whole CNT. In order to understand the effects of phosphorus and sulfur on the growth mechanism of CNTs, and the reason behind the differences in the structure of resulting nanotubes, we investigated the binding chemistry of these elements on graphene, the kink structure and with carbon clusters.

4.1 Computational Method

In this work, we have performed first principles plane-wave calculations [79] within density functional theory (DFT) [74,75] by the projector-augmented-wave (PAW) potentials [90, 91]. For this purpose, we have used Vienna ab-initio simulation package program (VASP) [92, 93]. The exchange-correlation potential was expressed in terms of generalized gradient approximation (GGA) (Perdew-Wang 91 type) [94]. In order to achieve desired accuracy in calculations, plane-wave cutoff energy is set to 500 eV. In order not to put a boundary condition and see the geometrical changes, we treated the system as a molecule. We have used supercells and put at least 10 Angstroms of vacuum in the calculations. By doing so we were able to minimize ion-ion interactions of the atoms of neighbouring cells. It is therefore sufficient to use the Γ point in the Brillouin zone. The partial occupancy around the Fermi level is treated by Gaussian smearing with a smearing

parameter of 0.08 eV. For all calculations energy convergence was within 10^{-5} eV accuracy. In the proceeding of this chapter, we will present the calculations in two separate parts. In the first part, we will explain the chemistry of phosphorus and sulfur atoms on graphene and the kink structure which is choosen to simulate Y-junction [52]. In the second part, we will be investigating the clusters that phosphorus and sulfur atoms make with carbon atoms. For all of the calculations of the first part, edges of finite sized structures were saturated by hydrogen atoms and then all of the atoms are relaxed to their minimum energy configurations by using conjugate gradient method. For all of the calculations of the second part, however, since there is no edge, there is no introduction of H atoms. Only carbon and phosphorus or sulfur atoms are present in these systems and they are relaxed to their minimum energy configurations by using conjugate gradient method where total energy and atomic forces are minimized.

4.1.1 Graphene and Kink Structure

We calculated the binding energies of P and S atoms on graphene, graphene with one vacancy, graphene with two vacancies and the kink structure (relaxed form of a single pentagonal defect). By doing so we can understand the binding mechanisms and chemistries of P and S atoms on the sides, on the vacancies, on the kinks and on the junctions of CNTs.

We used first principles in order to quantify the energies of various systems. The definitions are as follows, E_{grap}, $E_{grap+1vac}$, $E_{grap+2vac}$, E_{total} and E_{kink} denote the energy of graphene, graphene with one vacancy, graphene with two vacancy, phosphorus added graphene system and the kink structure, respectively. With these definitions we can use the following equation to calculate the binding energies of phosphorus atoms, which is $E_{binding}$.

$$E_{binding} = E_{total} - E_{grap} - n_P \mu_P. \tag{4.1}$$

In equation 4.1 n_P is the number of P atoms and μ_P is the chemical potential

of P atoms (For the case of Sulfur, we use n_S and μ_S instead, respectively). We relax a single P (S) atom and take the total energy of this system as the chemical potential of that atom. This equation is used for the calculation of binding energies of P atoms on graphene. The equation can be modified to be used for one vacancy on graphene case as substituting $E_{grap+1vac}$ with E_{grap} and kink like structure case as substituting E_{kink} with E_{grap}.

Similarly, formation energies are also calculated. In the formation energy we replace the last term of equation 4.1 (seperated atoms) with corresponding phosphorus or sulfur molecules such as dimer, trimer etc, i.e. replacing $n_P\mu_P$ by $E_{molecule}$. Therefore, the relation for the formation energy is;

$$E_{formation} = E_{total} - E_{grap} - E_{molecule}. \tag{4.2}$$

Similarly E_{grap} can be substituted to find the formation energy of graphene with vacancy and the kink structure. Therefore, according to our definition binding energy tells us the total required energy for phosphorus / sulfur atoms to bind the graphene or the kink structure. Formation energy, however, is the energy required to break the phosphorus (sulfur) dimer or trimer into isolated atoms and then to bind to graphene or the kink structure.

4.1.2 Clusters

The cluster calculations include the geometrical relaxation of C_xP_y (or C_xS_y) systems. For these systems x and y can range from 1 to 4, where $2 \leq x + y \leq 5$. All these systems are relaxed to their minimum energy configurations. For each x and y values we may have infinitely many initial configurations. Therefore, we tried many (but finite) initial configurations in order to see the behaviour of the atoms during geometric relaxation and calculated the minimum energy of final configurations.

4.2 Adsorption of P or S on Graphene and Kink Structure

In this part, we are going to present the results of binding chemistry of phosphorus and sulfur atoms on graphene and the kink defect structure. For this purpose, we performed calculations for more than 100 initial configurations for both phosphorus and sulfur atom adsorption. As a result, we saw that the relaxation process almost always yielded the same configuration, i.e. phosphorus and sulfur showed similar behaviour when incorporated in these structures.

4.2.1 Phosphorus

Phosphorus atoms are initially placed close to both the graphene surface and the kink structure. First, we put a single phosphorus (P_1) atom into various possible positions close enough to make contact with the graphene so as to understand the location and strength of binding. In order to do that P_1 atom is placed on top of a carbon atom of the graphene or on top of the bond between carbon atoms of graphene or on top of the center of the hexagon, 2 Å away from the surface. Relaxation from all configurations ended up such that P_1 sits on top of the bond bridging two carbon atoms, which are pulled a little out of the plane of graphene (figure 4.1a). The bond distance between the carbon and phosphorus atoms was 1.93 Å. Following the understanding of the behaviour of single phosphorus atom towards graphene, we introduced another one into the system. The second P atom is placed both close to and far away from the P_1 approaching from different angles. Starting from many different initial configurations, we ended up with 3 different final configurations. The first configuration is one in which the P atoms make a dimer with 1.91 Å in between P atoms and move away from the graphene (figure 4.1b). In the second configuration P_2 pushes P_1 from the top of the bond to the top of C atom and it goes to the top of the nearest C atom so that making a bridge which has a length of 2.07 Å (figure 4.1c). The third final configuration is that P_2 is far away enough from P_1 and they don't interact. Therefore, both of them sits on top of a C-C bond away from each other (figure 4.1d). The

distance between P atoms is more than 4.5 Å in this final configuration. In other initial configurations where P_2-P_1 distance is less than 4.5 Å phosphorus atoms were able to attract each other resulting in two other final configurations. After that, we introduced the third P atom (P_3) into the system for all combinations of possible configurations. We found 3 different final configurations again. First final configuration is that P atoms make a triangle and moves away from the graphene surface (figure 4.1e). Second final configuration is that they cannot make a triangle but stay as a line again moving away from the graphene surface (figure 4.1f). For the third final configuration we can say that if they are far away enough, they don't interact and all of them sits on top of C-C bond more than 4.5 Å away from each other. Next, we investigated P adsorption on graphene with a single vacancy by placing P atoms on various possible positions. In all configurations, we ended up with the P atom trying to substitute the missing C atom, however, since it has a bigger radius it doesn't fit to that space. Therefore, it moves a little out of the plane (less than 1.5 Å) taking the closer C atoms with itself (figure 4.2a). After that, we introduced a second vacancy neighbour to the first one. This time since there is more than enough space P atom goes in the middle of the bond between missing C atoms staying in plane of graphene (figure 4.2b). With two vacancies and two P atoms, however, the first final configuration is one where the two P atoms are located on the opposite sides of the graphene plane and make a bond with a length of 2.13 Å in between through the hole of vacancies (figure 4.2c). They are also bounded to the C atoms closer to them. The second final configuration is that they stay in the same side of graphene making a bridge configuration (figure 4.2d). P-P distance is 2.16 Å for this case.

Next, we started the calculations for the kink defect structure. First, we placed one P atom (P_1) in several initial positions both around the pentagon and away from the pentagon of the kink structure. We observed two final configurations. P atom either goes on top of the C-C bonds which are the members of the pentagon (figure 4.3a), or it goes on top of the bonds between the one C atom being a member of the pentagon and the the other C atom being being the neighbour of the pentagon (figure 4.3b). In both cases the C-P distance is about 1.88 Å. If we introduce a second P atom (P_2) into the system we have three different final

configurations. The first one is that they make a dimer with 1.9 Å bond length and go away (figure 4.3c). The second one is that P_1 stays in its position and P_2 binds it with a distance 1.94 Å without binding to any C atom making a needle out of kink structure (figure 4.3d). Third final configuration is that they make a bridge between two nearest members of the pentagon (figure 4.3e). Then, P-P distance is 2.06 Å and C-P distance is 1.93 Å. When we introduce the third P atom (P_1) the final configurations increase. We have a triangle which is bounded to the kink (figure 4.3f) as well as a triangle without binding (triangle-C distance 2.08 Å) (figure 4.3g). We have a line without any connection to kink (figure 4.3h). We have a dimer and a P atom bounded to the kink (figure 4.3i). Also, we have the bridge on pentagon and a separated P atom with no connection to the bridge (figure 4.3j).

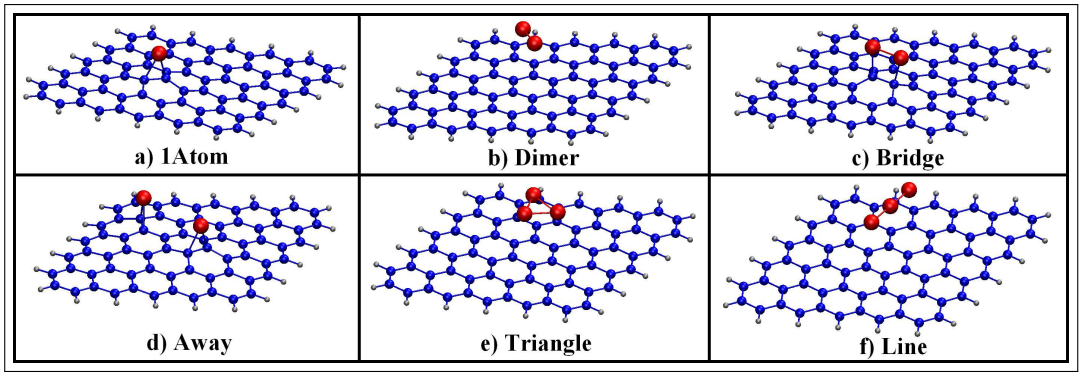

Figure 4.1: Various optimized final configurations of P an S atoms on graphene.

4.2.2 Sulfur

When we place one S atom into various positions over the graphene surface it goes on top of the bond between C atoms just like P does (figure 4.1a). With the introduction of the second S atom we ended up with 2 different configurations. They either didn't interact (figure 4.1d), or they made a dimer with a bond length of 1.93 Å (figure 4.1b). However, the distance that they don't interact decreased to less than 3.5 Å and also they didn't make a bridge if we compare with P case. With the introduction of the third S atom, we had either a triangle away

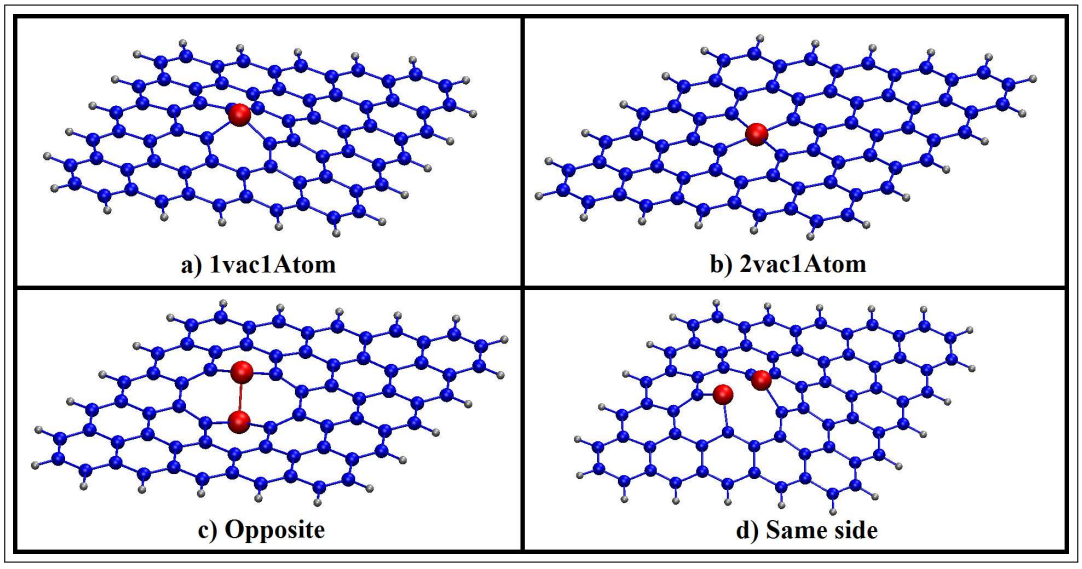

Figure 4.2: Various optimized final configurations of P and S atoms on graphene with vacancies.

from graphene surface (figure 4.1e) or a broken line (like the geometry of water molecule) again away from the surface. The difference between S and P cases here is that we have a straight line for P. We have the same final configurations for 1 vacancy+1S and 1 vacancy+1P cases (figure 4.2a). S, just like P is again out of the plane less than 1.5 Å away. If we introduce a second vacancy, S atom goes in the middle of the bond of C atoms missing just like P atom (figure 4.2b). For 2 vacancy+2S case again the final configurations are the same with the case of P (figure 4.2c-d). However, when S atoms are on the opposite sides, the distance between them is 2.91 Å.

The kink structure with one S atom has the same final configurations as the case for P (figure 4.3a). It either binds to a bond on pentagon with C-S distance of 1.87 Å or out of the pentagon with C-S distance of 1.83 Å (figure 4.3a-b). When we introduce the second S atom, however, we don't see three different configurations as it was the case for P. This time we have two final configurations first of which is a dimer with S-S distance of 1.95 Å but it cannot escape from the kink structure. There is a 2.1 Å f distance between closest C and S atoms. Second final configuration is a bridge with an S-S distance of 2.06 Å and S-C distance

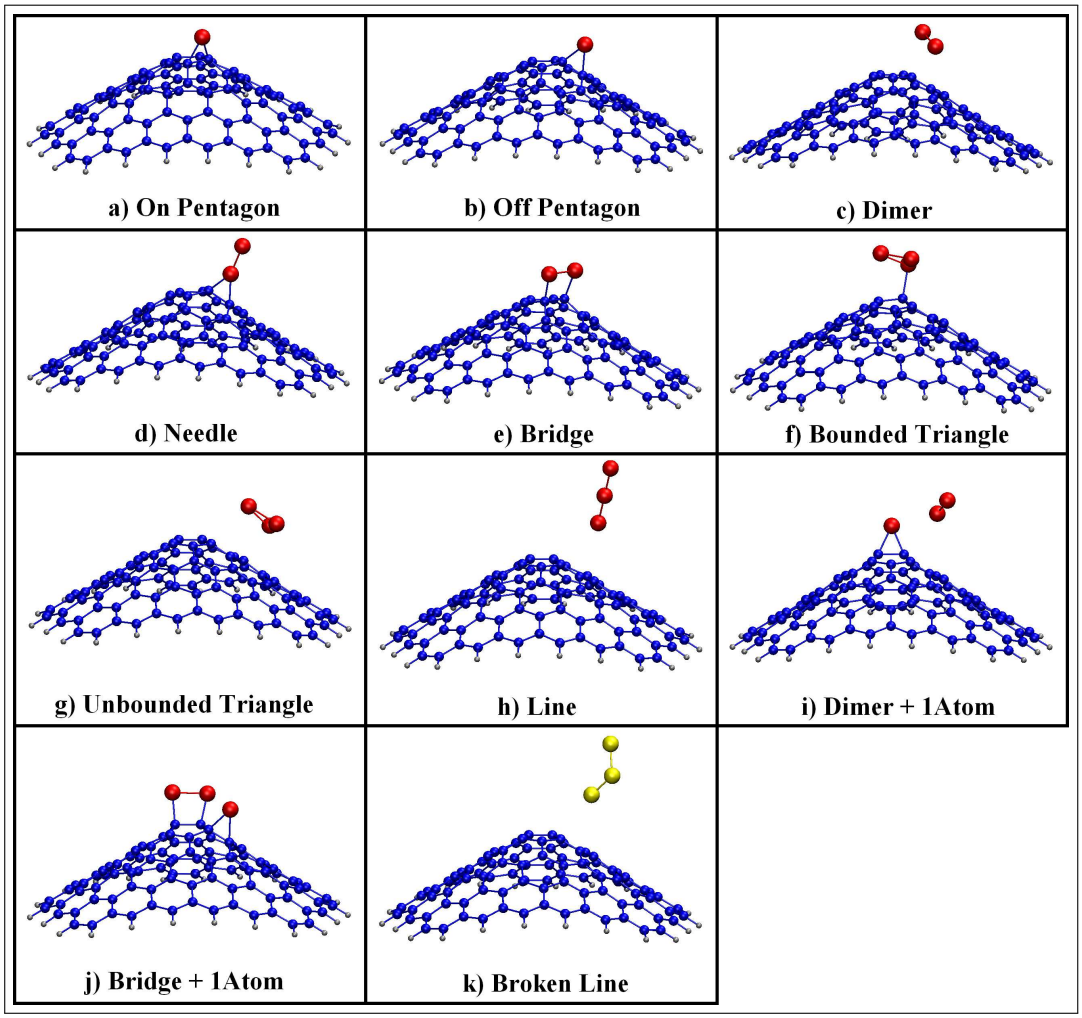

Figure 4.3: Various optimized final configurations of P an S atoms on the kink structure.

Table 4.1: Binding and formation energies for all observed final structures.

System	Phosphorus		Sulfur	
	$E_{Binding}$(eV)	$E_{Formation}$(eV)	$E_{Binding}$(eV)	$E_{Formation}$(eV)
Graphene				
1Atom	-1.66	-1.66	-1.69	-1.69
Dimer	-9.02	-0.06	-6.49	-0.22
Bridge	-6.58	2.37	-	-
Away	-3.77	5.18	-3.43	2.84
Triangle	-13.52	-0.12	-10.53	0.30
Line	-12.61	0.80	-10.41	0.42
Graphene with vacancy				
1vac1Atom	-9.86	-9.86	-8.08	-8.08
2vac1Atom	-7.50	-7.50	-5.25	-5.25
Opposite	-12.42	-3.46	-9.71	-3.44
Same side	-12.57	-3.61	-7.62	-1.35
Kink structure				
On Pentagon	-2.68	-2.68	-2.78	-2.78
Off Pentagon	-2.72	-2.72	-2.75	-2.75
Dimer	-9.05	-0.09	-	-
Needle	-6.80	2.15	-6.89	-0.62
Bridge	-8.44	0.51	-6.40	-0.12
Bounded Triangle	-14.44	-1.05	-	-
Unbounded Triangle	-13.63	-0.23	-10.53	0.30
Line	-12.59	0.81	-11.08	-0.24
Dimer+1Atom	-11.90	1.50	-	-
Bridge+1Atom	-11.67	1.73	-9.54	1.30

of 1.93 Å (figure 4.3e). In this case we do not observe the needle configuration. When we introduce the third S atom we have three final configurations. The first one is that S atoms make a triangle and move away (figure 4.3g), in the second configuration two S atoms make a bridge and the third atom is separated (figure 4.3j). In the third configuration, S atoms make a broken line away from the kink structure (figure 4.3k).

4.2.3 Discussion

In table 4.1 binding energies of all observed final structures are shown. When we look at phosphorus on graphene case, it is favourable for two phosphorus

atoms to make dimer with respect to making a bridge with a difference of 3 eV in binding energies. In sulfur case, it doesn't make a bridge at all. Also, for three phosphorus on graphene, making triangle is energetically favorable by about 0.9 eV when it is compared to making a line. Again, it favors making a triangle in sulfur case but this time binding energy difference is about 0.1 eV. In all cases with graphene, both S and P tend to find other S and P atoms, and get away from the graphene structure. If we have vacancy sites however, incoming atoms try to heal those vacancies. For two atoms added to two vacancy case, phosphorus slightly tends to stay on the same side making a bridge, whereas, sulfur chooses to stay on the opposite sides of graphene. This choice decreases the energy of the system around 2.1 eV more.

Formation energies support the results of binding energies. Formation energy of dimer is slightly negative, which means that dimer in physical interaction distance is preferable among all other configurations for both phosphorus and sulfur. For the trimer case however, phosphorus has a negative, sulfur has a positive value of formation energy. This indicates that it is still favorable for phosphorus atoms tend to stay in physical interaction regime with the carbon network, whereas, it is favourable for sulfur atoms to aggregate and escape from the graphene structure. For all the vacancy cases, since healing a vacancy decreases the energy a lot, all formation energies are negative.

For the kink structure the incoming atom tends to stay close to the pentagon. When the second phosphorus is introduced, it takes the first phosphorus atom out of the carbon network making a dimer, which is 0.6 eV more favorable than the making a bridge. However, for sulfur, making a dimer is still favorable over making a bridge but this dimer cannot escape from the kink structure. With the introduction of the third phosphorus we can see that the most favorable case is bound triangle. However, we didn't observe such a final configuration in the sulfur case. In sulfur, instead of making a triangle, making a broken line is energetically more favorable. It seems that usual tendency is to escape from the kink structure for both sulfur and phosphorus.

Formation energies also support these results. We have a negative energy

value for the dimer in physisorption regime for phosphorus, whereas, dimer in chemisorption regime is favorable for sulfur. A triangle in chemical interaction regime is favorable by 1.05 eV with respect to isolated triangle for the phosphorus case, whereas, a broken line in physical interaction regime is favorable for sulfur.

4.3 Carbonaceous Clusters Including P or S Atoms

We start with 39 initial configurations for both C_xP_y and C_xS_y structures. In all of them, the two closest atoms have a distance of 2 Å between them. We started with C_1P_1 (C_1S_1) and relaxed the system to see the binding energy of carbon atom to phosphorus and sulfur. Then, we increased the number of atoms and finally ended up with 20 minimum energy final configurations out of 78 initial configurations. But what is interesting was some final configurations as a local minimum in energy.

4.3.1 Phosphorus

There are 39 initial configurations for the C_xP_y system which are the same for the system with sulfur instead of phosphorus. These 39 initial configurations consist of one C_1P_1, three C_1P_2, three C_2P_1, three C_1P_3, four C_2P_2, three C_3P_1, seven C_1P_4, five C_2P_3, five C_3P_2, five C_4P_1 systems with different geometries. We assign each of them some appropriate name after their geometries. For example, in figure 4.5b1, C_1P_2 line-edge is shown and named like this because the atoms are lined up and the single carbon atom is in the edge of this line. Closest atoms at figure 4.5 always have 2 Å of distance.

Starting with these 39 initial geometries we ended up with 10 minimum energy final configurations for each combination of x and y values. These minimum energy configurations are shown in figure 4.6. What we are trying to do is to

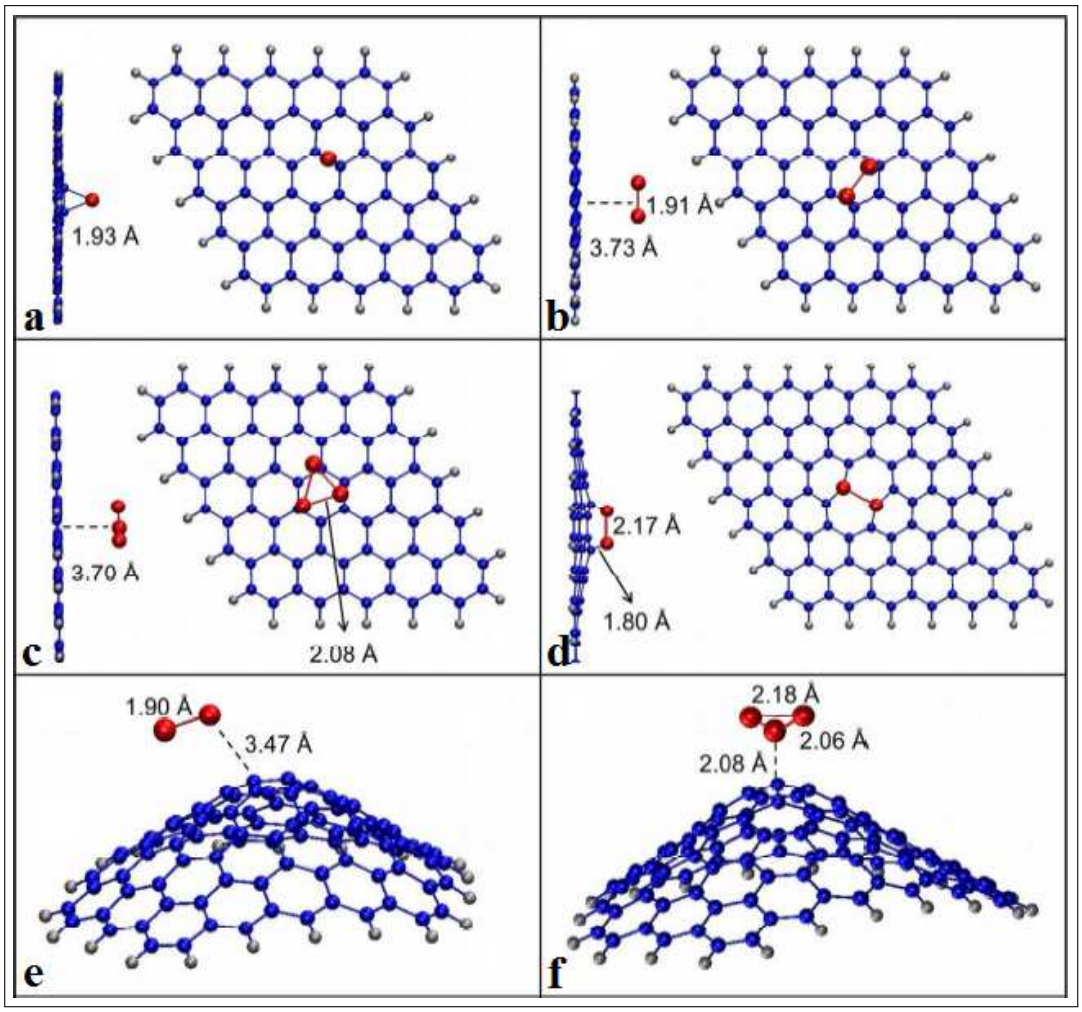

Figure 4.4: Optimized structures of phosphorus adsorption over various graphene structures with minimum formation energy: a) Single phosphorus atom in bridge position, b) two and c) three phosphorus atoms over the graphene layer, d) two phosphorus atoms on the double vacancy of graphene layer, e) two and f) three phosphorus atoms over the kink structure. (Small blue, large red and gray dots represent carbon, phosphorus and hydrogen atoms respectively.)

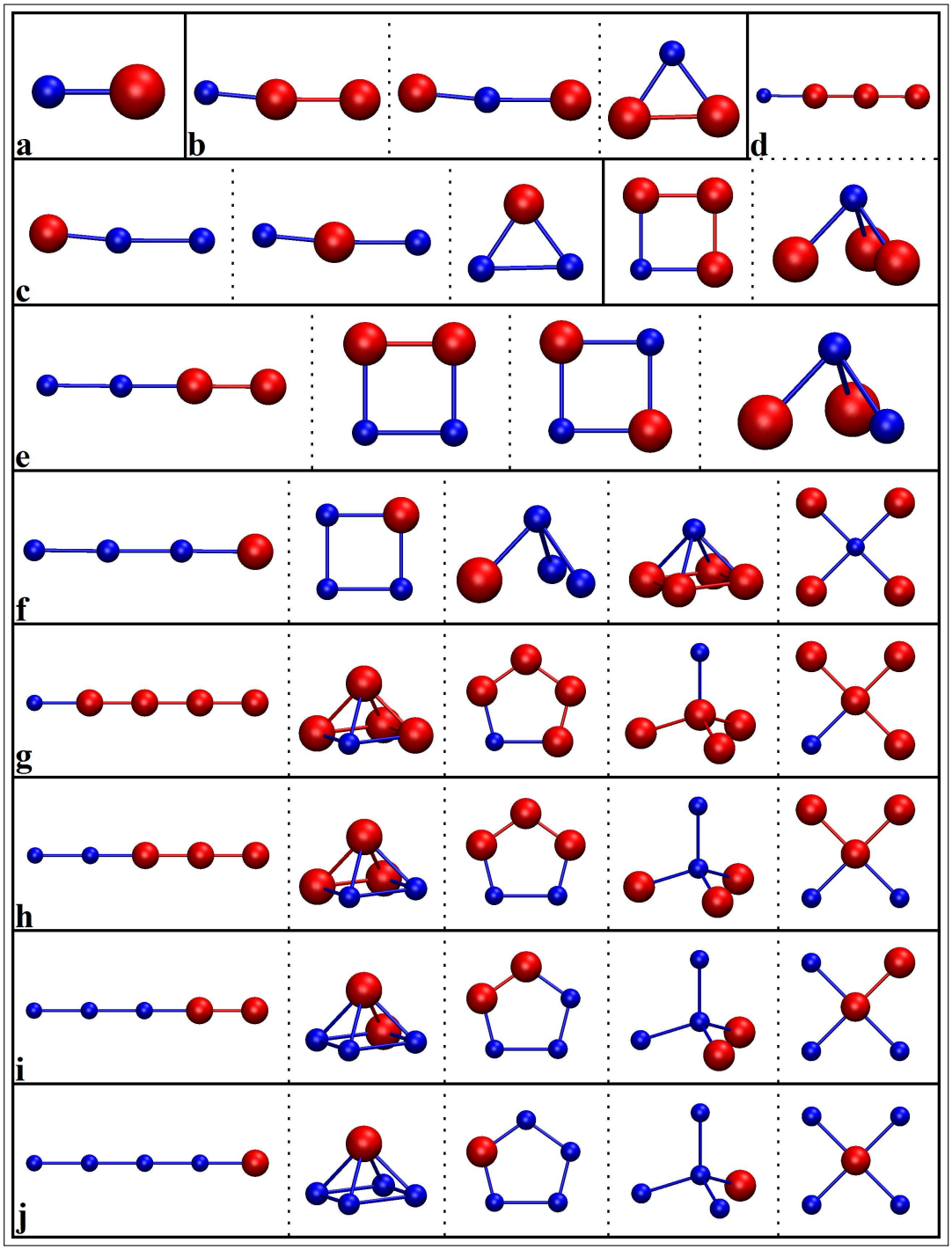

Figure 4.5: Initial geometries for the investigation of the C_xP_y cluster structures (Since initial geometries are the same for P and S cases, only C_xP_y are shown.). a)C_1P_1, b) C_1P_2, c) C_2P_1, d) C_1P_3, e) C_2P_2, f) C_3P_1, g) C_1P_4, h) C_2P_3, i) C_3P_2, j) C_4P_1 (Small blue and large red spheres represent carbon and phosphorus atoms respectively).

compare the final geometries and the minimum energy values of the systems with phosphorus and sulfur atoms so that we will be able to see if there is a difference in their behaviour and use this difference to explain the situation in CNTs.

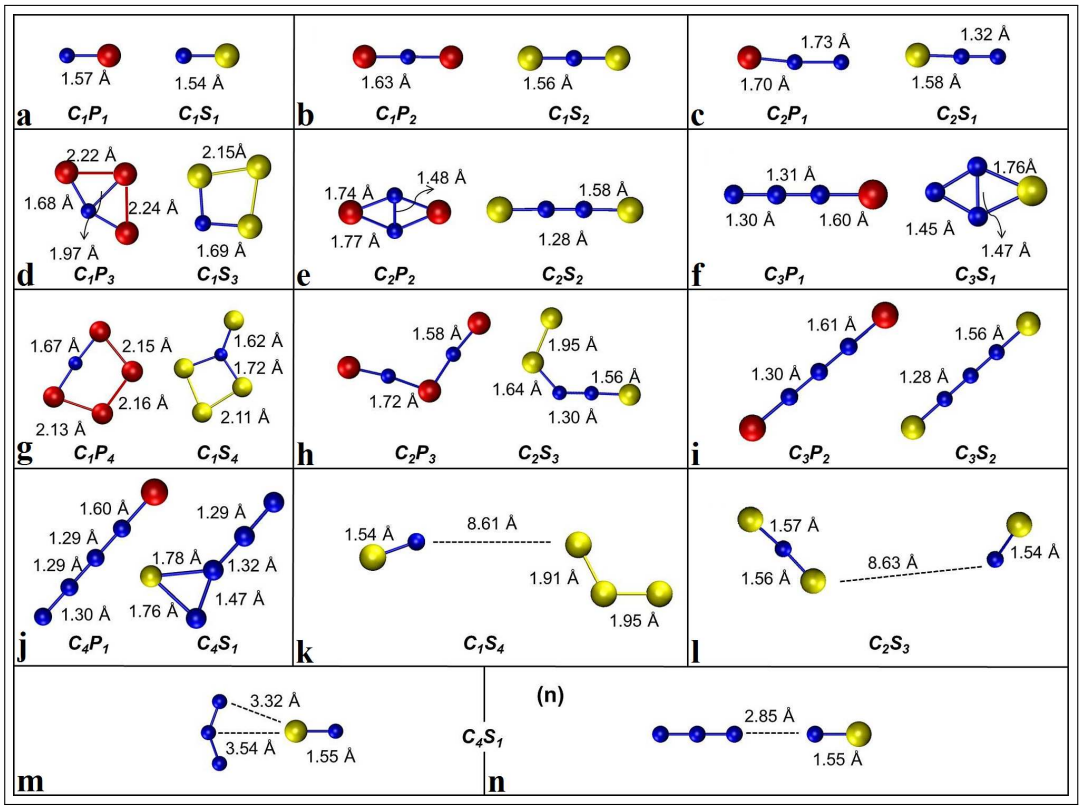

Figure 4.6: Final optimized geometries of C_xP_y-C_xS_y clusters with minimum energy cases and some local minima. Minimum energy cases are for a)C_1P_1-C_1S_1, b) C_1P_2-C_1S_2, c) C_2P_1-C_2S_1, d) C_1P_3-C_1S_3, e) C_2P_2-C_2S_2, f) C_3P_1-C_3S_1, g) C_1P_4-C_1S_4, h) C_2P_3-C_2S_3, i) C_3P_2-C_3S_2, j) C_4P_1-C_4S_1; and for local minimum of cases k) C_1S_4, l) C_2S_3, m) C_4S_1, n) another C_4S_1 (Small blue, large red and large yellow spheres represent carbon, phosphorus and sulfur atoms respectively.).

4.3.2 Sulfur

The initial configurations are exactly same as the ones shown in figure 4.5, where we replace phosphorus atoms with sulfur atoms. However, minimum energy final configurations may end up totally different for some cases as shown in figure 4.6.

4.3.3 Discussion

By examining the figure 4.6, we come up with some results. C-P bond distance is slightly greater than C-S bond distance, however, its a negligible difference. C-C distance is much shorter than these two, which is around 1.3 Å. If we look at the bond distances of C-C atoms in 4.6c, we can see that P atom wants to make a bond with C atom more than other C atom, however, S atom has a closer behaviour as the other C atom. In all minimum energy final geometries atoms are positioned in the same plane, lets say planar). At least we can say this for the systems with five atoms. Also, they all make a cluster with bond distances around 1.5-2 Å. As looking at the minimum energy configurations there seems to be no sharp difference between C_xP_y and C_xS_y systems. However, in 4.6k-l-m-n some final configurations of local minima in energy are shown. We found many final configurations like these where we lose cluster for C_xS_y systems, whereas all C_xP_y systems always ended up as a cluster. At these pictures, S atom takes a C atom out of the system, i.e from the chemical interaction regime to physical interaction regime. We believe that this tendency of S atoms can explain the different effects of P and S atoms on the growth mechanism of CNTs. As the CNTs grow, P atoms tie themselves to the CNT surface by making a cluster. These clusters are observed experimentally as well [58]. S atoms can make a cluster, however, when they find another S atom nearby, they may escape the system as we see at 4.6k. Therefore, it is less likely for S atom to tie itself with the CNTs. Since P atoms tend to make a cluster, they decrease the number of available C atoms for CNTs to grow. Therefore, CNTs cannot grow long, or thick as they do in S rich environment.

The total energies for the configurations shown in figure 4.6 are shown in table 4.2. Second and third lines show the C-C, P-P and S-S binding energies. C-C and P-P binding energies are very close, whereas, S-S binding energy is low respectively. Although C-P binding energy is lower than C-S binding energy, C_xP_y systems have less total energy with respect to C_xS_y systems. This is because of the strong P-P interaction. The most striking result that can be taken out from this table is that minimum energy configurations and local minima configurations

Table 4.2: Total energies for the systems shown in figure 4.6.

	System with P	Total Energy (eV)	System with S	Total Energy (eV)
	C_2	-9.00		
	P_2	-9.02	S_2	-6.48
a	C_1P_1	-8.60	C_1S_1	-10.20
b	C_1P_2	-15.49	C_1S_2	-16.56
c	C_2P_1	-16.86	C_2S_1	16.12
d	C_1P_3	-20.75	C_1S_3	-18.14
e	C_2P_2	-23.34	C_2S_2	-20.52
f	C_3P_1	-25.33	C_3S_1	-23.67
g	C_1P_4	-27.01	C_1S_4	-23.74
k			C_1S_4	-21.37
h	C_2P_3	-28.92	C_2S_3	-27.01
l			C_2S_3	-26.75
i	C_3P_2	-32.27	C_3S_2	-32.85
j	C_4P_1	-33.65	C_4S_1	-31.30
m			C_4S_1	-29.22
n			C_4S_1	-28.95

do not have a significant difference in total energy. This tells us how strongly S atoms tend to escape the system of clusters and destroy it, whereas, we do not observe such behaviour for C_xP_y clusters.

4.4 Conclusion

In this chapter, since the CNTs growing in phosphorus rich environment are very different in many properties than the ones growing in sulfur rich environment, we investigated the effect of phosphorus and sulfur atoms on the growth mechanism of CNTs. In order to do that we investigated the chemistry and interaction of P and S atoms with graphene layer, which can simulate a CNT with large curvature, a kink structure, which can simulate the Y-junction in a CNT, as well as C-P and C-S cluster structures. In conclusion, we can say that we did not observe much difference in chemistry while P and S atoms interact with graphene or kink structure. For both of the structures phosphorus/sulfur atoms tend to get away as soon as they find another phosphorus/sulfur atom if there is no

vacancy. Therefore, phosphorus/sulfur is not likely to interact with a complete CNT structure. However, we observed that C atoms tends to make clusters with P atoms in every case, whereas, C-S clusters are destroyed in some cases and S atoms tend to escape the cluster as they find another S atom. Therefore, we can say that while P atoms are collecting and binding the available C atoms around and so hindering the nanotube growth, S atoms do not and CNTs grow much longer and thicker in S rich environment with respect to P rich environment. In addition to these, when a phosphorus atom enters the CNT wall during the growth, it is very probable to attract other carbon atoms to make clusters on the nanotube with respect to sulfur case. Therefore, nanotubes will be better graphitized in sulfur rich environment with respect to phosphorus rich environment. Indeed this is so as we showed in [58].

Chapter 5

Lithium Intercalation For Battery Applications

Batteries are demanded to be as light and thin as possible. However, the most desirable property for a battery is its ability for high capacity and rechargeablity. Rechargeable lithium ion batteries are one of the most promising energy storage devices for electric vehicles and hybrid electric vehicles which have a growing market because of global warming and other environmental effects [95–99]. Li ion batteries possess high energy density, high power density, low cost, superior safety, and stable cycling lifespan. This motivates researchers to find a suitable material used as an electrode for lithium ion batteries. Polyanionic compounds such as Li_2FeSiO_4/C nanocomposite [100–102], $LiMn_2O_4$ [103], transition metal oxide compounds such as $CoO/CoFe_2O_4$ nanocomposites [57,104,105] are possible electrodes. Also, graphitic carbon and related carbonaceous materials are prime candidates for electrode applications [56] in Li-ion batteries having reversible capacity of a couple of hundreds Ah/kg (a thousand at most) [55]. Although, metal oxide compounds have higher capacity carbon based materials have the advantage of structural stability [57]. CNTs have improved capacity in comparison to graphite [106–108]. Further improvement can be achieved by doping, functionalizing and defect engineering [109, 110].

There are numerous theoretical and experimental work on the electronic and structural changes with the introduction of lithium atoms into graphitic system [111–119] (graphite, CNTs, etc.) as well as charge transfer from lithium to carbon atoms [111, 112, 120–125]. However, an agreement on how much charge is transferred from lithium to carbon atoms cannot be reached yet. According to some researchers, there is full charge transfer from Li to the graphitic system [111], whereas some others report that there is only partial charge transfer [112, 115, 120, 121].

In this work, we tried to understand the chemistry of lithium on bilayer graphene system so that we could mimic a double-walled CNT. We calculated binding energies of various configurations and found out the most stable configuration and understand the effects of defects. Also, we resolved the controversy in the literature about the charge transfer from lithium to the carbon network.

5.1 Computational Method

In this work, we have performed first-principles plane-wave calculations [79] based on density functional theory [74, 75] by using the projector-augmented-wave (PAW) potentials [90, 91]. For this purpose, we have used Vienna ab-initio simulation package program (VASP) [92, 93]. The exchange-correlation potential was expressed in terms of both local density approximation (LDA) [126] and generalized gradient approximation (GGA) (Perdew-Wang 91 type) [94]. In order to achieve desired accuracy in the calculations, plane-wave cutoff energy is set to 500 eV. Calculations are performed using a unit cell that includes 6x6 bilayer graphene and a Li atom, 145 atoms in total. The system is periodic in the xy-plane whereas, we have vacuum about 15 Å thick in perpendicular direction. We have chosen the 6x6 bilayer graphene unit cell in order to avoid the interactions of Li atoms of neighbouring cells. Since 6x6 graphene has lattice vectors longer than 14 Å it is safe to say that Li atoms of neighouring cells do not interact. Although unit cell is large, which results in the Brillouin zone being small, we still used a large grid in reciprocal lattice setting k-point 7x7x1 as

a Monkhorst-Pack [127, 128] mesh. The partial occupancy around Fermi level is treated by Gaussian smearing with a smearing parameter of 0.08 eV. For all calculations energy convergence was within 10^{-5} eV accuracy. In all calculations atoms are relaxed to their minimum energy configurations by using conjugate gradient method where total energy and atomic forces are minimized.

We are going to use the words "AA and AB stacking" in the following context. AA stacking means that all atoms in one layer of bilayer graphene are exactly over the atoms of the atoms of the previous layer, whereas, AB stacking means that A type atoms of one layer is exactly on the top of A type atoms of the other layer but B type atoms are on top of (or underneath) the center of the hexagon of the other layer. In our calculations, both AA and AB stacking of bilayer graphene are used with layer separation of 3.35 Å.

We tried several initial configurations depending on where the Li atom is positioned with respect to the graphene layers. Also, we have checked the case where we have one or two vacancies in bilayer graphene. We put Li atom on top of A atom, on top of B atom, on top of the C-C bond and on top of the center of a hexagon 2 Å above the top graphene layer in different configurations. Then, we put the Li below A atom, B atom, C-C bond and the center of a hexagon of the top layer with the same distance of 2 Å so that Li atom is in between the layers. As another initial configuration, we substituted a C atom of top layer with Li atom. Finally, we removed another C atom neighbouring to the missing one to create a double vacancy saturated with a Li atom. In the end, we had 8 initial geometrical configurations in AA stacking as shown in figure 5.1. Since AB stacking breaks the symmetry between A and B type atoms, we had more initial configurations, 12 in total as shown 5.2.

Since Van-der Waals interaction is not described well in DFT, when one relaxes bilayer graphene, layer seperation will increase up to 3.8 Å for LDA and more than 4.0 Å for GGA. In order to avoid this, and keep the distance around 3.35 Å as it initially was, we froze 22 atoms in perpendicular direction to the plane 11 in upper and 11 in lower plane (shown as green atoms in figures 5.1 - 5.4). This is another reason to choose a large (6x6) graphitic system. With the carbon atoms

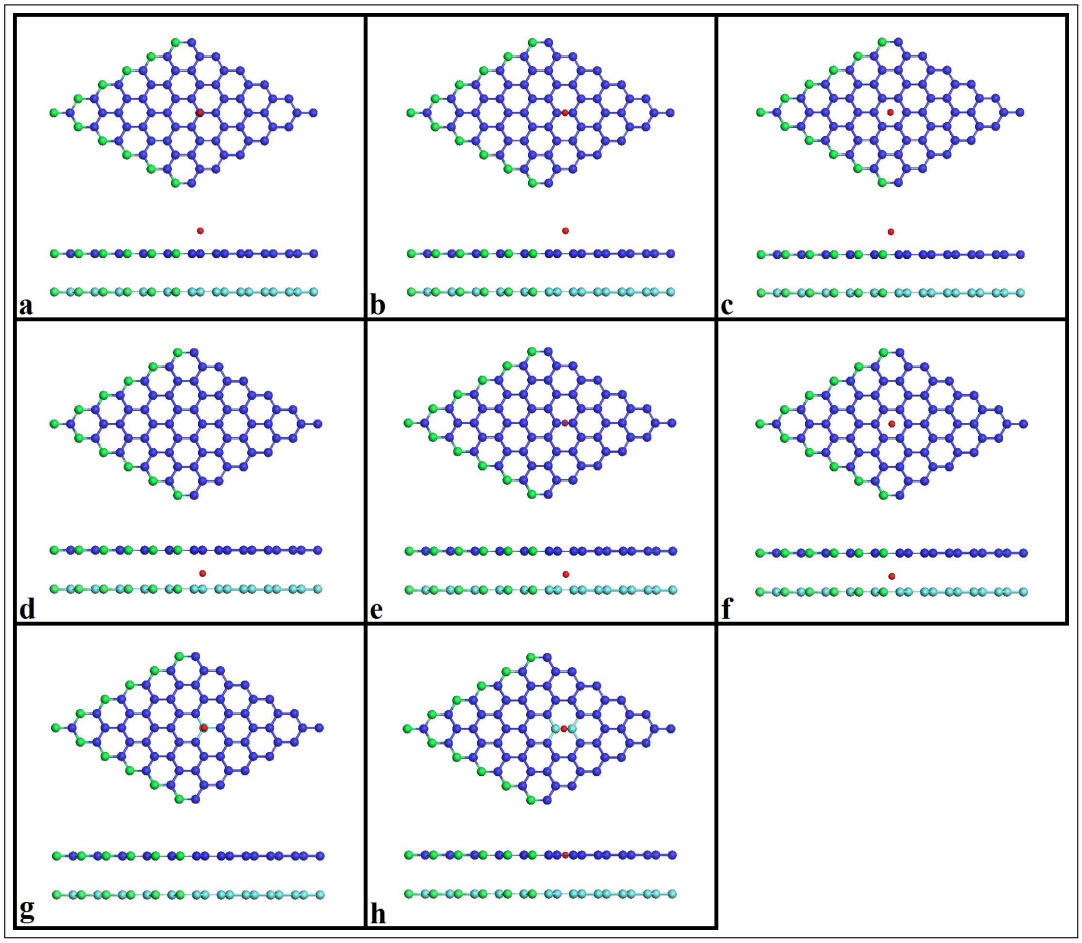

Figure 5.1: Top and side view of 8 different initial configurations for Li introduced AA stacking bilayer graphene. Li atom is, above the top layer a) on top of a C atom, b) on top of the C-C bond, c) on top of the center of a hexagon; in between the layers d) on top of a C atom, e) on top of a C-C bond, f) on top of the center of a hexagon; substituted with g) a C atom of the top layer; placed h) in the middle of the bond of two missing C atoms of the top layer (Blue, light blue, green and red spheres represent C atoms of the top layer, C atoms of the bottom layer, frozen C atoms and Li atom respectively). In "mid" cases Li has a 2 Å of distance with the bottom layer.

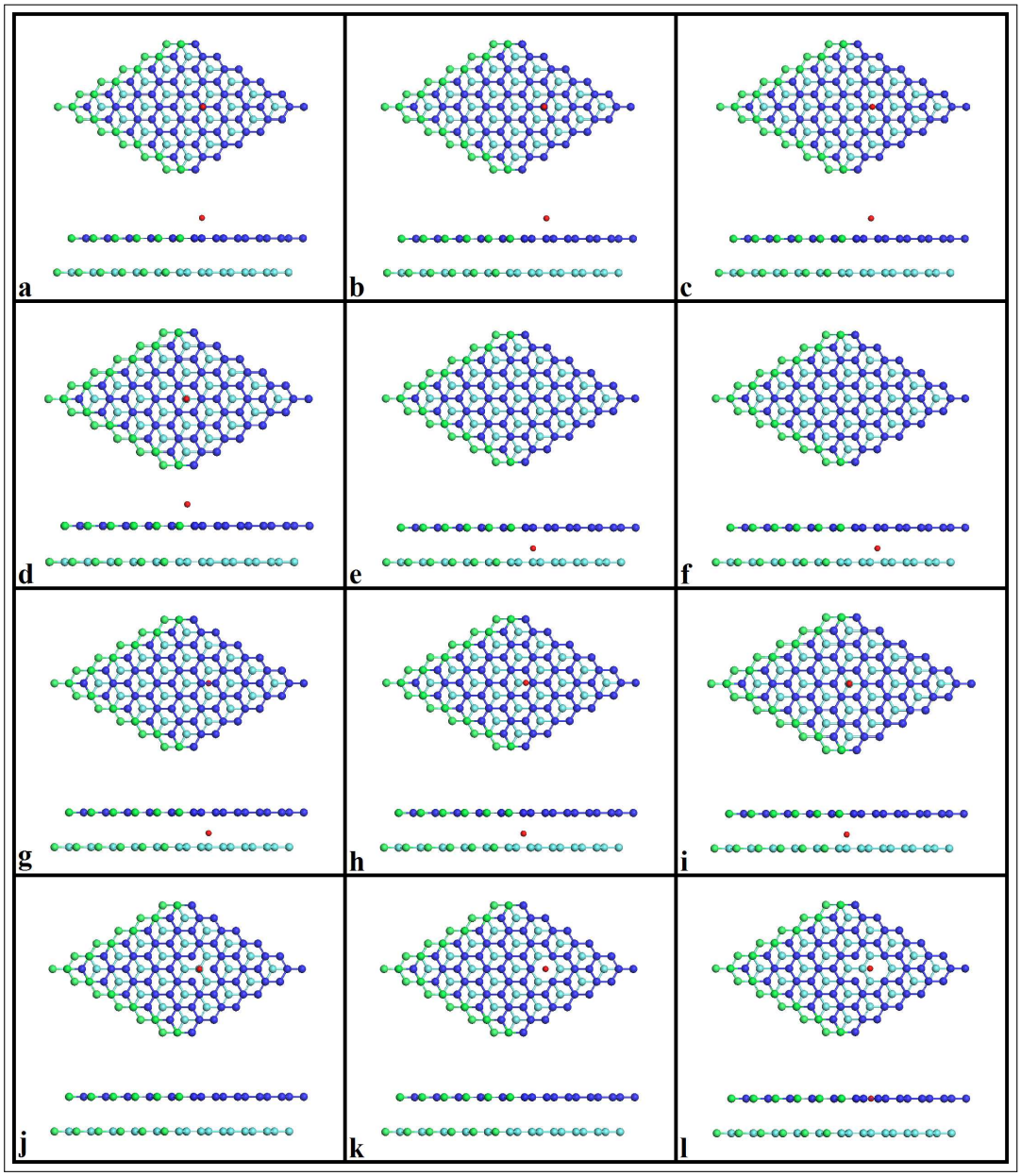

Figure 5.2: Top and side view of 12 different initial configurations for Li introduced AB stacking bilayer graphene. Li atom is, above the top layer a) on top of an A type C atom, b) on top of a B type C atom, c) on top of the C-C bond, d) on top of the center of a hexagon; in between the layers e) on top of an A type C atom, f) under a B type C atom, g) under the C-C bond of the top layer, h) above the C-C bond of the bottom layer, i) on top of a B type atom of the bottom layer; substituted with, j) an A type C atom of the top layer, k) a B type C atom of the top layer; placed l) in the middle of the bond of two missing C atoms of the top layer. (Colour convention is the same as in figure 5.1). In "mid" cases Li has a 2 Å of distance with the bottom layer.

in the vicinity of lithium being free, we relaxed the systems in all calculations. Then, binding energy of Li atoms to the graphite system in final configurations are calculated to find out the energetically preferable position for Li atom. Binding energies are calculated as follows;

$$E_{binding} = E_{total} - E_{grap} - n_{Li}\mu_{Li}. \tag{5.1}$$

In equation 5.1 $E_{binding}$ is the binding energy of Li to the graphitic system, E_{total} is the total energy of the system, E_{grap} is the energy of graphitic system (relaxed bilayer graphene (AA or AB stacking), relaxed bilayer graphene with one or two vacancies), n_{Li} is the number of Li atoms, which is "1" in all of our calculations and μ_{Li} is the chemical potential of Li atom.

We have also calculated the charge transfer between Li and the graphitic system. There are many controversial reports about this issue in the literature both in theoretical [111, 112, 120, 121] and experimental studies [122–125]. Some of these studies claim that there is full charge transfer from Li to the graphitic system, whereas some others report that there is only partial charge transfer. We tried to resolve this problem by obtaining charge densities and then calculating the charge transfer by using Bader [129, 130] analysis. The first problem we encountered is that there seemed to be significant charge transfer among carbon atoms of the graphitic system. Even the furthest carbon to lithium atom had a charge transfer of about 0.3 e^-. Now that we understood that there is a problem, we tried to get rid of the effect of the lithium atom and did the same analysis on 6x6 bilayer graphene. Again, we had charge transferred from some carbon atoms to the neighbouring ones even with AA stacking although we should have the same number of charges for each atom. This situation does not make sense, since all carbon atoms should have 4 valance e^-'s, which indicates a deeper problem. Therefore, we checked the charges of carbon atoms for 1x1 graphene and encountered with similar numbers. Our first approach to solve the problem was to increase the number of grid points (FFT mesh) that are calculated to describe the charge density. To do so, we set the tag "PREC = High" in the INCAR file. INCAR file is the file of VASP that the determiness "what and

how to do" containing large number of parameters. "PREC = High" tag is the highest defined setting for the number of grid points that can be set without entering this number of points particularly. With this tag, the number of grid points reach more than twice of the first trial. However, it was still not enough. Then, we particularly set the number of grid points by setting "NGXF, NGYF and NGZF" values in the INCAR file. These tags represent the number of FFT mesh in a certain direction, as an example, "NGFX=1000" means to take 1000 equally spaced points in x-direction so as to describe charge density. We found out that in order to obtain 4 e^-'s in each carbon atoms of graphene, we had to use an FFT mesh two orders of magnitude denser than the default settings. Increasing the grid size this much costs a lot of time and memory, which makes the calculations to be a lot harder and expensive. Then, we carried over our discussion for the system with Li atom where we encountered a second problem. This time, charges of carbon atoms were good enough within the numerical error, whereas, according to Bader analysis there were no lithium atom in the system at all, i.e. analysis finds zero volume for lithium. Lithium atom tends to give its valance charge and local minimum of the charge density, which Bader analysis look for, passes over the atom since the charge density is calculated only for the valance electrons in default settings. We thought that if we introduce the core electrons in to the system, we could overcome this problem. In order to do this, we set the tag "LAECHG = .TRUE.", which tells VASP to include core charges while writing the output file of charge density. Then, the core electrons of both C and Li atoms are introduced to the system. The introduction of core electrons somehow effected the carbon atoms in such a way that electron tranfer between them occured again. Same problem is obtained for pure graphene as well. We tried a lot of new approaches to obtain a better descripton of charges. One of those approaches was to map the calculated wave functions onto atomic orbitals. In the calculations we use plane-waves as the basis set, therefore, we had to set "LORBIT = 10" in the INCAR file in order to see the wavefunctions mapped onto the atomic orbitals. After trying many different approaches and failing in the description, we ended up with that the first approach was the best of all. We returned to the first approach i.e. using core electrons in the calculation

with a great number of grid points. This time, however, we changed the pseudo-potential file, i.e. "POTCAR" for Li atom, to include 1s electrons as well as valance electron. We removed "LAECHG = .TRUE." flag so that we had 4 e^-'s for each carbon atoms which are valance e^-'s, whereas, we had 3 e^-'s for the lithium atoms two of which are core e^-'s and one of which is the valance one. With this last setting, we were able to solve the problem for charge density and charge transfer.

5.2 Results

We had 8 different initial configurations for AA and 12 different configurations for AB stacking. After the relaxation we had 8 final configurations for both stackings. Actually, for AA stacking Li atom stayed almost in the same position as it initially was as shown in figure 5.3. However, for AB stacking, we had 8 final configurations out of 12 initial configurations as shown in figure 5.4. Li atom almost stayed in the original position as it was, in the initial configurations where Li atom is above the upper layer. 5 different initial configurations where Li atom is in between the layers, converged into a single final configuration. For this final configuration Li atom is between a B type atom and a hexagon. GGA and LDA results do not differ significantly for all of the final configurations. The first thing to check is the distance of Li atom to the nearest C atom for all cases. Also binding energies are calculated and tabulated.

5.2.1 Adsorption

For AA stacking we have 3 adsorption sites. "Outer A atom" (figure 5.3a) is the one where the lithium atom is on top of the carbon atom, "Outer bridge" (figure 5.3b) is the one where the lithium atom is above the bond between two carbon atoms, and, "Outer hollow" (figure 5.3c) is the one where the lithium atom is above the center of hexagon. For AB stacking we have "Outer B atom" (figure 5.4b) where the lithium atom is on top of B type atom, as well as the other

Table 5.1: GGA and LDA results of Li-C bond distances (d), binding energies (E_b) and transferred charge (e^-) from Li to C network for AA stacking

Adsorption Geometry for AA stacking	GGA			LDA		
	d (Å)	E_b (eV)	e^-	d (Å)	E_b (eV)	e^-
Outer A atom	2.06	-1.70	0.91	1.99	-1.93	0.90
Outer bridge	2.14	-1.72	0.91	2.08	-1.96	0.90
Outer hollow	2.27	-2.02	0.90	2.21	-2.29	0.88
Mid A atom	2.14	-2.49	0.88	2.01	-2.60	0.84
Mid bridge	2.21	-2.50	0.88	2.09	-2.63	0.84
Mid hollow	2.39	-2.75	0.88	2.30	-3.01	0.85
A substitution	2.19	-2.77	0.88	2.04	-3.54	0.84
Double C vacancy	2.36	-2.80	0.89	2.27	-3.29	0.86

Table 5.2: GGA and LDA results of Li-C bond distances (d), binding energy (E_b) and transferred charge (e^-) from Li to C network for AB stacking

Adsorption Geometry for AB stacking	GGA			LDA		
	d (Å)	E_b (eV)	e^-	d (Å)	E_b (eV)	e^-
Outer A atom	2.05	-1.50	0.91	2.01	-1.43	0.90
Outer B atom	2.06	-1.50	0.91	1.99	-1.43	0.90
Outer bridge	2.14	-1.52	0.91	2.09	-1.45	0.90
Outer hollow	2.25	-1.82	0.90	2.21	-1.76	0.88
Mid hollow	2.14	-2.42	0.87	2.03	-2.22	0.83
A substitution	2.04	-3.01	0.87	2.01	-3.28	0.86
B substitution	2.08	-3.02	0.85	2.03	-3.42	0.82
Double C vacancy	2.33	-2.82	0.89	2.20	-3.30	0.86

3 configurations. Minimum lithium-carbon distances are shown in the first and fourth column of table 5.1 for AA stacking and table 5.2 for AB stacking. From these tables it can be depicted that bond distances with GGA potential is slightly greater than the ones with LDA. However, it is not a significant difference. The average bond distance for the adsorption sites is 2.14 Å for GGA potential and 2.08 Å for LDA. In order to understand which configuration is the most stable one, we check for the energetics. In the second and fifth column of table 5.1 and 5.2 binding energies of Li atom to the graphitic system are shown. For both AA and AB stacking adsorption geometries energetically the most stable one is the "Outer hollow" case (both GGA and LDA) having around 0.3 eV more binding energy with respect to the other configurations.

5.2.2 Intercalation

For AA stacking we have 3 possible sites for the intercalation case. "Mid A atom" (figure 5.3d) is the one where the lithium atom is in between carbon atoms of two layers, "Mid bridge" (figure 5.3e) is the one where the lithium atom is in between C-C bonds of two layers, and, "Mid hollow" (figure 5.3f) is the one where the lithium atom is in between the center of the hexagons of two layers. For AB stacking however, we have only one final configuration "Mid hollow" (figure 5.3e) where the lithium atom sits in between a B type atom of one layer and the center of the hexagon of the second layer. Average bond distance for these configurations is 2.22 Å for GGA and 2.11 Å for LDA potentials. From the final configurations and the bond distances, it seems that the lithium atom tends to keep its distance with the carbon atoms around 2.15 Å and sets its position accordingly. Hollow site is again energetically the most favourable position amongst all. This tells us that the lithium atom wants as much neighbour as possible. Same argument is also strengtened by having AA stacking "Mid hollow" case as the most stable arrangement of all adsorption and intercalation final configurations. In this case the lithium atom has 12 neighbours around almost in same distance, whereas, in AB stacking "Mid hollow" case (0.3 eV less binding energy respectively) it has 7 neighbours and in AA or AB "Outer hollow" case, which is the third stable configuration, (0.8 eV less binding energy respectively) it has 6 neighbours.

5.2.3 Substitutional

We tried lithium substitution geometries by taking one or two carbon atoms away from the graphitic system and then substituting it with lithium. For AA stacking we have 2 possible final configurations. "A substitution" (figure 5.3g) is the one where one carbon atom is replaced with a lithium atom, "Double C vacancy" (figure 5.3h) is the one where two neighbouring carbon atoms are taken out of the system and one lithium atom is put instead. Since in AB case we have A type and B type carbon atoms we have 3 different cases. "A substitution" (figure 5.4f) is the one where A type carbon atom, "B substitution" (figure 5.4g)

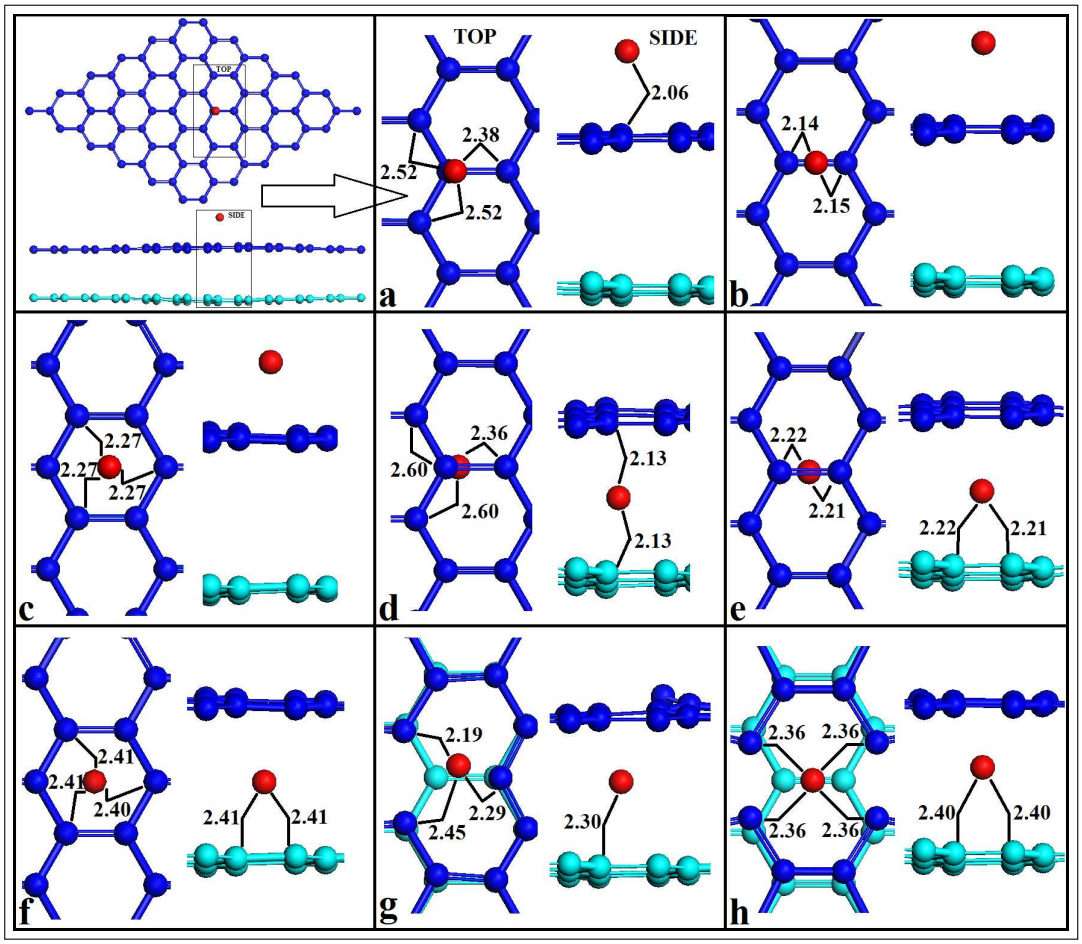

Figure 5.3: Top and side view of 8 different optimized final configurations for Li introduced AA stacking bilayer graphene. These final configurations represent a) Outer A atom, b) Outer bridge, c) Outer hollow, d) Mid A atom, e) Mid bridge, f) Mid hollow, g) A substitution, h) Double C vacancy, which are presented in table 5.1 (Blue, light blue, and red spheres represent C atoms of the top layer, C atoms of the bottom layer and Li atom respectively).

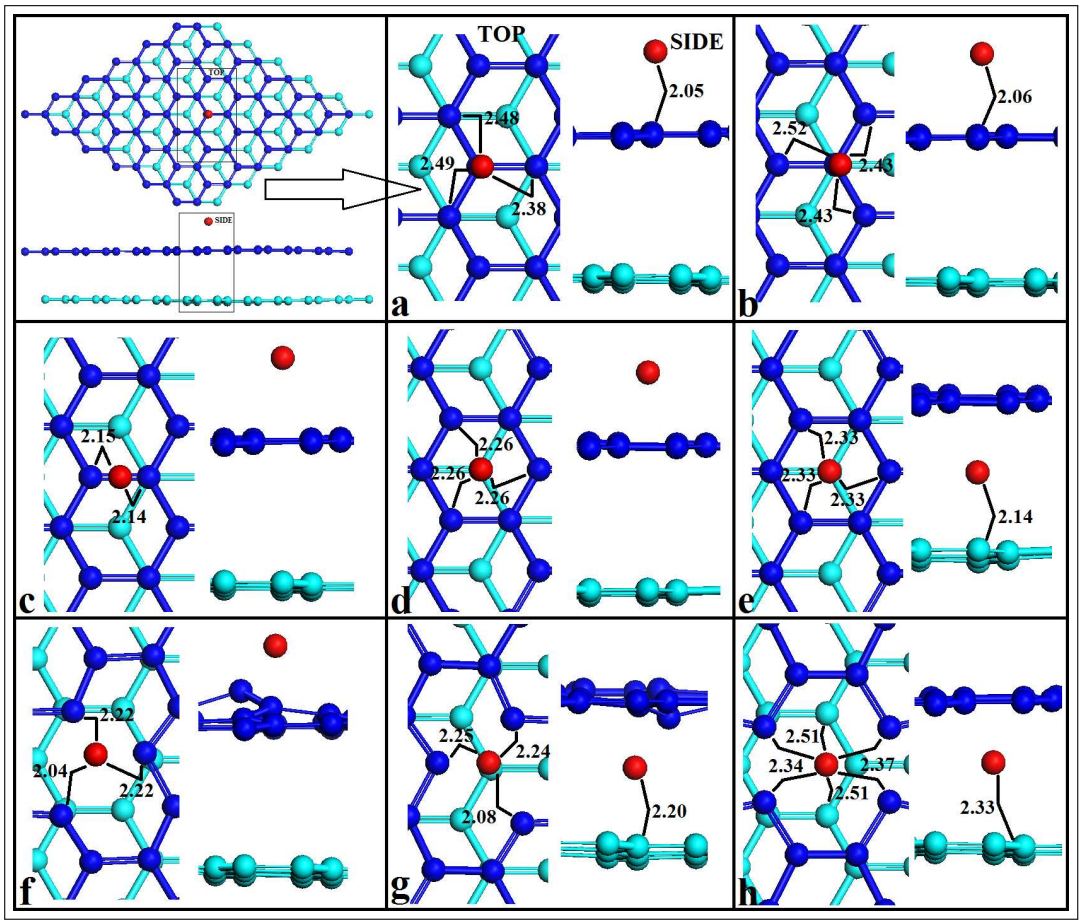

Figure 5.4: Top and side view of 8 different optimized configurations for Li introducd AB stacking bilayer graphene. These final configurations represent a) Outer A atom, b) Outer B atom, c) Outer bridge, d) Outer hollow, e) Mid hollow, f) A substitution, g) B substitution, h) Double C vacancy, which are presented in table 5.2 (Colour convention is the same as in figure 5.4).

is the one where B type carbon atom, "Double C vacancy" (figure 5.4h) is the one where an A type and neighbouring B type carbon atoms are replaced with a single lithium atom. Average Li-C bond distance for GGA is 2.20 Å and for LDA is 2.11 Å. For single vacancy cases, the distance between lithium and carbon atoms are 1.42 Å in initial configurations, which are too close. In order to increase the distance above 2 Å, lithium atom goes inside the graphene layers. For double vacancy case, however, initial distance between carbon and lithium atoms is 1.85 Å. Still its too tight to stand still and lithium atom again moves inside (or outside) the graphene layers. Binding energies of substitutions are greater than all of the possible cases because we have a vacancy or two to be healed. Healing a vacancy has a great advantage, energetically, rather than just binding to a complete graphene structure.

5.2.4 Charge Transfer

Some charge is transferred from lithium to the graphitic system. Transferred charge for the final configurations of AA stacking are shown in the third and sixth column of table 5.1 and similarly the transferred charge for the final configurations of AB stacking are shown in table 5.2. Charge transfer for GGA or LDA potetials do not differ much. In average 0.88 e^- is transferred from lithium to the graphitic system. Since lithium has one valance electron, we can say that most of the valance electron of lithium is transferred to the graphitic system (88

In figure 5.5 the transferred charge is displayed by presenting the difference charge density, calculated by subtracting the charge densities of graphitic system and Li atom from the charge density of a) intercalated system, b) substitutional system for AA stacking. From the figure 5.5a, it can be depicted that all carbon atoms in graphitic hexagons share the incoming electron. This electron is distributed symmetrically. Moreover, the extra electron tends to accommodate in the form of p_z orbital of the carbon atoms. For the defected case shown in figure 5.5b, the extra charges accommodate around the missing carbon atom to compensate the dangling bonds. In this case, p_z orbital is tried to be accommodated, however, for the carbons around the missing one other orbitals take some

electrons as well.

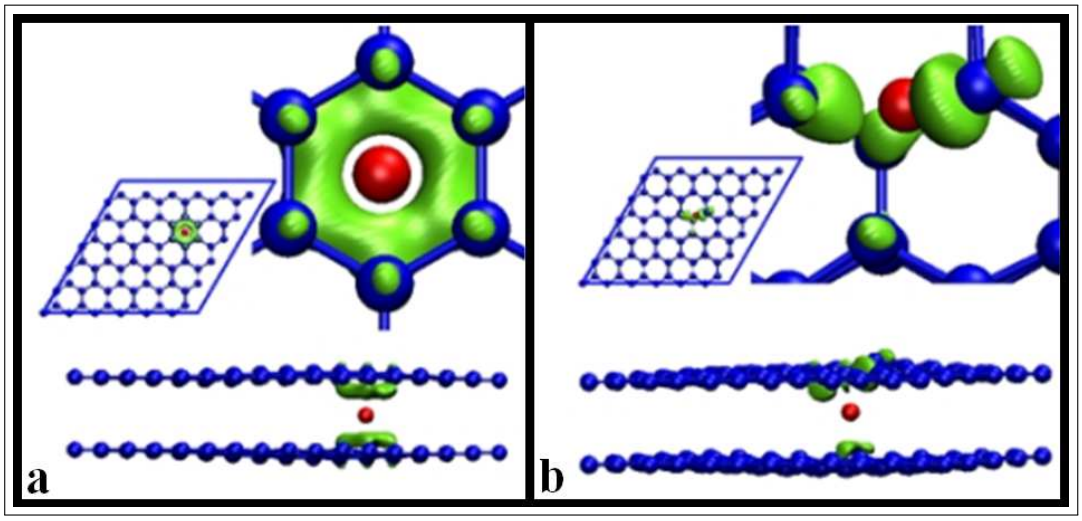

Figure 5.5: Top view, zoomed view, and side view of the transferred charge a) AA Mid hollow, b) AA A substitution cases (Blue atoms = C atoms, Red atom = Li atom, Green bubbles = Transferred charge).

5.3 Discussions

In order to understand the chemistry between Li atom and a graphitic system we have performed density functional theoretical analysis both with GGA and LDA potentials. It seems that GGA and LDA results do not differ significantly for this purpose.

The lithium atom makes bonds with carbon atoms that are 2.15 Å long. Lithium also tends to have as many neighbours as possible. The most stable final configuration is AA stacking "Mid hollow" case, where Li atom sits in between the centers of the hexagons of upper and lower layers having 12 nearest neighbours. All intercalation systems have stronger binding with respect to the adsorption cases. Therefore, intercalation is more likely (if possible) for lithium atom rather than adsorption. Lithium atom has one valance electron and in average it gives

0.88 of it the the graphitic system. This extra electron on graphitic layer is distributed symmetrically to the neighbours of lithium, moreover, the extra charge tends to accommodate the p_z orbitals of these carbon atoms.

Chapter 6

Super Periodic Graphitic Structures: Moire Pattern

Understanding the effects of surfaces in a system has crucial importance both in chemistry and physics. A defect [131,132], a buckling, a foreign atom, periodicity [133], etc. can change the direction of the evolution of the system. Therefore, imaging a surface and understanding the physics behind is a very important phenomena. Thanks to STM (Scanning Tunneling Microscope) [134] and other imaging devices and techniques, nowadays we are capable of having images with atomic resolution.

As a first example, STM is used to image HOPG (Highly oriented pyrolytic graphite) [59–64, 135–146] since it can be observed in vacuum, atmospheric and even in aqueous environments. It is well known that an AB stacking graphite has a honeycomb structure and has two A type and two B type atoms in the unit cell. One A atom is on top of the other being in different layers, whereas B type atoms have the center of hexagon on top [141] (or bottom), being in different layers just like the ones shown in figure 6.5. However, in STM images, only one type of atoms are visible [59, 60] which are widely accepted to be B type ones [140] (see figure 6.1a). This situation has become a popular phenomenon and many hypotheses are proposed to explain it [140].

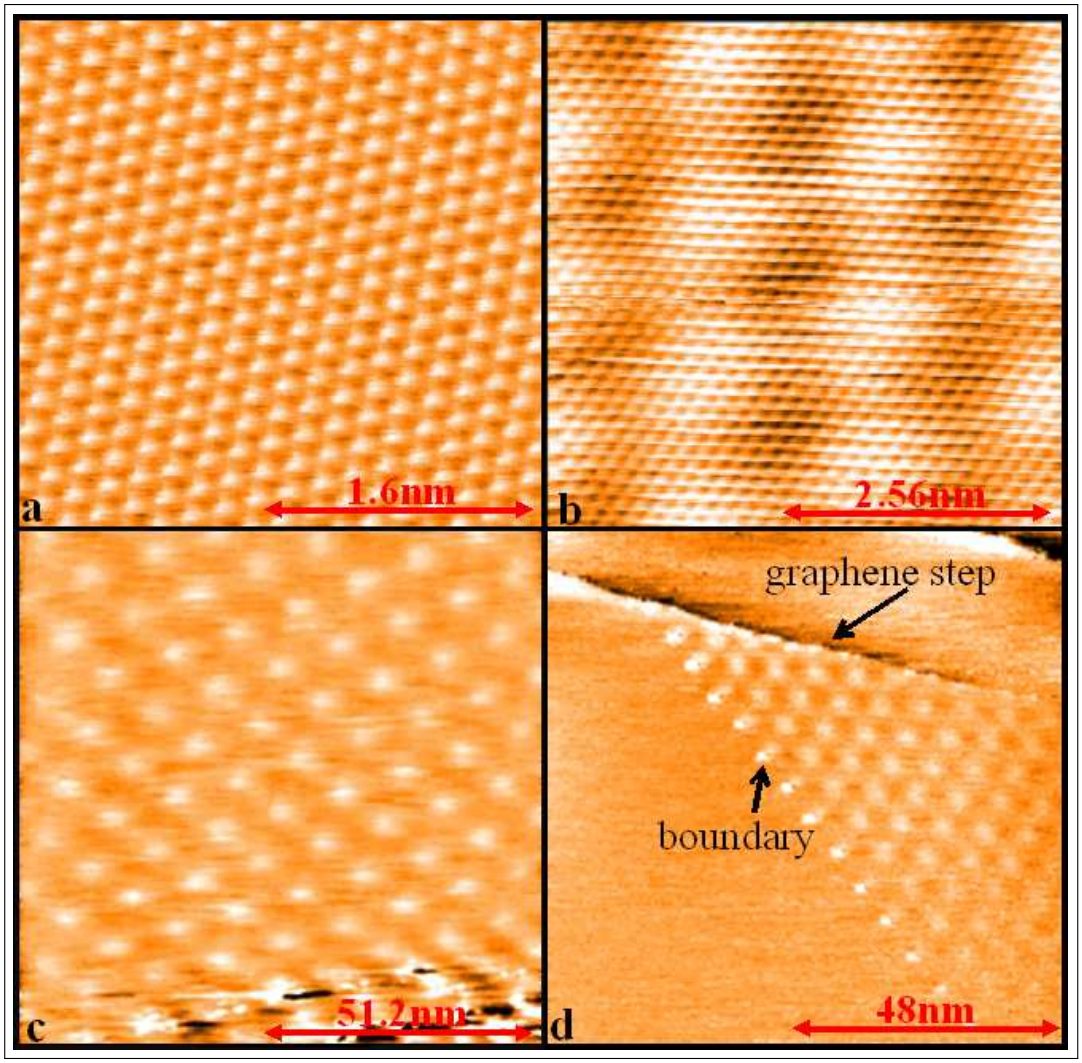

Figure 6.1: STM images of various graphitic structures (from Dilek Yıldız et al.): a) HOPG with tunnelling current of -0.5nA, bias voltage of 50mV (bright dots represent the points with high charge density, in this case one type of the carbon atoms), b) Moire pattern with atomic resolution with tunnelling current of 0.4nA, bias voltage of 50mV, c) another Moire pattern with tunnelling current of 0.7nA, bias voltage of 430mV, d) Moire pattern having a boundary and a graphene step with tunnelling current of 0.7nA, bias voltage of 300mV.

As a second example, large super-periodicities of HOPG structures are imaged using STM [61–67]. Some of the possible physical origins for the super-periodic

structures are multiple tip effects [138], foreign atom intercalation, immersion in aqueous solution [65, 147], and Moire pattern formation [61–63, 68]. The rotational Moire pattern assumption tells us that the top most layer of the graphite is rotated with respect to the layers underneath. In order to obtain a Moire pattern structure, there are four main experimental conditions, (1) HOPG is prepared under dry conditions and then immersed in aqueous solutions or in organic solvents [65, 148], (2) metal atoms are deposited on monolayer graphite (or HOPG surface) [63, 149–151], (3) HOPG has grain boundaries, lattice dislocations, defects, or steps [152–159] and (4) treating continuous trials with adhesive tape [155, 160]. However, it is not possible to repeat the same experiment and obtain exactly the same Moire pattern.

Some Moire pattern STM images are shown in figure 6.1b,c,d. All of the images in the figure were supplied by Dilek Yıldız studying at Istanbul Technical University, Turkey under the supervision of Associate Professor Doctor Oğuzhan Gürlü. Images in the figure are obtained under different tunnelling currents and bias voltages. Figure 6.1a, shows the STM image of HOPG. Since STM creates images of the charge density on the surface by tunnelling, the bright spots are the points where there is high charge density with respect to the vicinity of the point. At this image bias voltage is -50mV, so only the electrons between the energies -50mV - 0eV (Fermi level) in the band structure are tunnelled from the surface to an outer circuit through the STM tip. The only electrons in that energy range are the unpaired electrons in p_z orbital of carbon atoms. Therefore, the bright spots show the positions of carbon atoms. However, the distance between the bright spots are just the same as the lattice constant in the plane of graphene, i.e. if one draws a parallelogram with the bright spots at the corners it would be the unit cell of graphene. In the unit cell of graphene, there is one A type and one B type atom and the bright spots show the position of only one of them. This means that A type and B type atoms should have a difference in the density of electrons having the energy in the range mentioned. We will show the calculations about it later. In figure 6.1b,c and d, images of various Moire patterns observed are shown. Here, the bright spots do not represent single carbon atoms, but there is a super periodicity with a much larger lattice constant than graphene.

In figure 6.1b with atomic resolution that large so called Moire periodicity and the graphene periodicity are both visible. Of course, all of the Moire patterns are not perfect as in figure 6.1c and d there are boundaries and edges obtained.

In this chapter, we investigate the Moire patterns that are observed by Dilek Yıldız et al. in rotated graphitic structures, using first principles calculations. The main idea is to explain the origin of the images by the charge density of the rotated system. In addition to this, detailed geometrical calculations are introduced for the generation of unit cell of the structures.

6.1 Computational Method

In this work we have performed first principles plane-wave calculations [79] within density functional theory [74,75] by the projector-augmented-wave (PAW) potentials [90, 91]. For this purpose we have used Vienna ab-initio simulation package program (VASP) [92, 93]. The exchange-correlation potential was expressed in terms of generalized gradient approximation (GGA) (Perdew-Wang 91 type) [94]. In order to achieve desired accuracy in calculations, plane-wave cutoff energy is set to 500 eV. The partial occupancy around Fermi level is treated by Gaussian smearing with a smearing parameter of 0.08 eV. For all calculations energy convergence was within 10^{-5} eV accuracy. In all calculations, systems are relaxed electronically to their minimum energy configurations by using conjugate gradient method where total energy is minimized.

We have performed periodic calculations, however, for the structures we are interested in, the unit cell is not obvious and simple. In order to find the unit cell we created a method that is explained in the next section. As the size of the unit cell changes, the k-points grid (Monkhorst-Pack [127]) varies accordingly. The larger the unit cell, the smaller the k-points grid size. The greatest k-point grid in our calculations is 23x23x1, and the smallest one is 5x5x1.

6.1.1 Unit Cell Generation

First of all, we set the position of the rotation axis. Let's consider only a single graphene layer and say the rotation axis passes through a lattice point of the graphene, perpendicular to the layer. We can put this lattice point wherever we want on the graphene, but for simplicity, let's say the lattice point is in the center of a hexagon at point O (Origin). The graphene plane, lattice vectors ($\vec{a}_1$ and $\vec{a}_2$), origin O where the rotation axis pass through and other directions and vectors to be explained later are shown in figure 6.2 below. Now, we define a vector $\vec{R}_1$ as in equation 6.3.

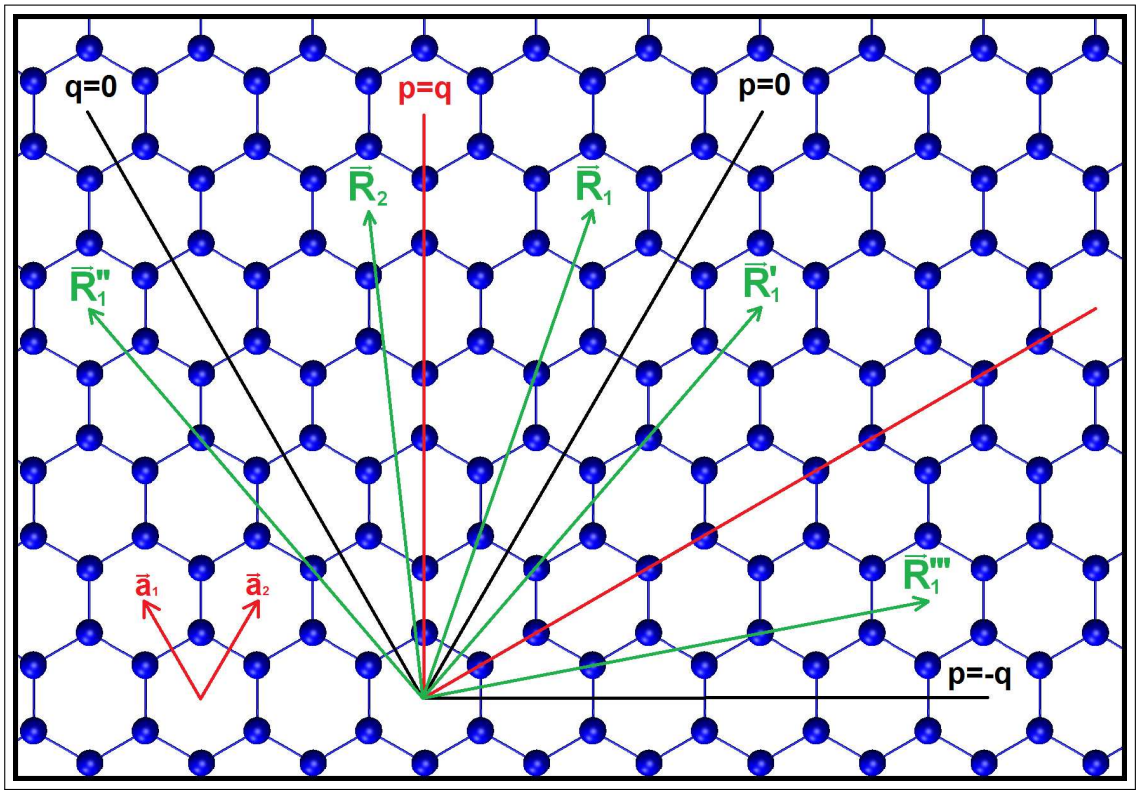

Figure 6.2: Unit cell generation figure; O is the origin (The point rotation axis pass through), $\vec{a}_1$ and $\vec{a}_2$ are lattice vectors for graphene, $\vec{R}_1$ and $\vec{R}_2$ are the vectors that are rotated onto $p = 0$ and $p = q$ lines to generate the necessary unit cells.

$$\vec{R}_1 = p_1\vec{a}_1 + q_1\vec{a}_2 \tag{6.1}$$

where p_1 and q_1 are positive integers ($p_1 \leq q_1$); $\vec{a}_1$ and $\vec{a}_2$ are the lattice vectors of graphene. We can define a similar vector $\vec{R}'_1$ symmetric with respect to the $p = 0$ line shown in figure 6.2. Both of the vectors we defined are translation vectors since p_1 and q_1 are integers. Therefore, these vectors define another lattice point of graphene as well. Now, we consider two graphene layers with AA stacking (AA and AB stacking has no difference in the end), i.e. bilayer graphene. Let $\vec{R}_1$ be a vector at the top layer and $\vec{R}'_1$ be a vector at the bottom layer. If we rotate the top layer (so the $\vec{R}_1$ vector) by some angle θ clockwise, such that $\vec{R}_1$ coincides with the $p = 0$ line and rotate the bottom layer (as well as $\vec{R}'_1$ vector) by the same angle θ counter clockwise, the two vectors will just sit on top of each other, therefore, two lattice points will be one over another, just like the lattice points the rotation axis pass through. If p_1 and q_1 are prime among themselves, there is no other lattice points coinciding with each other on these vectors. Then, with such a rotation, we find a second lattice point of the rotated system. Moreover, these two lattice points are the closest possible ones. Since lattice points of graphene has six fold rotational symmetry, we have similar lines and vectors with $p = 0$ line ($q = 0$,$p = -q$), $\vec{R}_1$ ($\vec{R}''_1$,$\vec{R}'''_1$) and $\vec{R}'_1$ vectors at $\pm 60^o$. Therefore, other lattice points are generated as well, which can be easily shown by rotating the original lattice point around the rotation axis $\pm 60^o$. After finding the three lattice points on the lines $p = 0$, $p = -q$ and $q = 0$ we use these points with origin to make a parallelogram which is the unit cell. Since the two vectors are both rotated in opposite directions by angle θ, the top layer is rotated by 2θ with respect to the bottom layer. Therefore, the rotation angle is said to be 2θ which can be given by

$$\theta_{Rotation} = 2\theta = 2 \arctan \frac{\sqrt{3} p_1}{2 q_1}. \tag{6.2}$$

For every rotation angle Moire pattern occur because in equation 6.2 p_1 and q_1 can take any value as long as $p_1 \leq q_1$ being positive integers. Therefore, if one takes a bilayer graphene and rotate the top layer with respect to bottom one, for every angle there will occur Moire pattern. However, geometrical and STM periodicity will differ if $p_1 > 1$, which will be explained later. In figure 6.3, atomic positions for some rotation angle are shown (the figures do not show the unit cell) to give an idea of how it looks like.

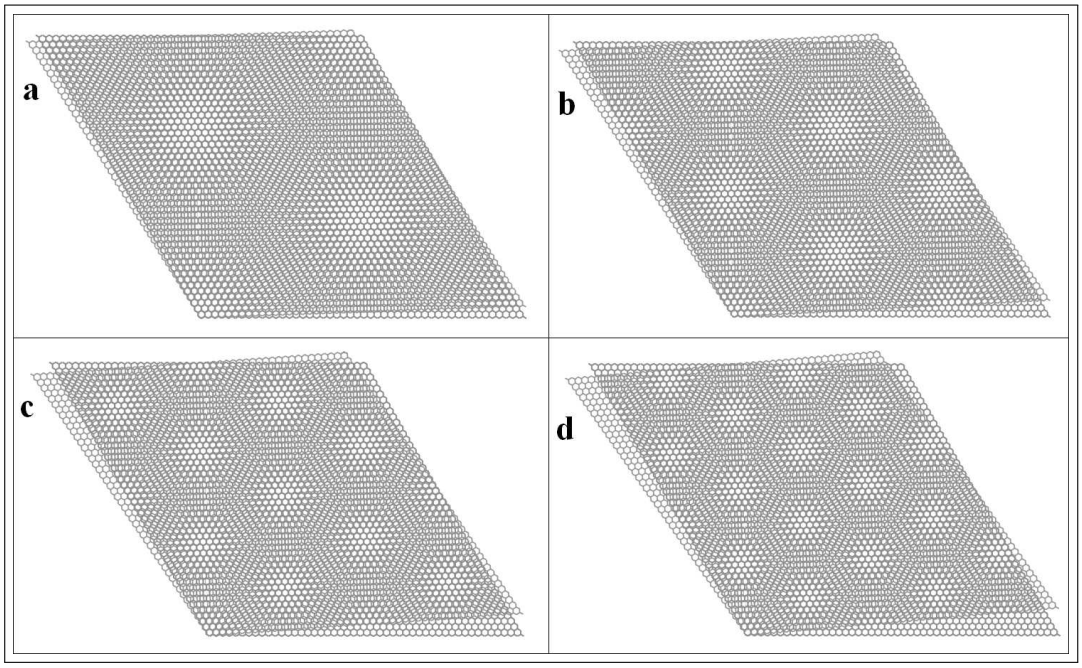

Figure 6.3: Rotated bilayer graphene structures with angle a) 2^o, b) 3^o, c) 4^o, d) 5^o.

Now, if we return to the generation of unit cell, we set the line that $\vec{R}_1$ vector will be rotated onto, as $p = 0$ line which is an armchair direction. However, instead of $p = 0$ line, we can choose $p = q$ line which is in zigzag direction and $\vec{R}_2$ vector as the translation vector. And then apply the same procedure to create the unit cell. Will this make a difference? The answer to this question is affirmative. Actually, if the first nearest lattice point to the origin is found by rotating the vector to armchair direction, then, the second nearest lattice point is the one with a vector rotated to the zigzag direction and vice versa. Also, the second nearest lattice point is $\sqrt{3}$ times further to the origin than the first one. Therefore, for some p_1 and q_1 values, we can find a closer lattice point on $p = q$ line. We made the necessary geometrical calculations and found the relations between these lattice points as follows; let $\vec{R}_2$ to be defined as

$$\vec{R}_2 = p_2\vec{a}_1 + q_2\vec{a}_2, \tag{6.3}$$

then, if $\vec{R}_1$ defines the nearest lattice point (so $\vec{R}_1$ defines the second nearest

lattice point),

$$p_1 = \frac{p_2 - q_2}{3}, \tag{6.4}$$
$$q_1 = \frac{p_2 + 2q_2}{3};$$

and if $\vec{R}_2$ defines the nearest lattice point (so $\vec{R}_2$ defines the second nearest lattice point);

$$p_1 = p_2 - q_2 \tag{6.5}$$
$$q_1 = p_2 + 2q_2.$$

Now, lets say $\vec{R}_2$ defines the nearest lattice point and lets subtract p_1 from q_1 using equation 6.6 to get

$$q_1 - p_1 = 3q_2. \tag{6.6}$$
$$\tag{6.7}$$

Since q_2 is an integer we can only have $\vec{R}_2$ defining the nearest lattice vector when $q_1 - p_1 = 0$ (mod3). Therefore, for $\frac{2}{3}$ of possible cases $\vec{R}_1$ defines the nearest lattice vector. For the purpose, we are trying to have as small angle as possible (since STM images show those). Therefore, we set $p_1 = 1$. Then, for the values where $q_1 - 1 = 0$ (mod3), i.e. $q_1 = 4, 7, 10, 13, ...$ we have $\vec{R}_2$ defining the nearest lattice point to the origin. For those special cases we will have half the unit cell we would for $\vec{R}_1$ defining the nearest lattice point case. And the angle of rotation will be $2\theta = 2 \arctan \frac{\sqrt{3}}{2q_1}$.

In this work, the smallest unit cell had 4 carbon atoms, whereas, the greatest had 628 atoms inside. We made single runs, i.e. geometric relaxation was off, only electronic relaxation is done. The distance between the graphene layers is set to be 3.35 Å. The system is periodic in plane, whereas, there is a vacuum more than 10 Å long perpendicular to the planes.

6.1.2 Calculations

Since, we generate the unit cell of the systems by the introduction of p_1 and q_1 values, we created a labeling with these numbers. For instance, we call a

system p1q10 when its unit cell is generated through the rotation of $\vec{R}_1$ which has components with $p_1 = 1$ and $q_1 = 10$. For all of the super periodic structures ($p_1 = 1$ and $q_1 = 7, 8, 9, 10, 11, 12$), we are interested in the charge densities of the system. If we look for the whole charge density of the system, however, we would see very small difference between the total charges of the atoms, which would make them indistinguishable. Also, it would not describe the STM images anyway. Since, STM can interact with only the electrons having at most a few eVs energy around Fermi level depending on the tip bias, we make a second calculation that only focus on those electrons rather than the whole system. In order to do this, we make a post processing of the VASP output. Starting from the WAVECAR file in which wave-functions of the system are described the charge densities around the Fermi level is calculated. This new calculation shows us the charges that will interact with STM tip describing the situation better. After having the charge density file, we can use a visualization program and draw line profiles and isosurfaces [161–164]. In order to understand the current and voltage effects, we draw band structure and density of states of the systems as well.

6.2 Results

In order to understand the number of layers that contribute to the charge density significantly, we tested AB stacking multilayer graphene structures. We started with six layers and went down to two layers, having 3.35 Å between the layers. In all calculations, we checked the charge density 0.8 Å above the top layer. For the figure 6.4, we used the charges within the energy range -0.5 eV to Fermi level. In figure 6.4a, we see the density of charges of carbon atoms for six layers AB stacking graphene. In figure 6.4b, we have the line profile graph of the same calculation for the line shown in the subset. In figure 6.4c, we see the density of charges of carbon atoms for two layers AB stacking graphene. In figure 6.4d, we have the line profile graph of the same calculation for the line shown in subset. As we see from the line profiles there are two peaks one of which is almost 1.25 times greater than the other one. This was what we expected since one type of the atom should be brighter in the STM image as in figure 6.1a. Since, we do

not see appreciable difference in the line profiles, we continue to work with two layers. We used two layers for the rest of the calculations in order to have as less atom as possible and so that to have the largest unit cell area in plane. In order to understand for which energy range we are still able to distinguish the atoms, we employed calculations for the energy ranges from -2.0 eV - Fermi level for the largest difference and -0.25 eV - Fermi level for the smallest difference. In figure 6.4e, charge density 0.8 Å above the to layer for the charges within energy range -1.5 eV to Fermi level of 2 layer AB stacking graphene is shown. In figure 6.4f, line profile for the same charges is drawn. As it can be seen, it is hard to make a distinction between A type or B type carbon atoms. Charge densities and line profile peaks are almost the same. Indeed, if we increase the energy range, we lose the difference. Therefore, we choose the energy range to be -0.5 eV to Fermi level for the rest of the computations.

In figure 6.5b, we see isosurface of charge density (green bubbles) for some isovalue for the same calculation shown in figure 6.4c-d. In order to see the difference better we choose an isovalue in such a way that if we decrease the value just a little bit, we see that green bubbles start to appear on the rest of the carbon atoms as well. Therefore, this figure shows us, let's say, the difference between atom types. The figure enables us to see that red A type carbon atoms (carbon atom below which there is a carbon atom of the second layer) and blue B type atoms (carbon atom below which there is the center of hexagon of the second layer) have different charges and in addition to that B type atoms have significantly more charge than A type ones.

Figure 6.3 shows some different geometrical configurations for some twisted structures with different angles. Some local hexagonal patterns start to appear as we twist the structure. For any angle, there occur hexagonal patterns as we mentioned earlier. The periodicity of these patterns seems to get smaller as the angle increases. Actually the periodicity D of these patterns is given by,

$$D = \frac{a}{2sin\theta}, \tag{6.8}$$

where a is the length of the lattice constant of graphene, i.e. 2.46 Å, and θ is the half of the rotation angle [68,160]. According to these calculations, the periodicity

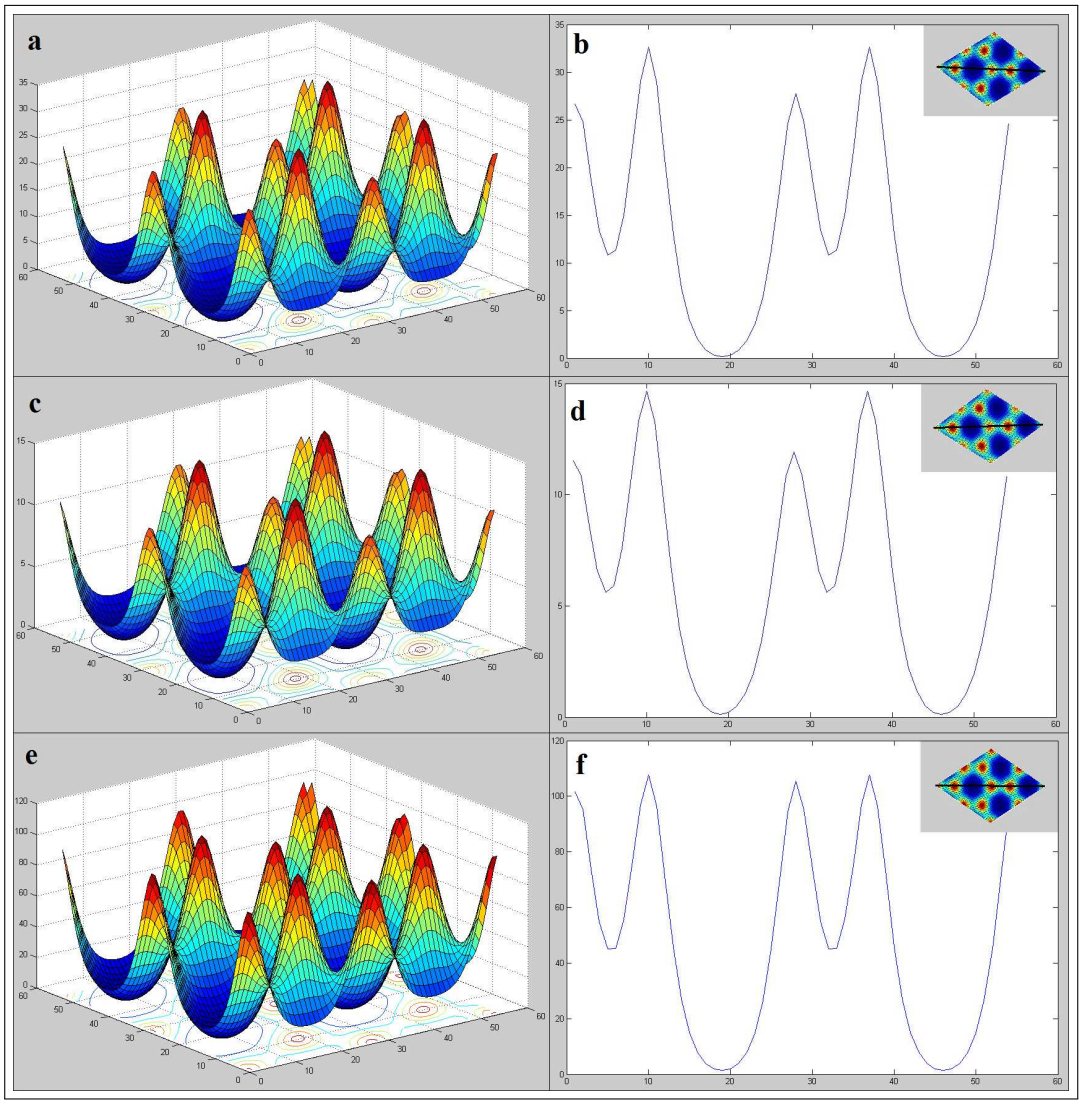

Figure 6.4: Charges within the energy window -0.5 eV to Fermi level for AB stacking graphene 0.8Å above the top layer a) Charge density for 6 layer, b) Line profile for 6 layer, c) Charge density for 2 layer, d) Line profile for 2 layer. Charges within the energy range -1.5eV to Fermi level for AB stacking graphene 0.8Å above the top layer e) Charge density for 2 layer, f) Line profile for 2 layer.

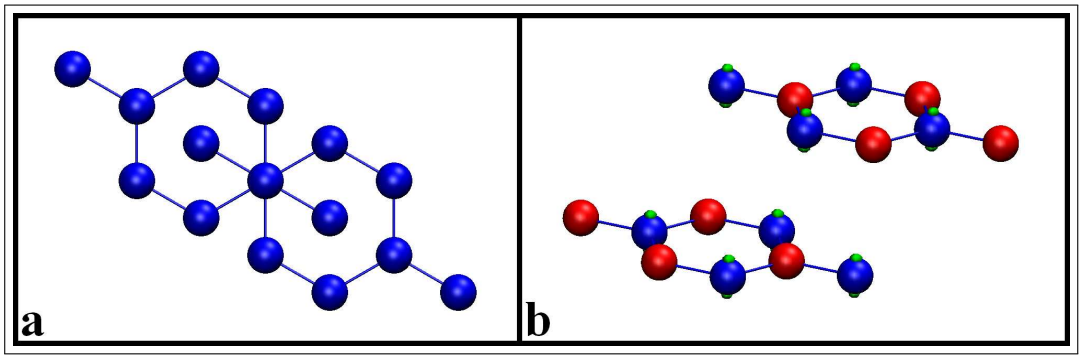

Figure 6.5: a) Unit cell of 2x2 AB stacking bilayer graphene from top view, b) 2x2 AB stacking bilayer graphene from side view with charge isosurface within the range -0.5eV to Fermi level. (Green bubbles are the isosurface of the charge density for some isovalue, red spheres are A type and blue spheres are B type carbon atoms.)

of the pattern is D for only some cases and D only shows the distance between the bright spots in the STM images. However, the local patterns may not be similar and indeed they are different when $p_1 \neq 1$. Moreover, even when $p_1 = 1$, the periodicity of the pattern is D only when $\vec{R}_2$ defines the nearest lattice vector. In short, although D seems to be periodicity of the bright spots in STM images, it is only the periodicity of the system when $\vec{R}_2$ defines the lattice vector and $p_1 = 1$. The actual periodicity of the system is $D_{actual} = p_1 D$ when $q_1 - p_1 = 0$ (mod3), and $D_{actual} = \sqrt{3} p_1 D$ when $q_1 - p_1 \neq 0$ (mod3). Then, it will not be meaningful to say that the patterns are periodic with some length for some angle, unless you do not know the $\vec{R}_1$ vector exactly, i.e. p_1 and q_1. It is impossible to define p_1 and q_1 and make the graphitic structures rotated accordingly with the present experimental techniques.

In figure 6.6a, rotated p1q10 structure is shown. For this structure since $10 - 1 = 9 \equiv 0$ (mod3) $\vec{R}_2$ defines the nearest lattice vector and the unit cell is the gray parallelogram. Notice that in this figure, each hexagonal pattern are the same. In figure 6.6b, rotated p1q11 structure is shown. For this structure $11 - 1 = 10 \neq 0$ (mod3), therefore, $\vec{R}_1$ defines the nearest lattice vector and the unit cell is the gray parallelogram. Notice that the pattern at the corners of the unit cell and inside the unit cell are all different.

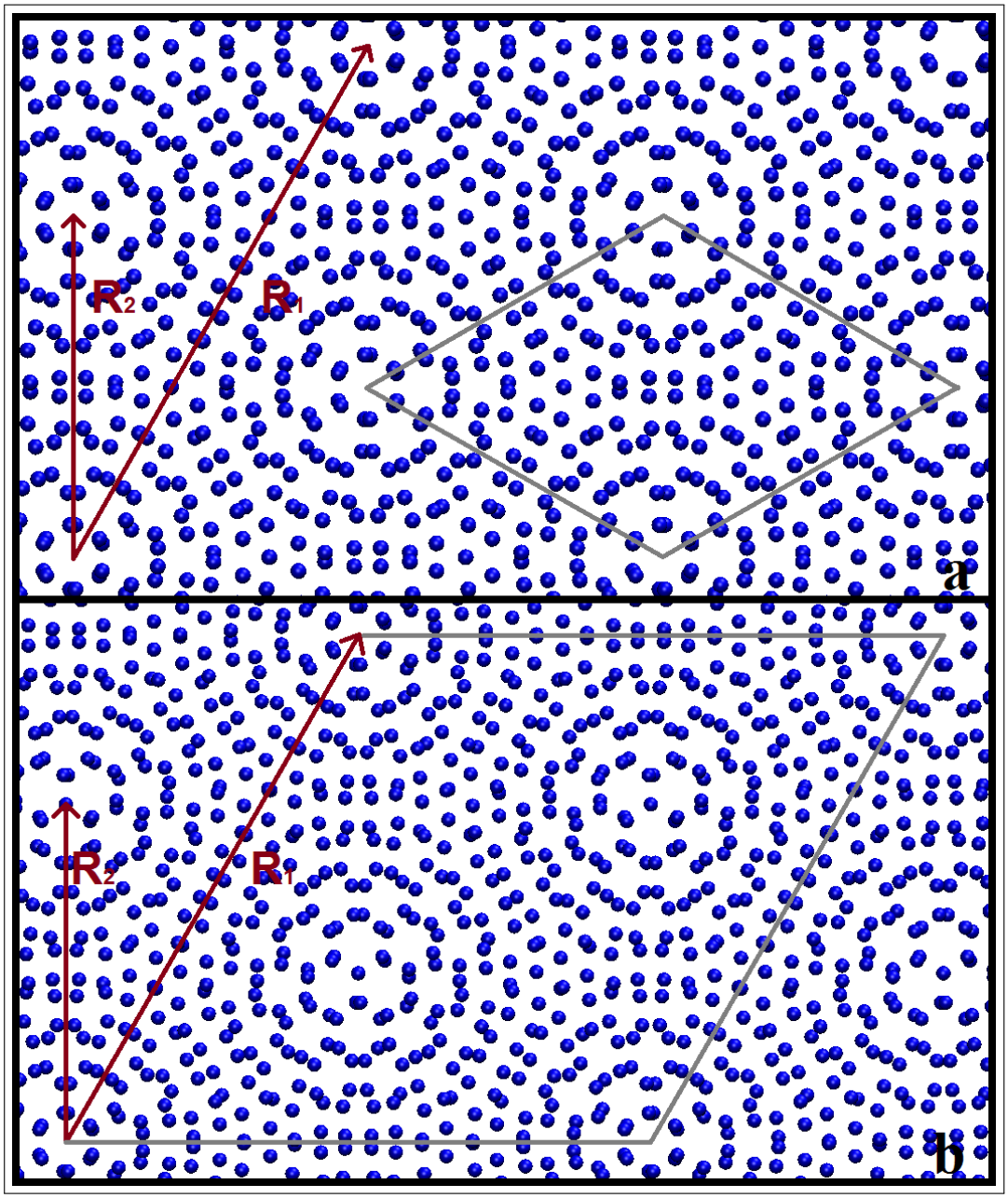

Figure 6.6: Rotated a) p1q10, b) p1q11 structures with $\vec{R}_1$ and $\vec{R}_2$ vectors and the unit cell of the system.

Figures 6.7 and 6.8 summarizes our results with the help of p1q11 system as an example. In figure 6.7a, top view of the unit cell of p1q11 system is shown within the gray paralellogram. All spheres are carbon atoms and yellow, orange, black and red spheres are the atoms around the regions we will discuss on. In figure 6.7b, we show the charge density isosurface plot of the same system (just like the ones in figure 6.5b) to see where the bright spots would appear in STM image. The yellow line with signs $1, *, ., +, 2$ in the figure represents positions for the line profile direction shown in figure 6.7d. In figure 6.7c, side view of the unit cell of p1q11 system with both carbon atoms and the isosurface plot is shown. In figure 6.8a, the density of states of the investigated systems within the energy range from -0.5eV to 0.5eV are shown. Similarly, in figure 6.8b, we plot the partial density of states of the carbon hexagons represented with different colors in figure 6.7a. With the help of these figures we will discuss the super-periodic Moire pattern in rotated graphitic systems.

6.3 Discussions

In this chapter, we investigated the super-periodic graphitic structures using density functional theory. We have shown that two layers are enough to describe the graphitic super-periodic systems. We have also shown that although the pattern periodicity in STM images are D, actual periodicity of the system can be different but indistinguishable with the current technology. With the help of figure 6.5, we understood that A type atoms differ from B type atoms. Therefore, our first expectation was to see the carbon atoms with another carbon atom at the bottom (A type) to have less charge density with respect to the ones with the center of hexagon at the bottom (B type). However, we noticed that after the system is rotated there was no A type or B type atoms anymore, but "AA stacking, AB stacking, AC stacking and no stacking" regions instead. AC stacking is similar to AB stacking. If we shift AA stacked bilayer graphene in one direction by one bond distance to get AB stacking, we get AC stacking when we do the same shift in the same direction one more. Then, if we shift one more time, we get back to AA stacking. In figure 6.7a, we circulated these regions with different stacking

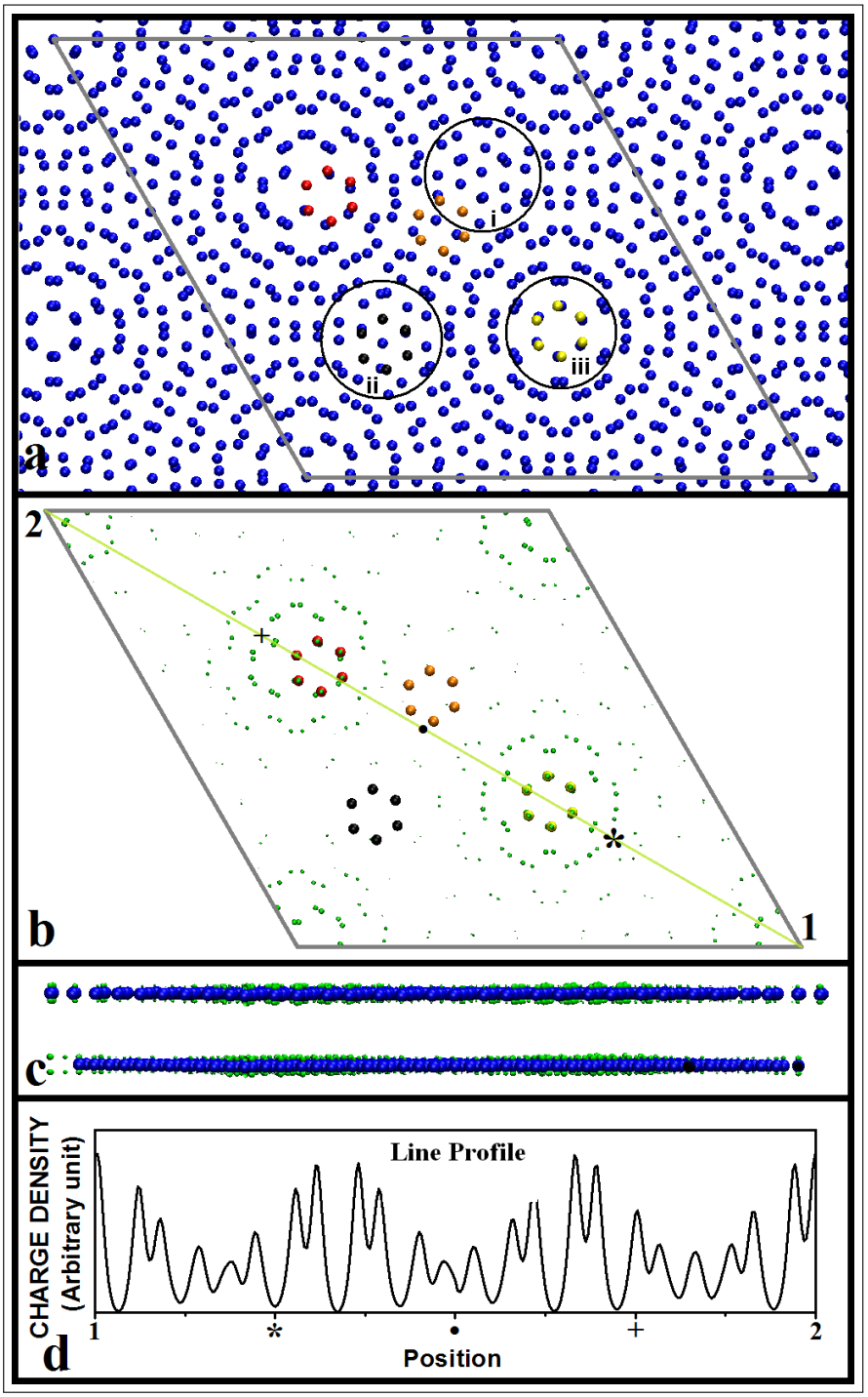

Figure 6.7: a) Top view of the unit cell of rotated p1q11 structure (Spheres are carbon atoms), b) charge density isosurface plot of p1q11 system (Green dots are the isosurfaces for some isovalue), c) side view of the same system with carbon atoms (Blue spheres) and isosurface of charges (Green dots), d) line profile of the charge density of p1q11 system in the direction from 1 to 2 as shown in b.

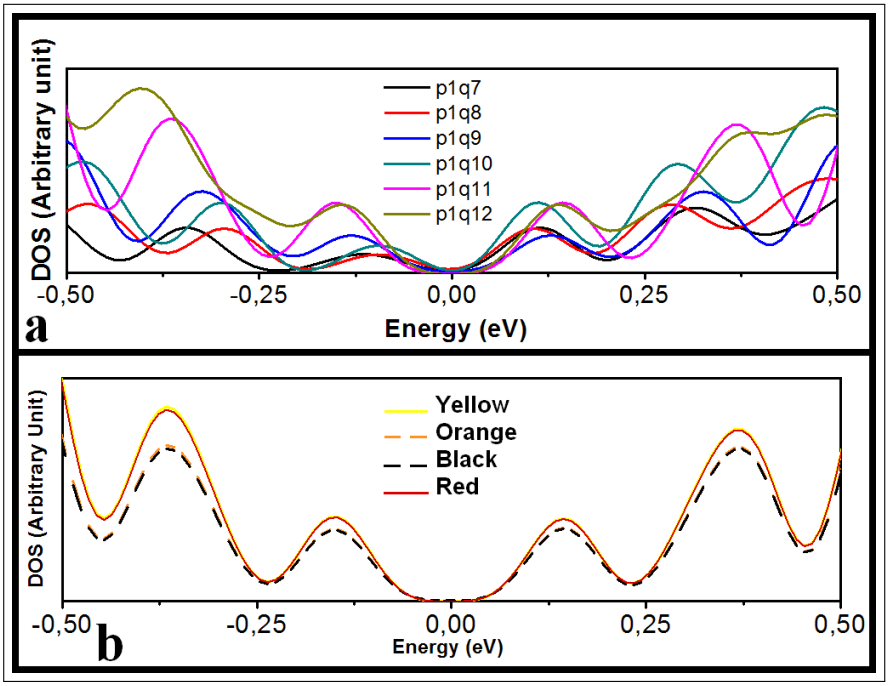

Figure 6.8: a) Density of states of the investigated systems within the energy range from -0.5eV to 0.5eV, b) partial density of states of the carbon hexagons shown in figure 6.7a.

and numbered as i, ii, and iii. If one looks closely, it can be noticed that iii region is an AA stacking region, where all carbon atoms have another carbon atom almost at the bottom of it, whereas, ii and i regions are AB and AC stacking regions which are composed of A type and B type atoms. Just at the center of the triangle connecting these three regions there is the no stacking region. Notice that iii region, the corners of the unit cell, and the region around red carbons all have AA stacking. Although, they do not exactly have the same geometry, they have similar stacking. From figure 6.7b, it can be depicted that AA stacking regions has the greatest local density of charges and should be bright in STM image with the periodicity D creating a triangular lattice. Figure 6.7c tells us that these charges are all coming from p_z orbital of carbons. Line profile of the system shown in figure 6.7d makes it clear that AA stacking regions have more charges with respect to neighbouring regions. The highest peaks occur around point 1 and 2, just after $*$ and just before $+$ all of which are AA stacked regions. By the help of the figure 6.8a, we can state that density of states are asymmetric with respect to Fermi level for all systems. Also, since the system does not lose the hexagonal symmetry, there is no energy band gap as the valance and conduction bands touch each other at Fermi level. Another important observation is that there are two or three peaks within the energy range from -0.5eV to Fermi level in all systems. Other than that, we could not observe a correlation between systems. In figure 6.8b, partial density of states of the carbon hexagons shown in figure 6.7a are drawn. This figure tells us that the peaks in the density of states of p1q11 shown in figure 6.8b cannot be attributed to single atoms, but there is a cumulative contribution from all atoms. In addition to this, since the integration of DOS or PDOS over energy gives the number of charges, we can again state that yellow and red atoms, which are all in AA stacking regions have more charges than others and will appear as bright regions in the STM image.

Chapter 7

Conclusions

In this thesis, we investigated various graphitic nanostructures from first-principles calculations. In order to do this, we employed tight binding approximation and density functional theory.

In chapter three, we investigated the electronic band structure of one and zero dimensional graphene nano-ribbons using tight binding method. We concluded that all of the zigzag type graphene nano-ribbons have zero band gap value. Armchair graphene nano-ribbons as well as zero dimensional chiral graphene nano-ribbons, however, can have various band gaps which can be calculated via equation 3.6. One dimensional armchair graphene nano-ribbons show three distinct family behaviour having different A and a values in the equation. Another important observation was that one dimensional zigzag and armchair graphene nano-ribbons have very different band structures and the band structure of certain one dimensional chiral graphene nano-ribbons look alike the band structure to one dimensional zigzag graphene nano-ribbons, whereas, others look alike the band structure of armchair ones.

In chapter four, we investigated the effect of phosphorus and sulfur atoms on the growth mechanism of CNTs via density functional theory. In order to do that we investigated the chemistry and interaction of P and S atoms with graphene layer, a kink structure as well as C-P and C-S cluster structures. We

have shown that phosphorus and sulfur atoms interact similarly with graphene and kink structure. Both of these atom types tend to escape from the graphitic surface as they find a partner unless there is a vacancy. Although, phosphor and sulfur atoms behave in a similar manner with a complete graphitic structure, they behave differently while interacting with carbon clusters. As a result of the investigations, we can conclude that phosphorus atoms tend to make cluster structures with carbon atoms binding strongly, whereas, sulfur atoms break the clusters and increase the number of free carbons. Therefore, during growth of CNTs, phosphorus atoms make cluster with carbon atoms and decreases the number of free carbon atoms available for nanotube growth leading thin and short CNTs with low quantity. Moreover, these phosphorus atoms can enter the nanotube network binding to a carbon atom and create clusters there which results in low graphitization. The situation is just opposite for the sulfur though. Sulfur atoms tries to destroy any carbon cluster increasing the number of free carbon atoms available for nanotube construction. Therefore, nanotubes grow thick, long and high in quantity with high graphitization.

In chapter five, we discussed the chemistry between Li atom and bilayer graphene to investigate the intercalation of Li atom into MWCNTs. In order to do this, both GGA and LDA potentials are employed in density functional calculations and we ended up with the same conclusions. According to our calculations Li-C bond distance is around 2.15 Å and Li atom tends to have as much neighbour as possible. Therefore, energetically the most stable configuration was AA stacking mid-hollow case, where Li atom sits in between the centers of the hexagons of upper and lower layers having 12 nearest neighbours. Moreover, all the systems with intercalation have stronger binding with respect to the adsorption cases. Therefore, intercalation is more likely for lithium atom rather than adsorption. Li atom gives $0.88e^-$ to the graphitic system, therefore, there is a partial charge transfer. This incoming charge is shared among the neighbouring carbon atoms accommodating the p_z orbitals of these atoms.

In chapter six, we investigated the super-periodic graphitic structures using density functional theory. Two layers of graphene was enough to describe the system. We showed that the pattern periodicity in STM images and the actual

periodicity of the system are different but indistinguishable with the current technology. There are four main regions in rotated graphitic systems which we call "AA, AB, AC and no stacking" regions and these patterns appear in AA stacking regions creating a triangular lattice via charge density isosurface, line profiles of charges and local density of states analysis. These charges are accommodated in p_z orbital of carbons. The density of states of all investigated systems are asymmetric with respect to Fermi level. We also observed some peaks in the valance band around the Fermi level which cannot be attributed to certain carbon atoms, but all atoms contribute to create these peaks.

In conclusion, various graphitic nanostructures are investigated from first principles. Many physical properties of the systems such as band structures, charge densities and density of states are calculated to draw the relevant properties of the considered systems.

Bibliography

[1] M. Endo, T. Hayashi, Y. A. Kim, M. Terrones, and M. S. Dresselhaus, "Applications of carbon nanotubes in the twenty-first century," *Philosophical Transactions of the Royal Society of London. Series A: Mathematical, Physical and Engineering Sciences*, vol. 362, Oct. 2004.

[2] A. K. Geim and K. S. Novoselov, "The rise of graphene," *Nature Materials*, vol. 6, pp. 183–191, Mar. 2007.

[3] M. J. Allen, V. C. Tung, and R. B. Kaner, "Honeycomb carbon: A review of graphene," *Chemical Reviews*, vol. 110, pp. 132–145, Jan. 2010.

[4] K. S. Novoselov, A. K. Geim, S. V. Morozov, D. Jiang, Y. Zhang, S. V. Dubonos, I. V. Grigorieva, and A. A. Firsov, "Electric field effect in atomically thin carbon films," *Science*, vol. 306, Oct. 2004.

[5] K. S. Novoselov, A. K. Geim, S. V. Morozov, D. Jiang, M. I. Katsnelson, I. V. Grigorieva, S. V. Dubonos, and A. A. Firsov, "Two-dimensional gas of massless Dirac fermions in graphene," *Nature*, vol. 438, pp. 197–200, Nov. 2005.

[6] Y. Zhang, Y.-W. Tan, H. L. Stormer, and P. Kim, "Experimental observation of the quantum Hall effect and Berry's phase in graphene," *Nature*, vol. 438, pp. 201–204, Nov. 2005.

[7] J. Wu, W. Pisula, and K. Müllen, "Graphenes as potential material for electronics," *Chemical Reviews*, vol. 107, pp. 718–747, Mar. 2007.

[8] A. H. Castro Neto, F. Guinea, N. M. R. Peres, K. S. Novoselov, and A. K. Geim, "The electronic properties of graphene," *Reviews of Modern Physics*, vol. 81, pp. 109–162, Jan. 2009.

[9] J. Dai, J. Yuan, and P. Giannozzi, "Gas adsorption on graphene doped with B, N, Al, and S: A theoretical study," *Applied Physics Letters*, vol. 95, pp. 232105–232105–3, Dec. 2009.

[10] S. Y. Zhou, D. A. Siegel, A. V. Fedorov, and A. Lanzara, "Metal to insulator transition in epitaxial graphene induced by molecular doping," *Physical Review Letters*, vol. 101, p. 086402, Aug. 2008.

[11] L. Rosales, M. Pacheco, Z. Barticevic, A. Latgé, and P. A. Orellana, "Conductance gaps in graphene ribbons designed by molecular aggregations," *Nanotechnology*, vol. 20, p. 095705, Mar. 2009.

[12] J. Berashevich and T. Chakraborty, "Tunable band gap and magnetic ordering by adsorption of molecules on graphene," *Physical Review B*, vol. 80, p. 033404, July 2009.

[13] R. M. Ribeiro, N. M. R. Peres, J. Coutinho, and P. R. Briddon, "Inducing energy gaps in monolayer and bilayer graphene: Local density approximation calculations," *Physical Review B*, vol. 78, p. 075442, Aug. 2008.

[14] P. A. Denis, R. Faccio, and A. W. Mombru, "Is it possible to dope single-walled carbon nanotubes and graphene with sulfur?," *ChemPhysChem*, vol. 10, no. 4, pp. 715–722, 2009.

[15] J. Dai and J. Yuan, "Modulating the electronic and magnetic structures of P-doped graphene by molecule doping," *Journal of physics. Condensed matter: an Institute of Physics journal*, vol. 22, June 2010.

[16] P. A. Denis, "Band gap opening of monolayer and bilayer graphene doped with aluminium, silicon, phosphorus, and sulfur," *Chemical Physics Letters*, vol. 492, pp. 251–257, June 2010.

[17] A. G. Garcia, S. E. Baltazar, A. H. R. Castro, J. F. P. Robles, and A. Rubio, "Influence of S and P doping in a graphene sheet," *Journal of Computational and Theoretical Nanoscience*, vol. 5, no. 11, pp. 2221–2229, 2008.

[18] X. Wang, X. Li, L. Zhang, Y. Yoon, P. K. Weber, H. Wang, J. Guo, and H. Dai, "N-doping of graphene through electrothermal reactions with ammonia," *Science*, vol. 324, May 2009.

[19] J. O. Sofo, A. S. Chaudhari, and G. D. Barber, "Graphane: A two-dimensional hydrocarbon," *Physical Review B*, vol. 75, p. 153401, Apr. 2007.

[20] I. Zanella, S. Guerini, S. B. Fagan, J. Mendes Filho, and A. G. Souza Filho, "Chemical doping-induced gap opening and spin polarization in graphene," *Physical Review B*, vol. 77, p. 073404, Feb. 2008.

[21] A. A. Avetisyan, B. Partoens, and F. M. Peeters, "Electric field tuning of the band gap in graphene multilayers," *Physical Review B*, vol. 79, p. 035421, Jan. 2009.

[22] R. Saito, G. Dresselhaus, and M. S. Dresselhaus, *Physical Properties of Carbon Nanotubes*. Imperial College Press, Jan. 1998.

[23] P. R. Wallace, "The band theory of graphite," *Physical Review*, vol. 71, pp. 622–634, May 1947.

[24] M. Y. Han, B. Özyilmaz, Y. Zhang, and P. Kim, "Energy band-gap engineering of graphene nanoribbons," *Physical Review Letters*, vol. 98, p. 206805, May 2007.

[25] Y.-W. Son, M. L. Cohen, and S. G. Louie, "Energy gaps in graphene nanoribbons," *Physical Review Letters*, vol. 97, p. 216803, Nov. 2006.

[26] P. Shemella, Y. Zhang, M. Mailman, P. M. Ajayan, and S. K. Nayak, "Energy gaps in zero-dimensional graphene nanoribbons," *Applied Physics Letters*, vol. 91, pp. 042101–042101–3, July 2007.

[27] S. Souma, M. Ogawa, T. Yamamoto, and K. Watanabe, "Numerical simulation of electronic transport in zigzag-edged graphene nano-ribbon devices," *Journal of Computational Electronics*, vol. 7, pp. 390–393, Sept. 2008.

[28] Y. P. Chen, Y. E. Xie, and X. H. Yan, "Electron transport of L-shaped graphene nanoribbons," *Journal of Applied Physics*, vol. 103, pp. 063711–063711–4, Mar. 2008.

[29] M. Han, B. Ozyilmaz, Y. Zhang, P. Jarillo-Herero, and P. Kim, "Electronic transport measurements in graphene nanoribbons," *physica status solidi (b)*, vol. 244, no. 11, pp. 4134–4137, 2007.

[30] S. Hong, Y. Yoon, and J. Guo, "Metal-semiconductor junction of graphene nanoribbons," *Applied Physics Letters*, vol. 92, pp. 083107–083107–3, Feb. 2008.

[31] R. N. Costa Filho, G. A. Farias, and F. M. Peeters, "Graphene ribbons with a line of impurities: Opening of a gap," *Physical Review B*, vol. 76, p. 193409, Nov. 2007.

[32] D. S. Novikov, "Transverse field effect in graphene ribbons," *Physical Review Letters*, vol. 99, p. 056802, July 2007.

[33] E.-J. Kan, Z. Li, J. Yang, and J. G. Hou, "Will zigzag graphene nanoribbon turn to half metal under electric field?," *Applied Physics Letters*, vol. 91, pp. 243116–243116–3, Dec. 2007.

[34] J. Fernández-Rossier, J. J. Palacios, and L. Brey, "Electronic structure of gated graphene and graphene ribbons," *Physical Review B*, vol. 75, p. 205441, May 2007.

[35] S. Okada, "Energetics of nanoscale graphene ribbons: Edge geometries and electronic structures," *Physical Review B*, vol. 77, p. 041408, Jan. 2008.

[36] O. Hod, J. E. Peralta, and G. E. Scuseria, "Edge effects in finite elongated graphene nanoribbons," *Physical Review B*, vol. 76, p. 233401, Dec. 2007.

[37] L. A. Agapito and H.-P. Cheng, "Ab initio calculation of a graphene-ribbon-based molecular switch," *The Journal of Physical Chemistry C*, vol. 111, pp. 14266–14273, Sept. 2007.

[38] S. Iijima, "Helical microtubules of graphitic carbon," *Nature*, vol. 354, pp. 56–58, Nov. 1991.

[39] Z. Yao, H. W. C. Postma, L. Balents, and C. Dekker, "Carbon nanotube intramolecular junctions," *Nature*, vol. 402, pp. 273–276, Nov. 1999.

[40] S. J. Tans, A. R. M. Verschueren, and C. Dekker, "Room-temperature transistor based on a single carbon nanotube," *Nature*, vol. 393, pp. 49–52, May 1998.

[41] M. S. Fuhrer, J. Nygå rd, L. Shih, M. Forero, Y.-G. Yoon, M. S. C. Mazzoni, H. J. Choi, J. Ihm, S. G. Louie, A. Zettl, and P. L. McEuen, "Crossed nanotube junctions," *Science*, vol. 288, Apr. 2000.

[42] E. Frackowiak and F. Béguin, "Electrochemical storage of energy in carbon nanotubes and nanostructured carbons," *Carbon*, vol. 40, pp. 1775–1787, Aug. 2002.

[43] P. Chen, X. Wu, J. Lin, and K. L. Tan, "High h2 uptake by alkali-doped carbon nanotubes under ambient pressure and moderate temperatures," *Science*, vol. 285, July 1999.

[44] A. Chambers, C. Park, R. T. K. Baker, and N. M. Rodriguez, "Hydrogen storage in graphite nanofibers," *The Journal of Physical Chemistry B*, vol. 102, pp. 4253–4256, May 1998.

[45] J. R. Wood, Q. Zhao, M. D. Frogley, E. R. Meurs, A. D. Prins, T. Peijs, D. J. Dunstan, and H. D. Wagner, "Carbon nanotubes: From molecular to macroscopic sensors," *Physical Review B*, vol. 62, pp. 7571–7575, Sept. 2000.

[46] S. Chopra, A. Pham, J. Gaillard, A. Parker, and A. M. Rao, "Carbon-nanotube-based resonant-circuit sensor for ammonia," *Applied Physics Letters*, vol. 80, pp. 4632–4634, June 2002.

[47] J.-C. Charlier, M. Terrones, M. Baxendale, V. Meunier, T. Zacharia, N. L. Rupesinghe, W. K. Hsu, N. Grobert, H. Terrones, and G. A. J. Amaratunga, "Enhanced electron field emission in B-doped carbon nanotubes," *Nano Letters*, vol. 2, pp. 1191–1195, Nov. 2002.

[48] H. Dai, J. H. Hafner, A. G. Rinzler, D. T. Colbert, and R. E. Smalley, "Nanotubes as nanoprobes in scanning probe microscopy," *Nature*, vol. 384, pp. 147–150, Nov. 1996.

[49] J. M. Romo-Herrera, B. G. Sumpter, D. A. Cullen, H. Terrones, E. Cruz-Silva, D. J. Smith, V. Meunier, and M. Terrones, "An atomistic branching mechanism for carbon nanotubes: Sulfur as the triggering agent," *Angewandte Chemie International Edition*, vol. 47, no. 16, pp. 2948–2953, 2008.

[50] G. H. Du, W. Z. Li, Y. Q. Liu, Y. Ding, and Z. L. Wang, "Growth of carbon nanotubes by pyrolysis of thiophene," *The Journal of Physical Chemistry C*, vol. 111, pp. 14293–14298, Oct. 2007.

[51] F. Deepak, A. Govindaraj, and C. Rao, "Synthetic strategies for Y-junction carbon nanotubes," *Chemical Physics Letters*, vol. 345, pp. 5–10, Sept. 2001.

[52] G. Kucukayan, R. Ovali, S. Ilday, B. Baykal, H. Yurdakul, S. Turan, O. Gulseren, and E. Bengu, "An experimental and theoretical examination of the effect of sulfur on the pyrolytically grown carbon nanotubes from sucrose-based solid state precursors," *Carbon*, vol. 49, pp. 508–517, Feb. 2011.

[53] Demoncy N., Pascard H., Loiseau A., Brun N., Colliex C., and Stephan O., "Sulfur: The key for filling carbon nanotubes with metals," *Synthetic Metals*, vol. 103, no. 1, pp. 2380–2383, 1999.

[54] M. S. Mohlala, X.-Y. Liu, M. J. Witcomb, and N. J. Coville, "Carbon nanotube synthesis using ferrocene and ferrocenyl sulfide. the effect of sulfur," *Applied Organometallic Chemistry*, vol. 21, no. 4, pp. 275–280, 2007.

[55] G. Maurin, F. Henn, B. Simon, J.-F. Colomer, and J. B. Nagy, "Lithium doping of multiwalled carbon nanotubes produced by catalytic decomposition," *Nano Letters*, vol. 1, pp. 75–79, Feb. 2001.

[56] V. Meunier, J. Kephart, C. Roland, and J. Bernholc, "Ab initio investigations of lithium diffusion in carbon nanotube systems," *Physical review letters*, vol. 88, Feb. 2002.

[57] M. Li, Y.-X. Yin, C. Li, F. Zhang, L.-J. Wan, S. Xu, and D. G. Evans, "Well-dispersed bi-component-active CoO/CoFe2O4 nanocomposites with tunable performances as anode materials for lithium-ion batteries," *Chemical Communications*, vol. 48, pp. 410–412, Dec. 2011.

[58] G. Kucukayan-Dogu, H. Sen, H. Yurdakul, S. Turan, O. Gulseren, and E. Bengu, "Synthesis of phosphorus included multi-walled carbon nanotubes by pyrolysis of sucrose," *Submitted*.

[59] G. Binnig, H. Fuchs, C. Gerber, H. Rohrer, E. Stoll, and E. Tosatti, "Energy-dependent state-density corrugation of a graphite surface as seen by scanning tunneling microscopy," *EPL (Europhysics Letters)*, vol. 1, p. 31, Jan. 1986.

[60] S.-I. Park and C. F. Quate, "Tunneling microscopy of graphite in air," *Applied Physics Letters*, vol. 48, pp. 112–114, Jan. 1986.

[61] M. Kuwabara, D. R. Clarke, and D. A. Smith, "Anomalous superperiodicity in scanning tunneling microscope images of graphite," *Applied Physics Letters*, vol. 56, pp. 2396–2398, June 1990.

[62] J. Xhie, K. Sattler, M. Ge, and N. Venkateswaran, "Giant and supergiant lattices on graphite," *Physical Review B*, vol. 47, pp. 15835–15841, June 1993.

[63] Z. Y. Rong and P. Kuiper, "Electronic effects in scanning tunneling microscopy: Moiré pattern on a graphite surface," *Physical Review B*, vol. 48, pp. 17427–17431, Dec. 1993.

[64] W.-T. Pong, J. Bendall, and C. Durkan, "Observation and investigation of graphite superlattice boundaries by scanning tunneling microscopy," *Surface Science*, vol. 601, pp. 498–509, Jan. 2007.

[65] V. J. Cee, D. L. Patrick, and T. P. Beebe Jr., "Unusual aspects of superperiodic features on highly oriented pyrolytic graphite," *Surface Science*, vol. 329, pp. 141–148, May 1995.

[66] J. E. Buckley, J. L. Wragg, H. W. White, A. Bruckdorfer, and D. L. Worcester, "Large-scale periodic features associated with surface boundaries in scanning tunneling microscope images of graphite," in *Proceedings of the Fifth International Conference on Scanning Tunneling Microscopy/Spectroscopy*, vol. 9, (Baltimore, Massachusetts (USA)), pp. 1079–1082, AVS, 1991.

[67] X. Yang, C. Bromm, U. Geyer, and G. von Minnigerode, "Several large-scale superperiodicities on highly oriented pyrolytic graphite observed by scanning tunneling microscopy," *Annalen der Physik*, vol. 504, no. 1, pp. 3–10, 1992.

[68] J. M. Campanera, G. Savini, I. Suarez-Martinez, and M. I. Heggie, "Density functional calculations on the intricacies of Moiré patterns on graphite," *Physical Review B*, vol. 75, p. 235449, June 2007.

[69] M. Born and R. Oppenheimer, "Zur quantentheorie der molekeln," *Annalen der Physik*, vol. 389, no. 20, pp. 457–484, 1927.

[70] D. R. Hartree, "The wave mechanics of an atom with a non-coulomb central field. part i. theory and methods," *Mathematical Proceedings of the Cambridge Philosophical Society*, vol. 24, no. 01, pp. 89–110, 1928.

[71] J. C. Slater, "Note on Hartree's method," *Physical Review*, vol. 35, pp. 210–211, Jan. 1930.

[72] L. H. Thomas, "The calculation of atomic fields," *Mathematical Proceedings of the Cambridge Philosophical Society*, vol. 23, no. 05, pp. 542–548, 1927.

[73] E. Fermi, "Eine statistische methode zur bestimmung einiger eigenschaften des atoms und ihre anwendung auf die theorie des periodischen systems der elemente," *Zeitschrift für Physik*, vol. 48, pp. 73–79, Jan. 1928.

[74] P. Hohenberg and W. Kohn, "Inhomogeneous electron gas," *Physical Review*, vol. 136, pp. B864–B871, Nov. 1964.

[75] W. Kohn and L. J. Sham, "Self-consistent equations including exchange and correlation effects," *Physical Review*, vol. 140, pp. A1133–A1138, Nov. 1965.

[76] A. D. Becke, "Density-functional exchange-energy approximation with correct asymptotic behavior," *Physical Review A*, vol. 38, pp. 3098–3100, Sept. 1988.

[77] J. P. Perdew and Y. Wang, "Accurate and simple analytic representation of the electron-gas correlation energy," *Physical Review B*, vol. 45, pp. 13244–13249, June 1992.

[78] J. P. Perdew, K. Burke, and M. Ernzerhof, "Generalized gradient approximation made simple," *Physical Review Letters*, vol. 77, pp. 3865–3868, Oct. 1996.

[79] M. C. Payne, M. P. Teter, D. C. Allan, T. A. Arias, and J. D. Joannopoulos, "Iterative minimization techniques for ab initio total-energy calculations: molecular dynamics and conjugate gradients," *Reviews of Modern Physics*, vol. 64, pp. 1045–1097, Oct. 1992.

[80] L. Laaksonen, F. Müller?Plathe, and G. H. F. Diercksen, "Fully numerical restricted Hartree-Fock calculations on open-shell hydrides: On the basis-set truncation error," *The Journal of Chemical Physics*, vol. 89, pp. 4903–4908, Oct. 1988.

[81] E. Baerends, "Orbital interaction theory of organic chemistry," *Recueil des Travaux Chimiques des Pays-Bas*, vol. 115, no. 3, pp. 200–200, 1996.

[82] B. Webster, *Chemical bonding theory.* Blackwell Scientific, 1990.

[83] N. W. Alcock, *Bonding and structure: structural principles in inorganic and organic chemistry*. New York: Ellis Horwood, 1990.

[84] R. V. Kasowski, "Electronic states of CO adsorbed onto Ni," *Physical Review Letters*, vol. 37, pp. 219–222, July 1976.

[85] L. Pisani, J. A. Chan, B. Montanari, and N. M. Harrison, "Electronic structure and magnetic properties of graphitic ribbons," *Physical Review B*, vol. 75, p. 064418, Feb. 2007.

[86] J. M. Romo-Herrera, M. Terrones, H. Terrones, S. Dag, and V. Meunier, "Covalent 2D and 3D networks from 1D nanostructures: Designing new materials," *Nano Letters*, vol. 7, pp. 570–576, Mar. 2007.

[87] Z. Wang, Z. Zhao, and J. Qiu, "Synthesis of branched carbon nanotubes from coal," *Carbon*, vol. 44, pp. 1321–1324, June 2006.

[88] A. A. Koós, R. J. Nicholls, F. Dillon, K. Kertész, L. P. Biró, A. Crossley, and N. Grobert, "Tailoring gas sensing properties of multi-walled carbon nanotubes by in situ modification with Si, P, and N," *Carbon*, vol. 50, pp. 2816–2823, July 2012.

[89] D. Yu, Y. Xue, and L. Dai, "Vertically aligned carbon nanotube arrays co-doped with phosphorus and nitrogen as efficient metal-free electrocatalysts for oxygen reduction," *The Journal of Physical Chemistry Letters*, vol. 3, pp. 2863–2870, Oct. 2012.

[90] P. E. Blöchl, "Projector augmented-wave method," *Physical Review B*, vol. 50, pp. 17953–17979, Dec. 1994.

[91] G. Kresse and D. Joubert, "From ultrasoft pseudopotentials to the projector augmented-wave method," *Physical Review B*, vol. 59, pp. 1758–1775, Jan. 1999.

[92] G. Kresse and J. Hafner, "Ab initio molecular dynamics for open-shell transition metals," *Physical Review B*, vol. 48, pp. 13115–13118, Nov. 1993.

[93] G. Kresse and J. Furthmüller, "Efficient iterative schemes for ab initio total-energy calculations using a plane-wave basis set," *Physical Review B*, vol. 54, pp. 11169–11186, Oct. 1996.

[94] J. P. Perdew, J. A. Chevary, S. H. Vosko, K. A. Jackson, M. R. Pederson, D. J. Singh, and C. Fiolhais, "Atoms, molecules, solids, and surfaces: Applications of the generalized gradient approximation for exchange and correlation," *Physical Review B*, vol. 46, pp. 6671–6687, Sept. 1992.

[95] P. Poizot, S. Laruelle, S. Grugeon, L. Dupont, and J.-M. Tarascon, "Nano-sized transition-metal oxides as negative-electrode materials for lithium-ion batteries," *Nature*, vol. 407, pp. 496–499, Sept. 2000.

[96] Y.-S. Hu, Y.-G. Guo, W. Sigle, S. Hore, P. Balaya, and J. Maier, "Electrochemical lithiation synthesis of nanoporous materials with superior catalytic and capacitive activity," *Nature materials*, vol. 5, Sept. 2006.

[97] Y.-G. Guo, J.-S. Hu, and L.-J. Wan, "Nanostructured materials for electrochemical energy conversion and storage devices," *Advanced Materials*, vol. 20, no. 15, pp. 2878–2887, 2008.

[98] F. Cheng, J. Liang, Z. Tao, and J. Chen, "Functional materials for rechargeable batteries," *Advanced materials (Deerfield Beach, Fla.)*, vol. 23, Apr. 2011.

[99] F.-F. Cao, Y.-G. Guo, and L.-J. Wan, "Better lithium-ion batteries with nanocable-like electrode materials," *Energy & Environmental Science*, vol. 4, pp. 1634–1642, Apr. 2011.

[100] Z. Zheng, Y. Wang, A. Zhang, T. Zhang, F. Cheng, Z. Tao, and J. Chen, "Porous Li2FeSiO4/C nanocomposite as the cathode material of lithium-ion batteries," *Journal of Power Sources*, vol. 198, pp. 229–235, Jan. 2012.

[101] A. K. Padhi, K. S. Nanjundaswamy, and J. B. Goodenough, "Phospho-olivines as Positive?Electrode materials for rechargeable lithium batteries," *Journal of The Electrochemical Society*, vol. 144, pp. 1188–1194, Apr. 1997.

[102] B. L. Ellis, K. T. Lee, and L. F. Nazar, "Positive electrode materials for Li-ion and Li-batteries," *Chemistry of Materials*, vol. 22, pp. 691–714, Feb. 2010.

[103] L. J. Xi, H.-E. Wang, Z. G. Lu, S. L. Yang, R. G. Ma, J. Q. Deng, and C. Chung, "Facile synthesis of porous LiMn2O4 spheres as positive electrode for high-power lithium ion batteries," *Journal of Power Sources*, vol. 198, pp. 251–257, Jan. 2012.

[104] J. Cabana, L. Monconduit, D. Larcher, and M. R. Palacín, "Beyond intercalation-based li-ion batteries: the state of the art and challenges of electrode materials reacting through conversion reactions," *Advanced materials (Deerfield Beach, Fla.)*, vol. 22, Sept. 2010.

[105] X.-Y. Xue, S. Yuan, L.-L. Xing, Z.-H. Chen, B. He, and Y.-J. Chen, "Porous Co3O4 nanoneedle arrays growing directly on copper foils and their ultrafast charging/discharging as lithium-ion battery anodes," *Chemical Communications*, vol. 47, pp. 4718–4720, Apr. 2011.

[106] H. Shimoda, B. Gao, X. P. Tang, A. Kleinhammes, L. Fleming, Y. Wu, and O. Zhou, "Lithium intercalation into opened single-wall carbon nanotubes: Storage capacity and electronic properties," *Physical Review Letters*, vol. 88, p. 015502, Dec. 2001.

[107] Z.-h. Yang and H.-q. Wu, "The electrochemical impedance measurements of carbon nanotubes," *Chemical Physics Letters*, vol. 343, pp. 235–240, Aug. 2001.

[108] Y. T. Lee, C. S. Yoon, and Y.-K. Sun, "Improved electrochemical performance of Li-doped natural graphite anode for lithium secondary batteries," *Journal of Power Sources*, vol. 139, pp. 230–234, Jan. 2005.

[109] D. Zhou, S. Seraphin, and S. Wang, "Single-walled carbon nanotubes growing radially from YC2 particles," *Applied Physics Letters*, vol. 65, pp. 1593–1595, Sept. 1994.

[110] S. Okada, S. Saito, and A. Oshiyama, "Energetics and electronic structures of encapsulated C60 in a carbon nanotube," *Physical review letters*, vol. 86, Apr. 2001.

[111] N. A. W. Holzwarth, S. G. Louie, and S. Rabii, "Lithium-intercalated graphite: Self-consistent electronic structure for stages one, two, and three," *Physical Review B*, vol. 28, pp. 1013–1025, July 1983.

[112] R. Benedek, A. P. Smith, and L. H. Yang, "Charge transfer in Rb-intercalated graphites," *Physical Review B*, vol. 49, pp. 7786–7789, Mar. 1994.

[113] K. R. Kganyago and P. E. Ngoepe, "Structural and electronic properties of lithium intercalated graphite LiC_6," *Physical Review B*, vol. 68, p. 205111, Nov. 2003.

[114] M. Khantha, N. A. Cordero, L. M. Molina, J. A. Alonso, and L. A. Girifalco, "Interaction of lithium with graphene: An ab initio study," *Physical Review B*, vol. 70, p. 125422, Sept. 2004.

[115] C. Hartwigsen, W. Witschel, and E. Spohr, "Charge density and charge transfer in stage-1 alkali-graphite intercalation compounds," *Physical Review B*, vol. 55, pp. 4953–4959, Feb. 1997.

[116] D. Lamoen and B. N. J. Persson, "Adsorption of potassium and oxygen on graphite: A theoretical study," *The Journal of Chemical Physics*, vol. 108, pp. 3332–3341, Feb. 1998.

[117] E. Durgun, S. Dag, V. M. K. Bagci, O. Gülseren, T. Yildirim, and S. Ciraci, "Systematic study of adsorption of single atoms on a carbon nanotube," *Physical Review B*, vol. 67, p. 201401, May 2003.

[118] K. Nishidate and M. Hasegawa, "Energetics of lithium ion adsorption on defective carbon nanotubes," *Physical Review B*, vol. 71, p. 245418, June 2005.

[119] N.-X. Chen and S. Rabii, "Ab initio calculation of the optical spectra of LiC_6 and the origins of its plasmons," *Physical Review Letters*, vol. 52, pp. 2386–2389, June 1984.

[120] K. Rytkönen, J. Akola, and M. Manninen, "Density functional study of alkali-metal atoms and monolayers on graphite (0001)," *Physical Review B*, vol. 75, p. 075401, Feb. 2007.

[121] K. T. Chan, J. B. Neaton, and M. L. Cohen, "First-principles study of metal adatom adsorption on graphene," *Physical Review B*, vol. 77, p. 235430, June 2008.

[122] A. Mansour, S. E. Schnatterly, and J. J. Ritsko, "Electronic structure of alkali-intercalated graphite studied by soft-x-ray emission spectroscopy," *Physical Review Letters*, vol. 58, pp. 614–617, Feb. 1987.

[123] M. Balasubramanian, C. S. Johnson, J. O. Cross, G. T. Seidler, T. T. Fister, E. A. Stern, C. Hamner, and S. O. Mariager, "Fine structure and chemical shifts in nonresonant inelastic x-ray scattering from Li-intercalated graphite," *Applied Physics Letters*, vol. 91, pp. 031904–031904–3, July 2007.

[124] A. Hightower, C. C. Ahn, B. Fultz, and P. Rez, "Electron energy-loss spectrometry on lithiated graphite," *Applied Physics Letters*, vol. 77, pp. 238–240, July 2000.

[125] N. Imanishi, S. Ohashi, T. Ichikawa, Y. Takeda, O. Yamamoto, and R. Kanno, "Carbon-lithium anodes for lithium secondary batteries," *Journal of Power Sources*, vol. 39, no. 2, pp. 185–191, 1992.

[126] J. P. Perdew and A. Zunger, "Self-interaction correction to density-functional approximations for many-electron systems," *Physical Review B*, vol. 23, pp. 5048–5079, May 1981.

[127] H. J. Monkhorst and J. D. Pack, "Special points for brillouin-zone integrations," *Physical Review B*, vol. 13, pp. 5188–5192, June 1976.

[128] M. Methfessel and A. T. Paxton, "High-precision sampling for brillouin-zone integration in metals," *Physical Review B*, vol. 40, pp. 3616–3621, Aug. 1989.

[129] G. Henkelman, A. Arnaldsson, and H. Jónsson, "A fast and robust algorithm for Bader decomposition of charge density," *Computational Materials Science*, vol. 36, pp. 354–360, June 2006.

[130] E. Sanville, S. D. Kenny, R. Smith, and G. Henkelman, "Improved grid-based algorithm for bader charge allocation," *Journal of Computational Chemistry*, vol. 28, no. 5, pp. 899–908, 2007.

[131] A. A. El-Barbary, R. H. Telling, C. P. Ewels, M. I. Heggie, and P. R. Briddon, "Structure and energetics of the vacancy in graphite," *Physical Review B*, vol. 68, p. 144107, Oct. 2003.

[132] K. Kobayashi, "Superstructure induced by a topological defect in graphitic cones," *Physical Review B*, vol. 61, pp. 8496–8500, Mar. 2000.

[133] J. T. Li, R. Berndt, and W.-D. Schneider, "Apparent superstructures in scanning tunneling microscopy," *Applied Physics Letters*, vol. 67, pp. 921–923, Aug. 1995.

[134] G. Binnig, H. Rohrer, C. Gerber, and E. Weibel, "7 x 7 reconstruction on Si(111) resolved in real space," *Physical Review Letters*, vol. 50, pp. 120–123, Jan. 1983.

[135] H. J. Mamin, E. Ganz, D. W. Abraham, R. E. Thomson, and J. Clarke, "Contamination-mediated deformation of graphite by the scanning tunneling microscope," *Physical Review B*, vol. 34, pp. 9015–9018, Dec. 1986.

[136] E. Cisternas, M. Flores, and P. Vargas, "Superstructures in arrays of rotated graphene layers: Electronic structure calculations," *Physical Review B*, vol. 78, p. 125406, Sept. 2008.

[137] J. M. Soler, A. M. Baro, N. García, and H. Rohrer, "Interatomic forces in scanning tunneling microscopy: Giant corrugations of the graphite surface," *Physical Review Letters*, vol. 57, pp. 444–447, July 1986.

[138] H. A. Mizes, S.-i. Park, and W. A. Harrison, "Multiple-tip interpretation of anomalous scanning-tunneling-microscopy images of layered materials," *Physical Review B*, vol. 36, pp. 4491–4494, Sept. 1987.

[139] K. Kobayashi, "Moiré pattern in scanning tunneling microscopy: Mechanism in observation of subsurface nanostructures," *Physical Review B*, vol. 53, pp. 11091–11099, Apr. 1996.

[140] D. Tománek, S. G. Louie, H. J. Mamin, D. W. Abraham, R. E. Thomson, E. Ganz, and J. Clarke, "Theory and observation of highly asymmetric atomic structure in scanning-tunneling-microscopy images of graphite," *Physical Review B*, vol. 35, pp. 7790–7793, May 1987.

[141] R. C. Tatar and S. Rabii, "Electronic properties of graphite: A unified theoretical study," *Physical Review B*, vol. 25, pp. 4126–4141, Mar. 1982.

[142] S. Hembacher, F. J. Giessibl, J. Mannhart, and C. F. Quate, "Local spectroscopy and atomic imaging of tunneling current, forces, and dissipation on graphite," *Physical Review Letters*, vol. 94, p. 056101, Feb. 2005.

[143] P. Ouseph, T. Poothackanal, and G. Mathew, "Honeycomb and other anomalous surface pictures of graphite," *Physics Letters A*, vol. 205, pp. 65–71, Sept. 1995.

[144] F. Atamny, O. Spillecke, and R. Schlögl, "On the STM imaging contrast of graphite: towards a "true" atomic resolution," *Physical Chemistry Chemical Physics*, vol. 1, pp. 4113–4118, Jan. 1999.

[145] P. Moriarty and G. Hughes, "Atomic resolved material displacement on graphite surfaces by scanning tunnelling microscopy," *Applied Physics Letters*, vol. 60, pp. 2338–2340, May 1992.

[146] C. D. Zeinalipour-Yazdi and D. P. Pullman, "A new interpretation of the scanning tunneling microscope image of graphite," *Chemical Physics*, vol. 348, pp. 233–236, June 2008.

[147] Y. Wang, Y. Ye, and K. Wu, "Simultaneous observation of the triangular and honeycomb structures on highly oriented pyrolytic graphite at room

temperature: An STM study," *Surface Science*, vol. 600, pp. 729–734, Feb. 2006.

[148] P. Oden, T. Thundat, L. Nagahara, S. Lindsay, G. Adams, and O. Sankey, "Superperiodic features observed on graphite under solution with scanning tunneling microscopy," *Surface Science Letters*, vol. 254, pp. L454–L459, Aug. 1991.

[149] M. Sasaki, Y. Yamada, Y. Ogiwara, S. Yagyu, and S. Yamamoto, "Moiré contrast in the local tunneling barrier height images of monolayer graphite on Pt(111)," *Physical Review B*, vol. 61, pp. 15653–15656, June 2000.

[150] M. Enachescu, D. Schleef, D. F. Ogletree, and M. Salmeron, "Integration of point-contact microscopy and atomic-force microscopy: Application to characterization of graphite/Pt(111)," *Physical Review B*, vol. 60, pp. 16913–16919, Dec. 1999.

[151] D.-Q. Yang, G.-X. Zhang, E. Sacher, M. José-Yacaman, and N. Elizondo, "Evidence of the interaction of evaporated Pt nanoparticles with variously treated surfaces of highly oriented pyrolytic graphite," *The Journal of Physical Chemistry B*, vol. 110, Apr. 2006.

[152] Y. Gan, W. Chu, and L. Qiao, "STM investigation on interaction between superstructure and grain boundary in graphite," *Surface Science*, vol. 539, pp. 120–128, Aug. 2003.

[153] T. R. Albrecht, H. A. Mizes, J. Nogami, S.-i. Park, and C. F. Quate, "Observation of tilt boundaries in graphite by scanning tunneling microscopy and associated multiple tip effects," *Applied Physics Letters*, vol. 52, pp. 362–364, Feb. 1988.

[154] P. Simonis, C. Goffaux, P. Thiry, L. Biro, P. Lambin, and V. Meunier, "STM study of a grain boundary in graphite," *Surface Science*, vol. 511, pp. 319–322, June 2002.

[155] Z. Y. Rong, "Extended modifications of electronic structures caused by defects: Scanning tunneling microscopy of graphite," *Physical Review B*, vol. 50, pp. 1839–1843, July 1994.

[156] J. Osing and I. Shvets, "Bulk defects in graphite observed with a scanning tunnelling microscope," *Surface Science*, vol. 417, pp. 145–150, Nov. 1998.

[157] P. Ouseph, "Scanning tunneling microscopy observation of dislocations with superlattice structure in graphite," *Applied Surface Science*, vol. 165, pp. 38–43, Sept. 2000.

[158] T. Bernhardt, B. Kaiser, and K. Rademann, "Formation of superperiodic patterns on highly oriented pyrolytic graphite by manipulation of nanosized graphite sheets with the STM tip," *Surface Science*, vol. 408, pp. 86–94, June 1998.

[159] H.-L. Sun, Q.-T. Shen, J.-F. Jia, Q.-Z. Zhang, and Q.-K. Xue, "Scanning tunneling microscopy study of superlattice domain boundaries on graphite surface," *Surface Science*, vol. 542, pp. 94–100, Sept. 2003.

[160] H. Beyer, M. Müller, and T. Schimmel, "Monolayers of graphite rotated by a defined angle: hexagonal superstructures by STM," *Applied Physics A*, vol. 68, pp. 163–166, Feb. 1999.

[161] J. B. Jasinski, S. Dumpala, G. U. Sumanasekera, M. K. Sunkara, and P. J. Ouseph, "Observation and interpretation of adjacent Moire patterns of different shapes in bilayer graphene," *Applied Physics Letters*, vol. 99, pp. 073104–073104–3, Aug. 2011.

[162] E. Suárez Morell, P. Vargas, L. Chico, and L. Brey, "Charge redistribution and interlayer coupling in twisted bilayer graphene under electric fields," *Physical Review B*, vol. 84, p. 195421, Nov. 2011.

[163] E. Cisternas, F. Stavale, M. Flores, C. A. Achete, and P. Vargas, "First-principles calculation and scanning tunneling microscopy study of highly oriented pyrolytic graphite (0001)," *Physical Review B*, vol. 79, p. 205431, May 2009.

[164] M. Ondráček, P. Pou, V. Rozsíval, C. González, P. Jelínek, and R. Pérez, "Forces and currents in carbon nanostructures: Are we imaging atoms?," *Physical Review Letters*, vol. 106, p. 176101, Apr. 2011.

Appendix A

Numerical Fortran Code For Moire Coordinate Generation

```
c     This Code is generating the input file of VASP. It generates
c     the atomic positions and lattice vectors of the rotated
c     bilayer graphene for the given values of p1 and q1.
      implicit double precision(a-h,o-z)
      double precision x(990000),y(990000),z(990000)
      double precision ax,ay,az
      character*3 pbc,at, ac
      character*40 sel,bel
      real aaa,bbb,rl
      open(4,file='OUTPUT',status='unknown')
      write(*,*)'R = m * a1 + n * a2'
      write(*,*)'Enter m and n, where m <= n'
      read(*,*)m,n
      write(*,*)'Latis tipi AA = 1, AB = 2'
      read(*,*)na
      if (na.le.1.5) then
      write(*,*)'Latis noktasi nerede olsun?'
      write(*,*)'Hexagonun ortasi 1, A atomu ustu 2'
```

```
read(*,*)mn
endif
if (na.ge.1.5) then
write(*,*)'Latis noktasi nerede olsun?'
write(*,*)'Hexagonun ortasi 1, A atomu ustu 2, B atomu ustu 3'
read(*,*)mn
endif
sel=' pos_6x6graphene'
write(4,10)sel
sel='   1.00000000000000'
write(4,10)sel
aaa=m*m+n*n+m*n
bbb=SQRT(aaa)
rl=2.46*bbb
as=1.7320508
a=2.46
rx1=a/2*(2*m+n)
ry1=-a*n*as/2
rx2=a*(n-m)/2
ry2=a*(n+m)*as/2
rz1=0.0
rz2=15.0
alatispar=SQRT((rx1*rx1+ry1*ry1)/3)
sel='dosyanin sonunda'
write(4,11)rx1,ry1,rz1
write(4,11)rx2,ry2,rz1
write(4,11)rz1,rz1,rz2
ax=(as*m)/(m+2*n)
alfa=atan(ax)
alfa2=2*alfa
alfa3=alfa2*57.295779513
write(4,17)alfa3, sel
sel='Selective Dynamics'
```

```
write(4,10)sel
write(4,*) alatispar
sel='Cartesian'
write(4,10)sel
bel=' T T T'
mm=0
z1=5.0
z2=8.35
nm=m+n
a1x=a/2
a1y=a*as/2
a2x=a
a2y=0.0
do k=-nm,nm
do kk=-nm,nm
rx=a1x*k+a2x*kk
ry=a1y*k+a2y*kk
rotrx=rx*cos(alfa2)-ry*sin(alfa2)
rotry=rx*sin(alfa2)+ry*cos(alfa2)
rhx1=rx+a/2
rhy1=ry+a*as/6
rotrhx1=rhx1*cos(alfa2)-rhy1*sin(alfa2)
rotrhy1=rhx1*sin(alfa2)+rhy1*cos(alfa2)
rhx2=rx+a
rhy2=ry+a*as/3
rotrhx2=rhx2*cos(alfa2)-rhy2*sin(alfa2)
rotrhy2=rhx2*sin(alfa2)+rhy2*cos(alfa2)
rax1=rx
ray1=ry
rotrax1=rax1*cos(alfa2)-ray1*sin(alfa2)
rotray1=rax1*sin(alfa2)+ray1*cos(alfa2)
rax2=rx+a/2
ray2=ry+a*as/6
```

```
rotrax2=rax2*cos(alfa2)-ray2*sin(alfa2)
rotray2=rax2*sin(alfa2)+ray2*cos(alfa2)
rbx1=rx
rby1=ry
rotrbx1=rbx1*cos(alfa2)-rby1*sin(alfa2)
rotrby1=rbx1*sin(alfa2)+rby1*cos(alfa2)
rbx2=rx-a/2
rby2=ry-a*as/6
rotrbx2=rbx2*cos(alfa2)-rby2*sin(alfa2)
rotrby2=rbx2*sin(alfa2)+rby2*cos(alfa2)
cd1=(n+m)*as*rx/(n-m)
cd2=-n*as*rx/(n+2*m)
cd3=rx*(m+n)*as/(n-m)-a*as*(m*m+n*n+m*n)/(n-m)
cd4=-rx*n*as/(2*m+n)+a*as*(m*m+n*n+m*n)/(2*m+n)
rotcd1=(n+m)*as*rotrx/(n-m)
rotcd2=-n*as*rotrx/(n+2*m)
rotcd3=rotrx*(m+n)*as/(n-m)-a*as*(m*m+n*n+m*n)/(n-m)
rotcd4=-rotrx*n*as/(2*m+n)+a*as*(m*m+n*n+m*n)/(2*m+n)
if (k.eq.0.and.kk.eq.0) then
mm=mm+4
if (na.le.1.5) then
if (mn.eq.1) then
write(4,9)rhx1,rhy1,z1,bel
write(4,9)rhx2,rhy2,z1,bel
write(4,9)rotrhx1,rotrhy1,z2,bel
write(4,9)rotrhx2,rotrhy2,z2,bel
endif
if (mn.eq.2) then
write(4,9)rax1,ray1,z1,bel
write(4,9)rax2,ray2,z1,bel
write(4,9)rotrax1,rotray1,z2,bel
write(4,9)rotrax2,rotray2,z2,bel
endif
```

```
endif
if (na.ge.1.5) then
if (mn.eq.1) then
write(4,9)rhx1,rhy1,z1,bel
write(4,9)rhx2,rhy2,z1,bel
write(4,9)rotrax1,rotray1,z2,bel
write(4,9)rotrax2,rotray2,z2,bel
endif
if (mn.eq.2) then
write(4,9)rax1,ray1,z1,bel
write(4,9)rax2,ray2,z1,bel
write(4,9)rotrhx1,rotrhy1,z2,bel
write(4,9)rotrhx2,rotrhy2,z2,bel
endif
if (mn.eq.3) then
write(4,9)rbx1,rby1,z1,bel
write(4,9)rbx2,rby2,z1,bel
write(4,9)rotrax1,rotray1,z2,bel
write(4,9)rotrax2,rotray2,z2,bel
endif
endif
endif
if (ry.lt.cd1.and.ry.gt.cd2.and.ry.gt.cd3.and.ry.lt.cd4) then
mm=mm+2
if (na.le.1.5) then
if (mn.eq.1) then
write(4,9)rhx1,rhy1,z1,bel
write(4,9)rhx2,rhy2,z1,bel
endif
if (mn.eq.2) then
write(4,9)rax1,ray1,z1,bel
write(4,9)rax2,ray2,z1,bel
endif
```

```
endif
if (na.ge.1.5) then
if (mn.eq.1) then
write(4,9)rhx1,rhy1,z1,bel
write(4,9)rhx2,rhy2,z1,bel
endif
if (mn.eq.2) then
write(4,9)rax1,ray1,z1,bel
write(4,9)rax2,ray2,z1,bel
endif
if (mn.eq.3) then
write(4,9)rbx1,rby1,z1,bel
write(4,9)rbx2,rby2,z1,bel
endif
endif
endif
if (rotry.lt.rotcd1.and.rotry.gt.rotcd2) then
if (rotry.gt.rotcd3.and.rotry.lt.rotcd4) then
mm=mm+2
if (na.le.1.5) then
if (mn.eq.1) then
write(4,9)rotrhx1,rotrhy1,z2,bel
write(4,9)rotrhx2,rotrhy2,z2,bel
endif
if (mn.eq.2) then
write(4,9)rotrax1,rotray1,z2,bel
write(4,9)rotrax2,rotray2,z2,bel
endif
endif
if (na.ge.1.5) then
if (mn.eq.1) then
write(4,9)rotrax1,rotray1,z2,bel
write(4,9)rotrax2,rotray2,z2,bel
```

```
    endif
    if (mn.eq.2) then
    write(4,9)rotrhx1,rotrhy1,z2,bel
    write(4,9)rotrhx2,rotrhy2,z2,bel
    endif
    if (mn.eq.3) then
    write(4,9)rotrax1,rotray1,z2,bel
    write(4,9)rotrax2,rotray2,z2,bel
    endif
    endif
    endif
    endif
    enddo
    enddo
 9  FORMAT(3F20.15,A35)
10  FORMAT(A40)
15  FORMAT(A4,2F10.4,A15)
12  FORMAT(I5,A5,I2,A5,I2)
13  FORMAT(3F10.6)
14  FORMAT(5E15.7)
11  FORMAT(3F20.15)
16  FORMAT(3E15.7)
17  FORMAT('Aci=',F10.7,'  ',A40)
    sel='  m ='
    bel='  n ='
    write(4,12)mm,sel,m,bel,n
    stop
    end
```